

UNCLASSIFIED

AD NUMBER
AD834874
NEW LIMITATION CHANGE
TO Approved for public release, distribution unlimited
FROM Distribution limited to U.S. Gov't. agencies and their Contractors; Specific authority; Other requests must be referred to Director, Defense Atomic Support Agency, Washington, D.C. 20305.
AUTHORITY
DTRA ltr, 3 Nov 99

THIS PAGE IS UNCLASSIFIED

3 JANUARY 1968

DASA 2083

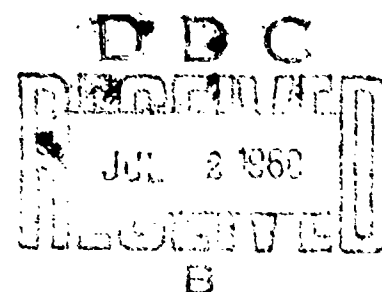
7

AD834874

LASER VELOCIMETER DEVELOPMENT PROGRAM FINAL REPORT

LW-57
(N-25-67-1)

PREPARED FOR THE DEFENSE ATOMIC SUPPORT AGENCY
UNDER CONTRACT DASA 01-67-C-0031



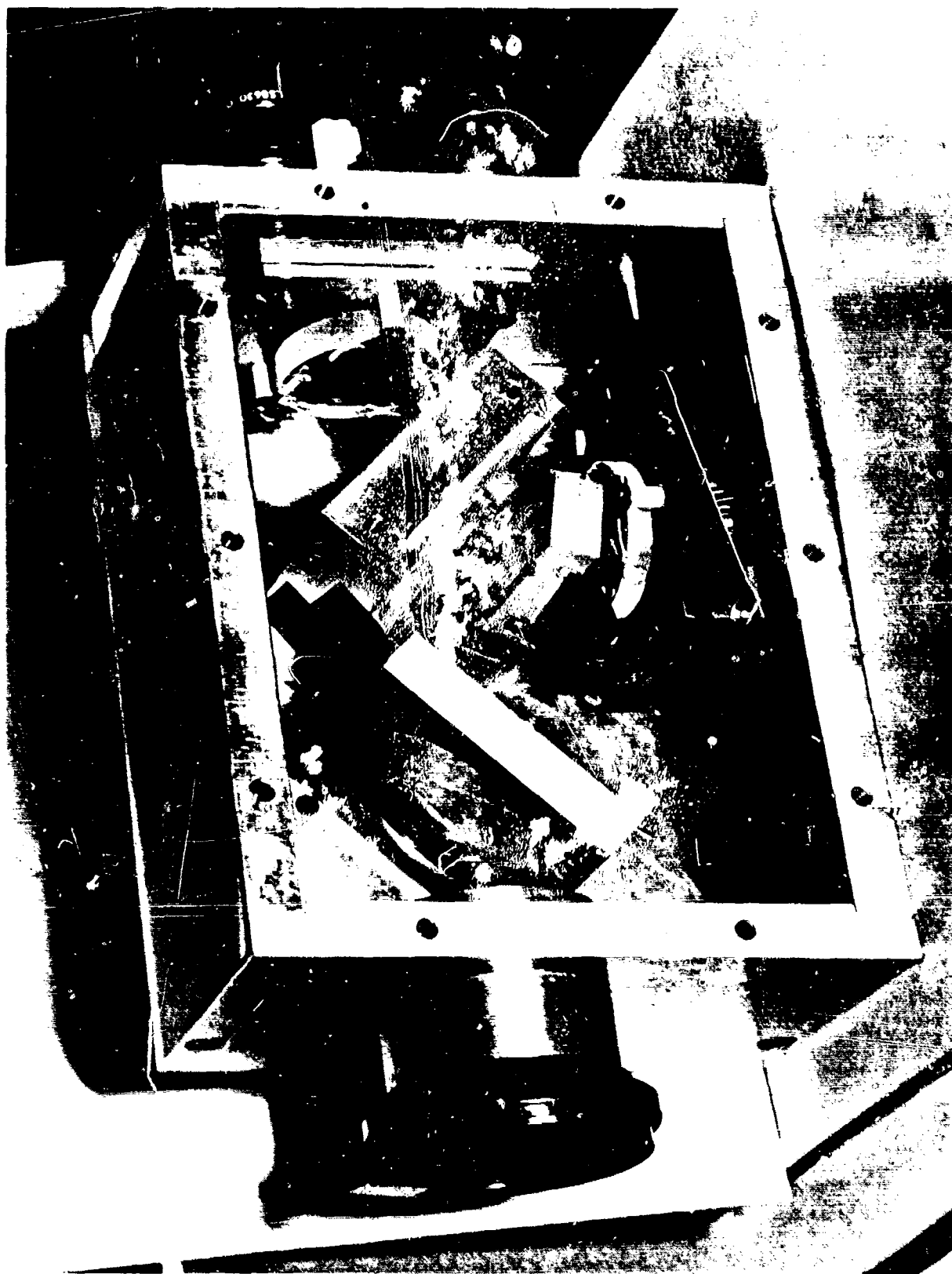
Lockheed

RESEARCH AND DEVELOPMENT DIVISION

MISSILES & SPACE COMPANY

A GROUP DIVISION OF LOCKHEED AIRCRAFT CORPORATION

(SUNNYVALE, CALIFORNIA)



The Angle-Compensated Differential Interferometer

LOCKHEED MISSILES & SPACE COMPANY

3 JANUARY 1968

DASA 2083

LASER VELOCIMETER DEVELOPMENT PROGRAM FINAL REPORT

(N-25-67-1)

PREPARED FOR THE DEFENSE ATOMIC SUPPORT AGENCY
UNDER CONTRACT DASA 01-67-C-0031

BY

C. W. GILLARD
G. S. ISHIKAWA
J. E. PETERSON

J. L. RAPIER
J. C. STOVER
N. L. THOMAS

APPROVED BY: Leo Davis
L. DAVIS, MANAGER
INFRARED AND OPTICAL SYSTEMS

Each transmittal of this document outside the agencies of the U.S. Government must have prior approval of the Director, Defense Atomic Support Agency, Washington, D.C. 20305.

Lockheed

RESEARCH AND DEVELOPMENT DIVISION

MISSILES & SPACE COMPANY

A GROUP DIVISION OF LOCKHEED AIRCRAFT CORPORATION

SUNNYVALE, CALIFORNIA

FORWORD

This report was prepared by Lockheed Missiles & Space Company (LMSC) under Defense Atomic Support Agency (DASA) Contract DASA 01-67-C-0031. The work was administered under the direction of the Blast and Shock Division, DASA Headquarters, with Lt. R. A. Armistead as Contracting Officer's Representative. Captain G. P. Crotwell of the Air Force Weapons Laboratory served as Technical Monitor. The research was performed by LMSC's Research and Development Division and funded by DASA.

ABSTRACT

This report presents the results of investigations for developing a laser system capable of measuring the velocity history of the free surface of a solid, shock-loaded material. Experimental data as well as considerations and analyses basic to phenomena affecting the accuracy and functional deployment of the system are examined.

Normally, diagnoses of the effects of shock in solid materials are deduced by measuring the effects of dynamic compression on a sample, requiring the installation of instrumentation on the surface of the sample. With some materials such instrumentation interferes with, and even negates, the desired measurement. Indeed, there exist environmental situations, as with hot samples, for example, where conventional instrumentation techniques are inappropriate.

The laser velocimeter system reported here is unique not so much in that it is capable of measuring the velocity history of the reflecting surface of a shock-loaded specimen using a laser beam, which has been done before (Ref. 1), but rather a new FM-AM optical discrimination system is featured that is capable of directly converting in a linear manner the Doppler signature of the reflected laser beam (which is directly proportional to the free-surface velocity of the shock-loaded specimen) to a corresponding AM output signal in a form particularly useful for oscilloscope display. The velocity-time history of a shock event is thus available immediately with no need for data reduction or processing; compatibility with conventional laboratory equipment is ensured and photographic records may be employed.

Using the breadboard laser velocimeter system described in this report and the LMSC Shock Facility (2.5-in. gas gun), several velocity-time measurements have

been made of the free surface of a shock-loaded aluminum plate. Tentative conclusions resulting from these measurements include the following:

- Velocity resolution (relative to full scale) is of the order of a few percent (possibly in the range of 2 to 4 percent).
- Time resolution of the electronic system is approximately 10 to 20 nsec.
- The velocity curves obtained thus far show what is interpreted as a precursor wave, indicate the possibility of an elastic-plastic wave interaction, show energy loss at spall, and indicate that the spalled element vibrates after separation. Vibrational energy remaining in the spalled element may be deduced from the measurements.

As a result of these investigations, it is evident that laser velocimeter systems designed along the lines of the system described in this report will provide a practical, convenient, and attractive way to monitor the velocity time history of events where velocities are of the order of 10^3 cm/sec and greater.

ACKNOWLEDGEMENTS

The investigations and results presented in this report reflect the combined efforts of many individuals. We are particularly indebted to the whole-hearted support provided by the group at LMSC's Shock Facility: Tom McCully, Boyd Jenrette, Randy Hipple, and Del Glenn. Assistance with the electronics was provided by Gil Tisue, Peter Sherk, Egon Donner, Sam Noel, and Troy Stark, all of whom contributed significantly of their own time, and who were motivated by the interesting technical challenge. Mechanical design and hardware implementation of the optical assemblies were handled by Karl Poerschke and Louis Waldron, respectively. Paul Gaebler, Research and Development Contracts, negotiated contractual terms of agreement and scheduled control of contractually required data. Clay Holland, Patent Department, docketed disclosure information and filed a U.S. patent application on the Differential Interferometer FM-AM Converter. George Patsakos, Physics Department, Stanford University, provided valuable analytical assistance. Dave Gilbert, LMSC Missile Systems Division, furnished inputs for portions of this report. Mr. Gilbert's foresight, help, and encouragement have been crucial to the success of the program. The managerial assistance of Leo Davis, provided the guidance, judgment, and inspiration that made our resources effective.

CONTENTS

Section		Page
	FOREWORD	iii
	ABSTRACT	v
	ACKNOWLEDGEMENTS	vii
	ILLUSTRATIONS	xiii
	TABLES	xv
1	INTRODUCTION	1-1
2	BASIC ASPECTS OF LASER VELOCIMETER DEPLOYMENT AND OPERATION	2-1
3	THE OPTICAL DISCRIMINATOR	3-1
	3.1 The Differential Interferometer Optical Discriminator	3-3
	3.2 Differential Interferometer - Implementation	3-7
	3.2.1 Wedge Assembly	3-7
	3.2.2 Bias and Tilt Plate Assembly	3-10
	3.2.3 Bias Control	3-12
	3.2.4 Beam Splitters and Mirrors	3-12
	3.2.5 Delay Element	3-14
	3.2.6 Iris and Window	3-14
	3.2.7 Photomultiplier System	3-16
	3.2.8 Thermal Insulation and Stability	3-16
	3.2.9 Initial Adjustment	3-18
4	RATIO AMPLIFIER	4-1
	4.1 Background	4-1
	4.2 Breadboard Ratio Amplifier	4-2
	4.3 Linearity	4-5
	4.4 Electronics Setup Procedures	4-9

Section	Page
4.4.1 Ratio Amplifier	4-9
4.4.2 Intensity Monitor	4-9
4.4.3 Triggering and Timing	4-10
5 TECHNICAL EVALUATION	5-1
5.1 Velocity Simulator	5-1
5.2 Experimental Work With the Velocity Simulator	5-3
5.3 Experimental Work in Shock Facility	5-15
5.4 Calibration Measurements in Shock Facility	5-23
6 CONCLUSIONS AND RECOMMENDATIONS	6-1
7 UNDERGROUND TEST FEASIBILITY	7-1
7.1 Introduction	7-1
7.2 Underground Test Environment	7-3
7.2.1 Physical Environment During Setup	7-3
7.2.2 Physical Environment During Operation	7-3
7.2.3 Radiation Environment During Operation	7-4
7.2.4 Physical Environment for Survival	7-5
7.3 Possible Configurations for Underground Tests	7-6
7.4 Velocimeter Redesign	7-9
7.4.1 Interferometer Optics	7-10
7.4.2 Interferometer Structure	7-16
7.4.3 Electronics	7-19
7.4.4 Calibration and Test Simulation	7-24
7.5 Conclusions and Recommendations	7-26
7.5.1 Conclusions	7-26
7.5.2 Recommendations	7-28
8 LIST OF SYMBOLS	8-1
9 REFERENCES	9-1

Appendixes

	Page
A SELECTION OF ΔL	A-1
B DETERMINATION OF $L(\epsilon)$	B-1
C AN EXAMINATION OF THE COHERENCE AND TIME-AVERAGING QUESTIONS FOR THE DIFFERENTIAL INTERFEROMETER	C-1
D EFFECTS OF SURFACE IRREGULARITIES IN THE INTERFEROMETER	D-1

Attachments

DISTRIBUTION LIST
DD FORM 1473

ILLUSTRATIONS

Figure		Page
	The Angle-Compensated Differential Interferometer	Frontispiece
1-1	A Sample Hugoniot Showing the Elastic/Plastic Regime	1-3
1-2	Application of Piezoelectric Transducers	1-3
1-3	Lagrangian Representation of Shock Fronts in Sample	1-5
2-1	Velocity Measurement Using a Laser Beam	2-2
2-2	Reflection From a Moving Mirror	2-3
2-3	Discriminator Characteristic Curve	2-5
2-4	Discriminator Transmission-Frequency Characteristics	2-6
2-5	Required Laser Power in Return Beam vs. Resolvable Intensity Levels	2-9
3-1	The Singlet Differential Interferometer	3-4
3-2	Differential Interferometer Optical Discriminator	3-8
3-3	Wedge Assembly	3-9
3-4	Bias, Tilt Plate, and Differential Screw Assembly	3-11
3-5	Mirror and Beam Splitter Assemblies	3-13
3-6	Assembled Mirror Systems	3-15
3-7	Ratio Amplifier Electronics and Photomultiplier Housing	3-17
3-8	Effect of Etalon on Fringe Patterns	3-19
4-1	Ratio Amplifier Electronics	4-3
4-2	Ratio Amplifier Schematic	4-4
4-3	Ratio Amplifier Calibration Curve	4-6
4-4	Ratio Amplifier Calibration Curves	4-7
5-1	Reflection From a Moving Mirror	5-2
5-2	Rotating Mirror Doppler Shifter	5-3
5-3	Velocity Simulator (Doppler Wheel)	5-4
5-4	Optical Layout for Velocity Simulator Measurements	5-5

Figure		Page
5-5	Laboratory Velocity Calibration Setup Using the Velocity Simulator	5-9
5-6	Experimental Data and Theoretical Curve for Response of First Interferometer to Source Velocity	5-13
5-7	Experimental Data and Theoretical Curve for Response of Second Interferometer to Source Velocity	5-14
5-8	Optical Layout for Shock Measurements	5-16
5-9	Laser Velocimeter Free-Surface Velocity Traces of Shock-Loaded Aluminum	5-17
5-10	Response vs. Free-Surface Velocity	5-24
5-11	Principle of Operation of a Cat's Eye Retroreflector	5-25
5-12	Velocimeter Flight Records of Special Pistons (Fliers) Down Gas-Gun Barrel	5-26
7-1	Possible Velocimeter Test Configurations	7-7
7-2	Tentative Interferometer Concept	7-14
7-3	Electronic Block Diagram	7-20
B-1	The Singlet Interferometer	B-2
B-2	The General Differential Interferometer	B-7
B-3	The Doublet Differential Interferometer	B-14
C-1	Differential Interferometer Having Travel Time Difference τ	C-2
C-2	Biasing Position on Intensity Curve	C-6
C-3	Effects of a Decrease in Visibility	C-6
C-4	Example Operating Points on Intensity Curve	C-9
D-1	Beam Paths in Interferometer	D-1
D-2	Errors Introduced by Reflection at Surface b	D-2
D-3	Errors Introduced by Transmission Through Surface a	D-3
D-4	Errors Introduced by Surfaces f and g	D-4
D-5	Errors Introduced by Transmission Through Surface b	D-5
D-6	Errors Introduced at Surfaces c and d	D-5
D-7	Error Introduced at Surface e	D-6

TABLES

Table		Page
5-1	Velocity Simulator Data for First Interferometer	5-7
5-2	Velocity Simulator Data for Second Interferometer	5-10
5-3	Relevant Parameters of Interferometers No. 1 and No. 2	5-11
5-4	Velocimeter Data From LMSC Shock Facility	5-20
5-5	Velocimeter Special Flyer Data	5-27
7-1	Comparison of Velocimeter Types	7-31

Section 1
INTRODUCTION

The study of shock in solids has been a useful means of investigating the dynamic properties of materials. Of particular interest are transient effects measured while a shock event is underway within a specimen. This report presents the results of investigations for developing a laser system capable of measuring the velocity history of the free surface of a solid shock-loaded material.

Lockheed Missiles & Space Company's laser velocimeter system features a new FM-AM optical discrimination system capable of directly converting in a linear manner the Doppler signature on a laser beam reflected by a shock-loaded surface to a corresponding AM output signal in a form particularly useful for oscilloscope display. Since the frequency of the Doppler shifted optical signal is directly proportional to the free-surface velocity of the shock-loaded specimen, the system output immediately gives the velocity time history of the surface during the shock event.

In the study of high-intensity shock-wave propagation through solids, a knowledge of the equation-of-state of the solid enables one to compute the decay of shock speed as the wave progresses through the solid. Several theoretical models exist for the mathematical representation of such an equation of state, the Mie-Gruneisen form being the best known for solids possessing well-ordered lattices. This representation, however, must rely ultimately on an experimental set of base points or reference points from which the mathematical expression evolves.

In the study of solids, a set of experimental Hugoniot reference points has been obtained statically by hydrostatic compression and, for high pressures, dynamically by means of explosive or projectile loading of materials and subsequent study of the ensuing shock propagation. From this last experimental setup, a principal-Hugoniot curve is obtained

that represents the locus of all pressure-volume-energy states obtainable by shock compression of variable intensity. Secondary-Hugoniot curves, corresponding to moderate or high initial temperatures, must also be obtained to account for materials in depth heating — the so-called thermal shock problem.

An example of a Hugoniot relation, normally measured with zero initial stress and at room temperature, is illustrated in Fig. 1-1. A large number of materials exhibit the characteristics shown, namely two regions: an elastic region and a plastic region. The elastic region extends from zero longitudinal stress to S_y , the dynamic yield stress. The plastic regime lies between the stresses S_p and S_y . The stress S_y connotes the existence of a cusp. At stresses above S_y , the solid will flow. Two shocks are generated by an impact producing a stress in the plastic regime. The leading shock is elastic and propagates near the dilation speed at the level of the dynamic yield stress; the trailing shock is purely plastic and raises the stress from S_y to the stress at the impact interface. Impact stresses below S_y and above S_p are stable; i. e., only one shock is produced. At levels somewhere above S_p , when deviation of longitudinal and transverse stress are negligible, the hydrodynamic theory is applicable. At regions somewhere below S_y , the linear elastic theory is applicable.

Realistic representations of material Hugoniots must account experimentally for the existence of both an elastic and plastic wave and must determine with precision the value of the dynamic yield stress.

The determination of the Hugoniot requires measurement of only two quantities: the shock-wave speed as it travels through the sample, and either the stresses produced by the shock or the sample particle velocity as induced by the shock passage at some convenient sampling station, such as a free surface.

Normally, the stresses produced by the shock are measured by installation of pressure transducers on the surface of the sample. A schematic drawing of a conceptual experimental arrangement is shown in Fig. 1-2. A flying sample, IS is accelerated to a

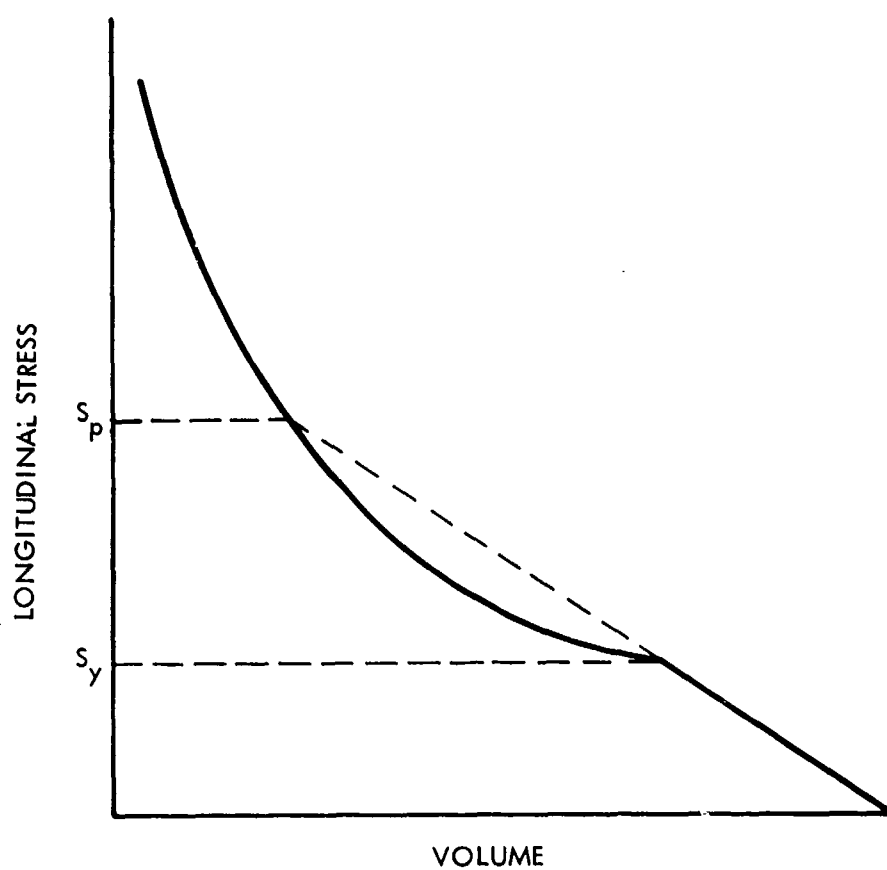


Fig. 1-1 A Sample Hugoniot Showing the Elastic/Plastic Regime

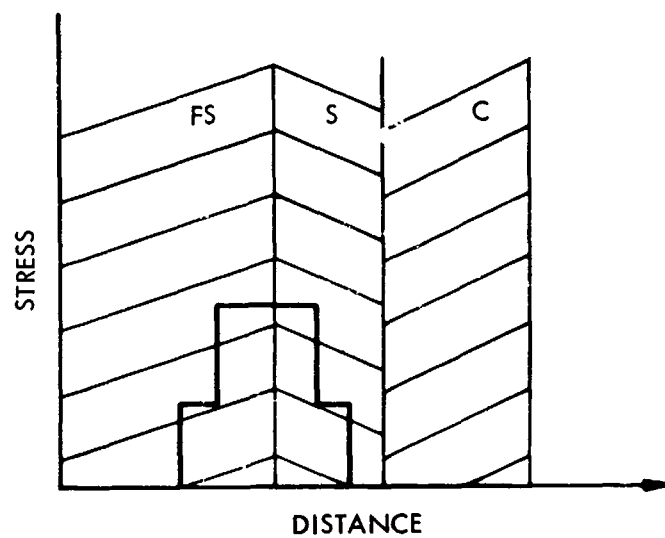


Fig. 1-2 Application of Piezoelectric Transducers

desired speed to impact on the stationary material sample S to which a crystal pressure transducer C has been affixed. Both FS and S must be of the same material. The average shock speed through S is measured by timing both the impact of FS and S and the initial response of C . Transmitted shock stresses are measured by the crystal transducer.

This technique works satisfactorily as long as one shock wave is propagated, i. e., for induced stresses above S_p or below S_y of Fig. 1-1. In the Hugoniot region between S_y and S_p , there are two wave fronts. The elastic wave first reaches the transducer at time T_1 (Fig. 1-3) with a stress level S_y . Subsequent shock arrival times T_2 , T_3 , etc., will be registered with accompanying stress discontinuities as a result of the interaction of the reflected elastic front with the plastic shock front. The plastic wave, however, never reaches the transducer. In fact, in most cases, its shock speed cannot be inferred from T_1 and T_2 because the velocities of reflections of the initial elastic front are generally not known. These velocities depend on the state of the material at the plastic front, a quantity that has to be determined by experiment.

The presence of a crystal transducer thus interferes with the very purpose of the experimental setup, namely the measurement of speed and impact stresses of both elastic and plastic waves. Indeed, there exist environmental situations, as with hot samples, for example, where such instrumentation techniques are inappropriate. Secondary-Hugoniot measurements are plagued with difficulties of proper calibration of preheated quartz transducers.

Transducers can be eliminated if the particle velocity of the free surface is measured instead. This has several advantages. Since the back surface of the sample is free, the reflection of the elastic precursor off the surface would always travel at the dilatation velocity. Furthermore, the reflection of this reflected wave off the plastic front would be elastic and would travel with a speed that could be predetermined and in any event would be near the dilatation speed. Thus, only a free surface is compatible with the determination of the Hugoniot in the elastic/plastic region. The foregoing considerations provide, in essence, the argument from which an active interest in laser-based velocimeter systems has evolved.

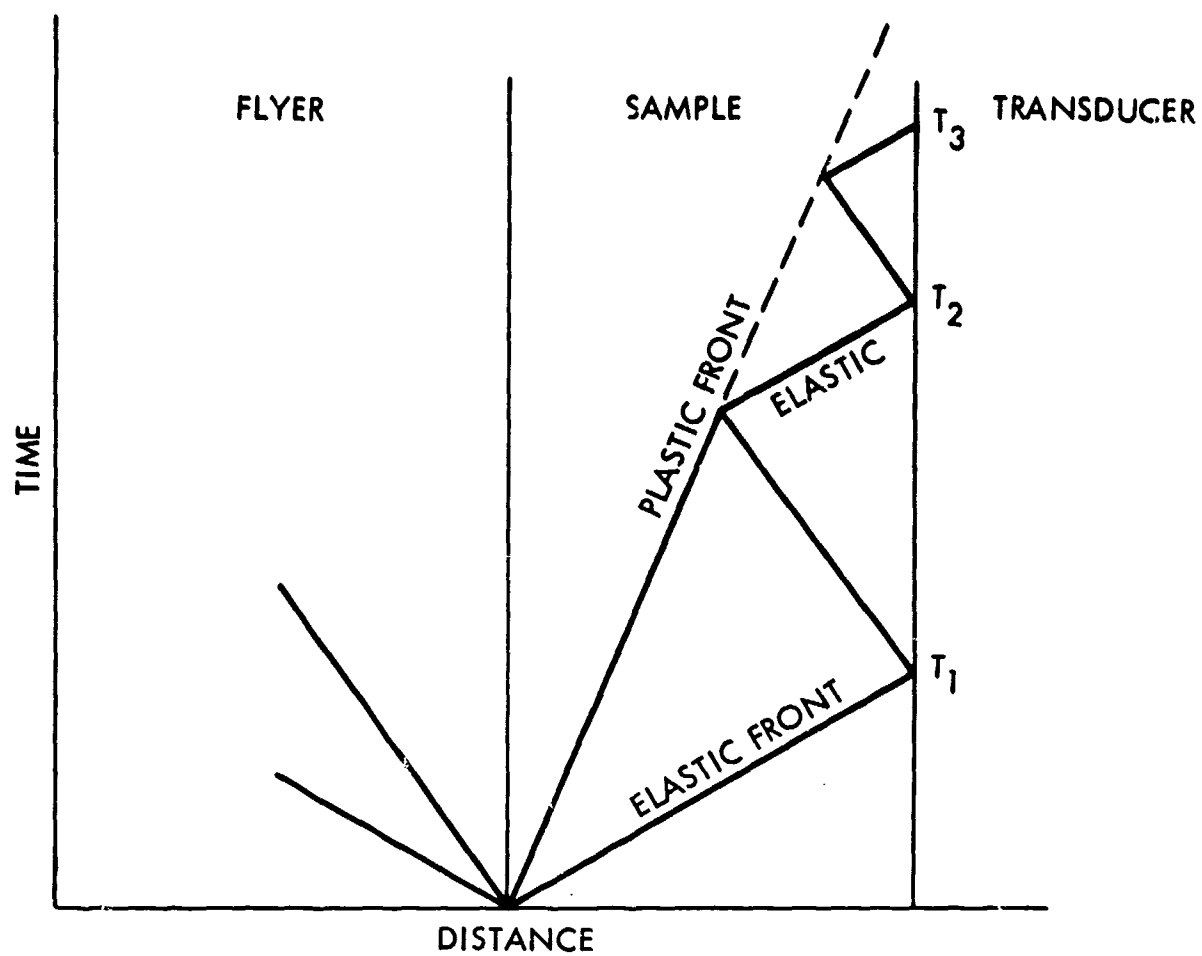


Fig. 1-3 Lagrangian Representation of Shock Fronts in Sample

BLANK PAGE

Section 2

BASIC ASPECTS OF LASER VELOCIMETER DEPLOYMENT AND OPERATION

This section provides technical perspective on the laser velocimeter, describes its basis of operation, and indicates a number of requirements to be met for proper instrumentation. Instrument operation is based upon reflection of a laser beam from a moving target surface and measurement of the resultant Doppler frequency; this frequency is very nearly proportional to target velocity at the speeds of interest to shock studies.

Velocimeters exploiting the spatial or temporal coherence of laser beams have been designed and are described in the literature (Refs. 2 and 3). These instruments generally operate as follows. In one instrument, the target surface is made reflective and is used as one of the mirrors in a Michelson-type interferometer. Upon proper alignment with the second mirror, a pattern consisting of interference fringes is focused onto a photodetector. The photodetector and associated electronics count interference fringes in order to measure target movement. Another technique involves directing a laser beam upon a diffusely reflecting surface and measuring the motion of the resultant diffraction or speckle pattern.

As a result of our investigations a new velocity measuring technique has evolved that eliminates the high-frequency requirements of fringe counting by employing a new optical discriminator developed at LMSC. This new device is capable of linearly converting Doppler frequency-shifted coherent light reflected from a moving target to amplitude variations that can be sensed by a photodetector. Thus, target velocity may be related to a variation in output signal amplitude. This technique is rather uniquely suited to the requirements of nuclear testing and conventional equation-of-state work where velocity accuracies of 1 to 10 percent are sufficient. The velocity measurement does not perturb the target/shock-wave interaction. Also, the required instrumentation is relatively inexpensive and can be remotely located with respect to the interaction volume.

Basic components of the LMSC laser velocimeter are shown in block diagram form in Fig. 2-1. This figure does not show the actual equipment layout; it merely assists in illustrating the concepts. In order to simplify the analysis, it is assumed that the shock waves arrive in plane parallel wave fronts and produce a target velocity v only in the direction of shock-wave propagation. The laser light arriving at the discriminator from the specularly reflective target surface will be shifted in frequency due to target motion.

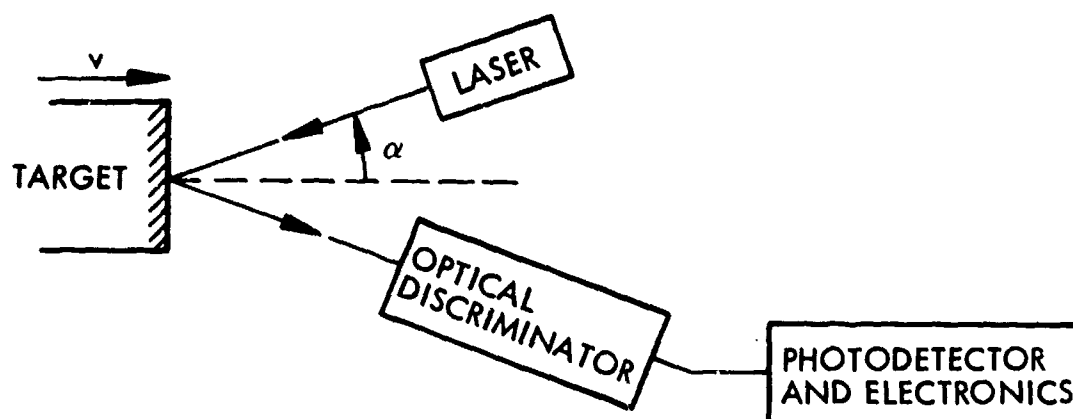


Fig. 2-1 Velocity Measurement Using a Laser Beam

For the simple case of relative velocity between an observer and source, the relativistic formula for the Doppler effect is given by

$$\nu = \frac{\nu_o (1 - \beta^2)^{1/2}}{1 - \beta \cos \alpha} \quad (2.1)$$

where

- ν = laser frequency measured by observer (in reference frame K)
- ν_o = laser frequency in "proper frame"
- β = v/c where c is velocity of light
- α = angle between target velocity vector v and direction of light ray propagation as measured in K frame

It is assumed in the above expression that the observer is stationary and located at the origin of an inertial reference frame K , while the light source originating from the mirror is in frame K_0 moving at velocity v in the positive X -direction relative to K . This definition insures that $\nu > \nu_0$ when $\alpha < \pi/2$ and $\nu < \nu_0$ when $\alpha > \pi/2$. Equation (2.1) can be approximated by expanding and retaining first-order terms in β to give

$$\nu_D \equiv \nu - \nu_0 \approx \nu_0 \beta \cos \alpha \quad (2.2)$$

where

ν_D = Doppler difference frequency

This equation must be slightly modified to account for the effect of the mirror. As shown in Fig. 2-2, when the source is reflected from a moving mirror it has an apparent normal velocity component twice that of the mirror and in the same direction.

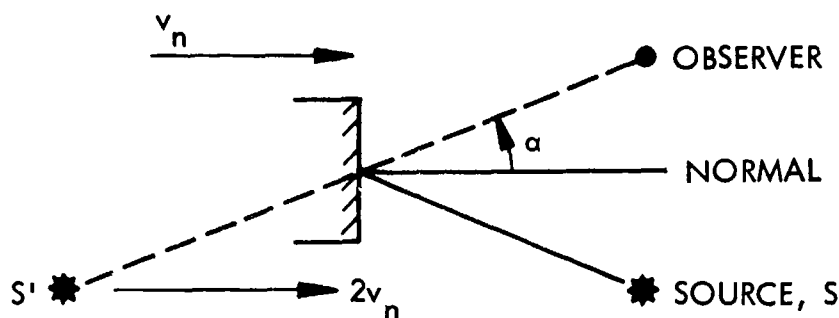


Fig. 2-2 Reflection From a Moving Mirror

Therefore, the Doppler difference frequency is given by

$$\nu_D \approx \frac{2 \nu_0 v_n \cos \alpha}{c} = \frac{2 v_n}{\lambda_0} \cos \alpha \quad (2.3)$$

To illustrate the magnitude of the difference frequency, consider a high-velocity target traveling 4×10^5 cm/sec and an He-Ne laser source ($\lambda_0 = 6.3 \times 10^{-5}$ cm) incident at an angle of 45 deg. Using these parameters, the difference frequency calculated from Eq. (2.3) is approximately 8.9 GHz. Thus, a target accelerated from rest position to a terminal velocity of 4×10^5 cm/sec would require a sensing system capable of a 0 to 9 GHz frequency response. Attempts to fringe count at this rate would exceed the capability of conventional electronic and microwave systems. Fortunately, the optical discriminator described herein appears to be uniquely suited to Doppler frequency excursions of this magnitude.

Basis of operation and technical details of the differential interferometer optical discriminator are discussed later. For the present discussion it will suffice to limit consideration of the optical discriminator to a black box device with functional properties that can be completely described by its intensity transmission characteristic curve. It is shown in Section 3 that the intensity transmission curve is given by

$$I/I_0 = \cos^2 \left(\frac{\pi \Delta L}{c} \nu + \frac{\varphi}{2} \right) \quad (2.4)$$

or equivalently,

$$I/I_0 = \frac{1}{2} \left[1 + \cos \left(\frac{2\pi \Delta L}{c} \nu + \varphi \right) \right]$$

where

I/I_0 = ratio of the actual output to maximum output light intensity

φ = a phase bias term

ΔL = total optical path difference in the interferometer

Qualitatively, optical intensity as a function of ν would have the following appearance.

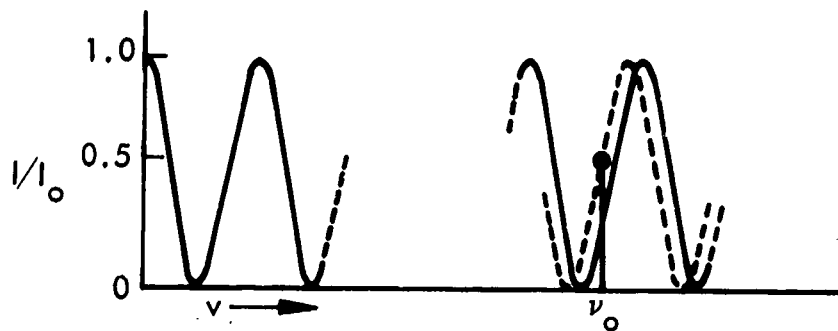


Fig. 2-3 Discriminator Characteristic Curve

The sensitivity of the device to changes in optical frequency is determined by ΔL , which depends upon the geometrical configuration of the interferometer. The operating point on the discriminator transmission curve may be shifted with frequency (or biased) by means of a mechanical adjustment. This mechanical biasing procedure controls the phase shift factor ϕ in Eq. (2.4) and permits biasing at any desired operating point (dashed curve in Fig. 2-3).

As discussed previously, the discriminator converts a velocity measurement to a measurement of optical intensity as a function of time. For a given velocimeter application, where sampling rate (time resolution) and accuracy (optical intensity resolution) are specified, required laser power and signal-to-noise ratio are calculable.

Consider the discriminator optical transmission curve illustrated in Fig. 2-4. In general, a photodetector is required to sense some M intensity levels between power points P_1 and P_2 . As shown, a restricted portion of the curve is used to limit nonlinearities and end effects.

Measuring optical intensity at the output of the discriminator from one sample period to the next is analogous to viewing an electronic picture. In the first instance, one is comparing the number of photons received during adjacent sample periods while in the second case (i. e., an image tube), one is comparing the number of photons in adjacent resolution elements. Thus, a correspondence may be considered to exist between the

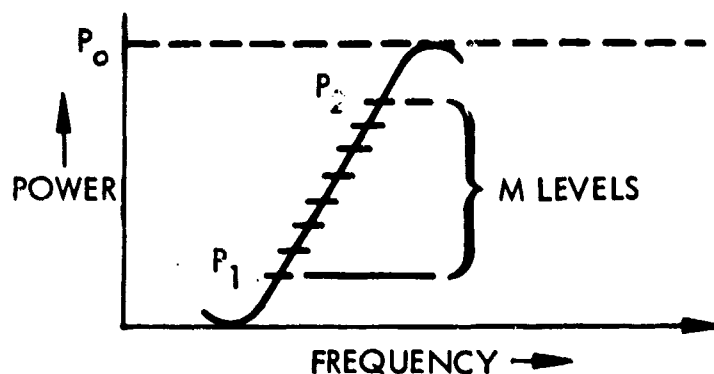


Fig. 2-4 Discriminator Transmission-Frequency Characteristics

temporal and spatial domains in this analogy. This correspondence allows one to apply certain imaging system concepts (Ref. 4) developed from Poisson statistics to the optical discriminator.

For two neighboring resolution elements (or sample periods) A and B whose average photon populations are \bar{N}_a and \bar{N}_b , the minimum contrast ratio C is defined by

$$C = \frac{\bar{N}_a - \bar{N}_b}{\bar{N}_a} \quad (2.5)$$

where $\bar{N}_a - \bar{N}_b$ represents the smallest increment in photon populations detectable. Using this definition, the potential number of intensity levels that can be sensed is equal to $1/C$.

The certainty coefficient K , which is a measure of the signal to rms noise when comparing intensity levels A and B, is given by

$$K = \frac{\bar{N}_a - \bar{N}_b}{(\bar{N}_a + \bar{N}_b)^{1/2}} \quad (2.6)$$

A value of $K = 2.0$ gives good assurance that a difference reading between two adjacent elements (sample periods) is real rather than a statistical fluctuation in photon population.

It can be shown that the signal-to-noise ratio for a single resolution element A , or sample period, is given by $S/N = N_a$; or, substituting the expressions for C and K

$$\frac{S}{N} = \left(\frac{K}{C}\right)^2 (2 - C) \quad (2.7)$$

The M power levels shown on Fig. 2-4 are related to the contrast ratio, C , by

$$\frac{1}{C} = \frac{P_a}{\rho P_o} \quad (2.8)$$

where

$$\rho = \frac{P_2 - P_1}{P_o}$$

is the fractional portion of the full laser power P_o actually employed in the measurement, and P_a is the nominal operating power level on the curve.

To reduce nonlinearities, ρ will typically be about 0.3 to 0.5 and the operating point P_a will be approximately $P_o/2$. Substituting these values into Eq. (2.8), the signal-to-noise ratio is now given by

$$\frac{S}{N} = \frac{1}{2} \left(\frac{KM}{\rho} \right)^2 \left(1 - \frac{\rho}{M} \right) \quad (2.9)$$

For quantum noise limited photodetection, one can also write

$$\frac{S}{N} = \frac{\eta P}{h\nu B} \quad (2.10)$$

where

- P = average power during sampling period
- η = photodetector quantum efficiency
- $h\nu$ = energy per photon
- B = sampling bandwidth (i. e., reciprocal of sampling period)

For the case illustrated, $P \approx P_o/2$ so that combining Eqs. (2.9) and (2.10) gives

$$P_o = \frac{h\nu B}{\eta} \left(\frac{KM}{\alpha} \right)^2 \left(1 - \frac{\rho}{M} \right) \quad (2.11)$$

Figure 2-5 is a graph of laser power P_o plotted as a function of ρ and M for the following parametric values:

- $h\nu = 3.14 \times 10^{-19}$ joule/photon at 6328 A (He-Ne laser wavelength)
- $\eta = 0.006$ (RCA S-11 photocathode surface)
- $B = 10^8$ Hz
- $K = 2.0$

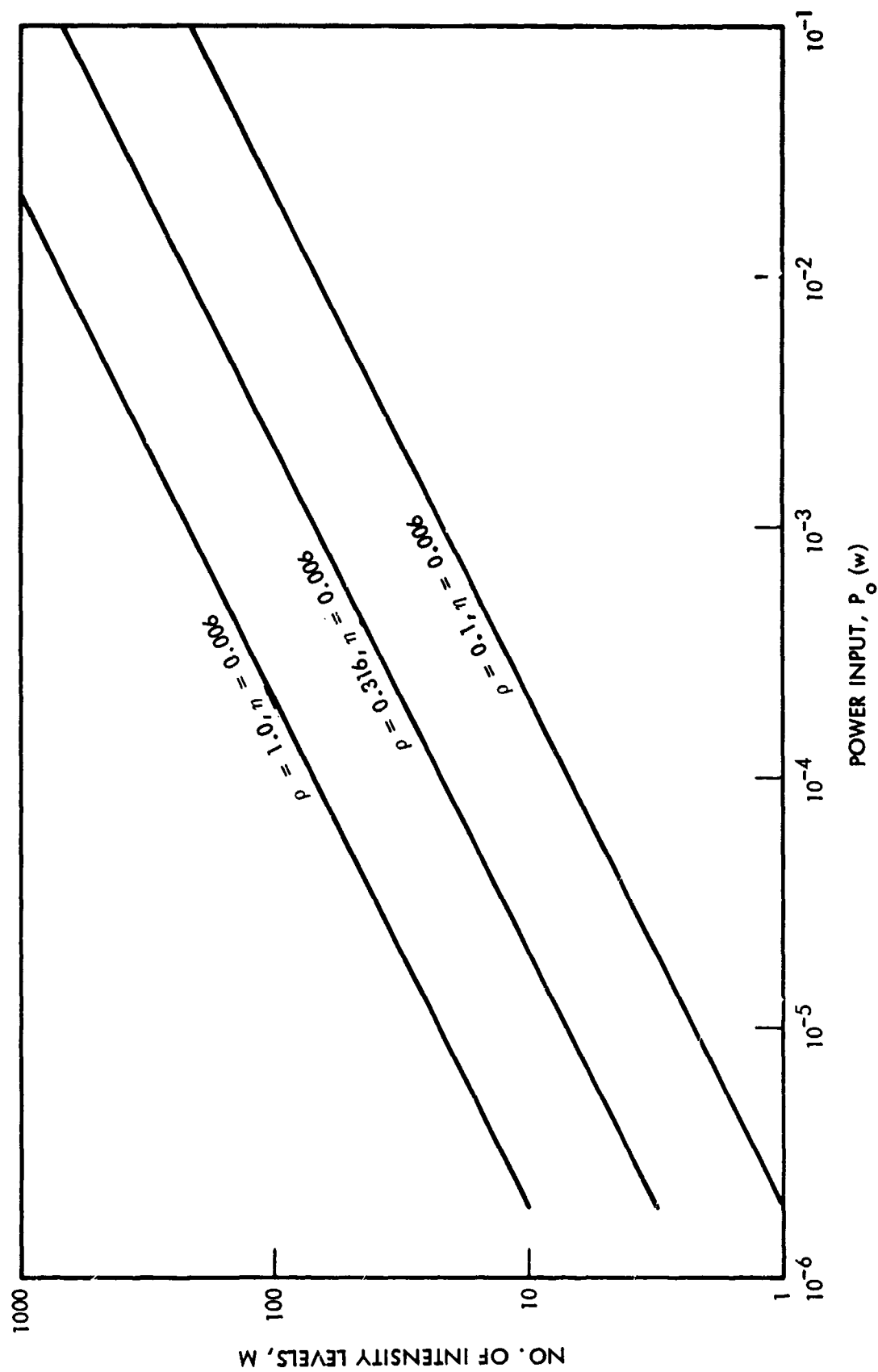


Fig. 2-5 Required Laser Power in Return Beam vs. Resolvable Intensity Levels

As shown on the graph, a velocity accuracy of 1 percent ($M = 100$) for a sampling period of $0.01 \mu\text{sec}$ requires a laser power of less than 2 mw. Allowing for optical reflection losses, alignment factors, etc., it is estimated that less than 5 mw will provide adequate signal power for equation-of-state diagnostics.

Low resolution (velocity accuracy approximately 10 percent) can be achieved with considerably less laser power.

Section 3

THE OPTICAL DISCRIMINATOR

The optical discriminator is a device that splits an input optical beam into two components, delays one component relative to the other, and then coherently recombines these two waves at the output end of the device. Optical delay may be related to the traversing of two optical paths that are different, say by an amount ΔL .

Optical discriminators exist in several forms. Early in this study LMSC planned to use a birefringent discriminator (Ref. 5). With this device optical delay is achieved by splitting the input beam into ordinary and extraordinary waves in a birefringent crystal such as calcite. Path length difference ΔL in such a device is related to crystal length L_c and refractive indices n_e and n_o by the relationship

$$\Delta L = (n_e - n_o) L_c \quad (3.1)$$

A simple Michelson interferometer with unequal arms may also be employed as an optical discriminator. With this device the total optical path difference is given by

$$\Delta L = 2\Delta S \quad (3.2)$$

where ΔS is the single-pass optical path length differential between the two arms of the interferometer.

Both the birefringent discriminator and the unequal arm-length Michelson interferometer are very sensitive to angular variation in the input optical beam, and hence possess a small acceptance angle. A new kind of optical discriminator, termed a differential interferometer, has been devised for use with the laser velocimeter. It is essentially

an unequal arm-length Michelson interferometer, yet, through the inclusion of additional optical elements, the sensitivity of this device to input beam angular variations may be greatly reduced and its acceptance angle significantly increased. It will be shown later that the optical path difference for the simplest version of this new device is given by

$$\Delta L = 2 \ell_{a1} \left(n_{a1} - \frac{1}{n_{a1}} \right) \quad (3.3)$$

where ℓ_{a1} is the thickness of a dielectric plate and n_{a1} is its refractive index.

A simple argument that ignores mutual coherence effects may be employed to illustrate the basic features of our new optical discriminator. Phase difference θ of two rays after traversing different paths is given by

$$\theta = \frac{2\pi\Delta L}{\lambda} + \varphi = \frac{2\pi\Delta L}{c} \nu + \varphi \quad (3.4)$$

where

ΔL = optical path difference

ν = laser frequency plus Doppler shift

c = speed of light

φ = bias term, controlled by an incremental adjustment of ΔL

The effect of θ on the output of an optical discriminator may be found by coherently superposing two equal beams of phase difference θ , thus:

$$\text{Signal out} = \bar{E} = e^{j\omega t} + e^{j(\omega t + \theta)}$$

$$\text{Power out} = I = (\bar{E} \cdot \bar{E}^*) = \left[e^{j\omega t} + e^{j(\omega t + \theta)} \right] \left[e^{-j\omega t} + e^{-j(\omega t + \theta)} \right] \quad (3.5)$$

Note: \bar{E}^* is complex conjugate of \bar{E}

So

$$I = 2 + e^{j\theta} + e^{-j\theta} = 4 \cos^2 \frac{\theta}{2}$$

Normalized power out is thus

$$I = I_0 \cos^2 \frac{\theta}{2} = I_0 \cos^2 \left(\frac{\pi \Delta L}{c} \nu + \frac{\varphi}{2} \right) \quad (3.6)$$

which is the same form as Eq. (2.4).

Since $\nu = \nu_0 + \nu_D$, using the periodic property of $\cos^2 \theta/2$ and the bias term φ to incorporate the ν_0 term we may also write Eq. (3.6) as

$$I = I_0 \cos^2 \left(\frac{\pi \Delta L}{c} \nu_D + \frac{\varphi}{2} \right) \quad (3.7)$$

or equivalently,

$$I = \frac{I_0}{2} \left[1 + \cos \left(\frac{2\pi \Delta L}{c} \nu_D + \varphi \right) \right] \quad (3.8)$$

3.1 THE DIFFERENTIAL INTERFEROMETER OPTICAL DISCRIMINATOR

This subsection describes the features of the angle-compensated differential interferometer discriminator, and provides an analytical foundation so that its basis of operation may be understood from both a quantitative and a qualitative viewpoint.

Figure 3-1 illustrates the simplest form of differential interferometer. It consists of mirrors M_a and M_b , beam splitter S , and a dielectric element of length ℓ_{a1} and refractive index n_{a1} in one arm. From geometrical optics it may be shown that

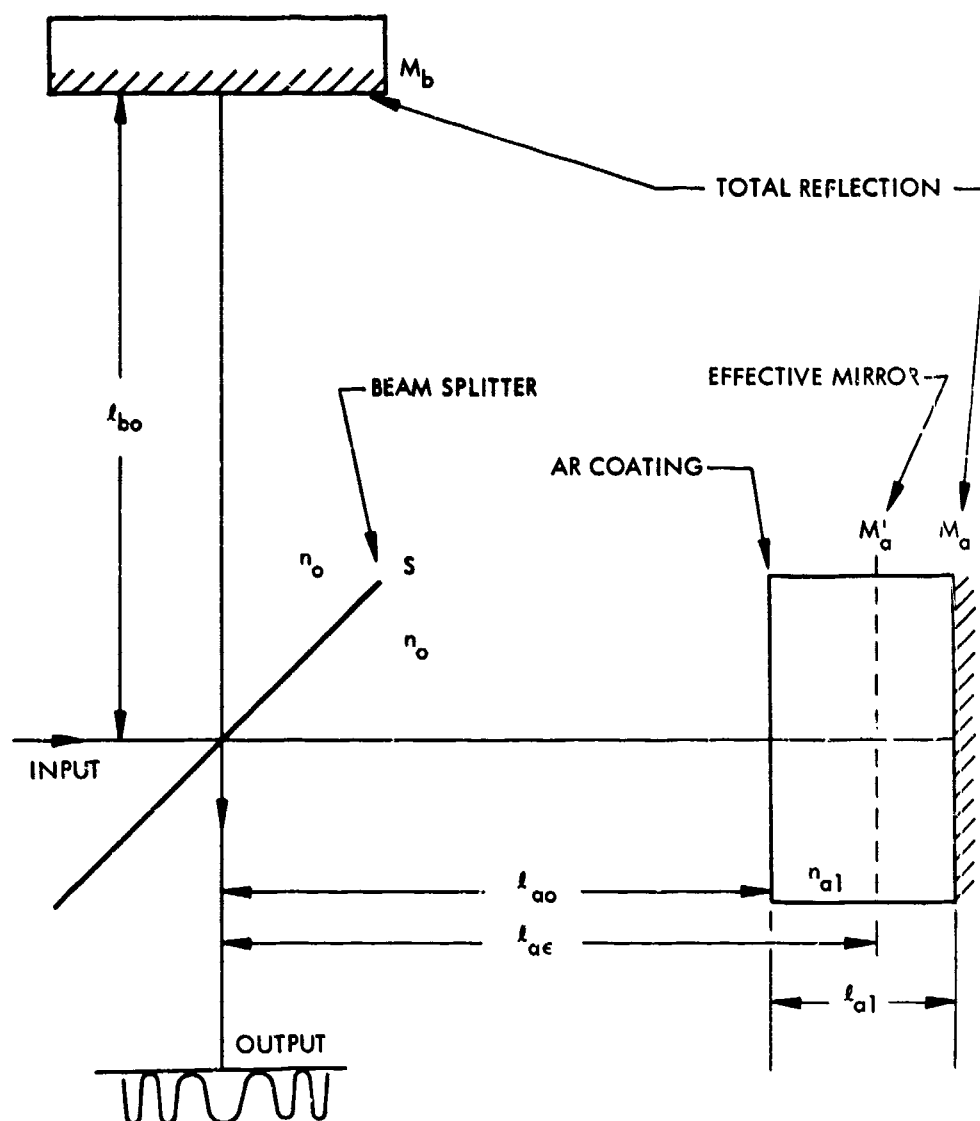


Fig. 3-1 The Singlet Differential Interferometer

mirror M_a takes the apparent position M'_a at a depth of l_{a1}/n_{a1} in the dielectric for viewing angles near the normal (i. e., assuming ϵ is the angle to the normal, where the approximation $\sin \epsilon \approx \epsilon$ is valid). Now if l_{ae} , the distance from the beam splitter to the apparent mirror position M'_a is set equal to l_{bo} , the distance from the beam splitter to mirror M_b , the mirrors will appear to be geometrically equidistant from the beam splitter. Yet from the figure it is apparent that the optical path lengths are quite different. Indeed, analysis shows that the optical path difference ΔL for normal incidence is given by

$$\Delta L = 2\ell_{a1} \left(n_{a1} - \frac{1}{n_{a1}} \right) \quad (3.9)$$

Since $\ell_{a\epsilon} = \ell_{bo}$ for small angular deviations from the normal to the dielectric, the device is insensitive to angular variations in the input beam. The differential interferometer features one other important attribute: analysis, confirmed by experiment, shows that for small angles (say, within ± 6 deg of the interferometer axis) a ray of small dimensions will track and interfere with itself after traversing both arms. This means that the device may be employed in convergent or divergent light, a feature also confirmed in the laboratory.

Insensitivity of device response (i. e., interference pattern change) to input beam angular variations as well as input beam convergence or divergence may be controlled through the use of additional dielectric elements. In a semiquantitative sense one can express the change in optical path difference, ΔL , as a power series in $\sin \epsilon$:

$$\Delta L(\epsilon) = a_0 + a_2 \sin^2 \epsilon + a_4 \sin^4 \epsilon + \dots \quad (3.10)$$

where, because of symmetry, only even terms in $\sin \epsilon$ exist in the series. For each optical element of different refractive index included in the interferometer one can, by an arbitrary but judicious choice of parameters, configure the system so that one of the coefficients in Eq. (3.10) is zero (or any specified value). Thus a singlet interferometer may be designed so that

$$\Delta L(\epsilon) = a_0 + a_4 \sin^4 \epsilon + \dots \quad (3.11)$$

and a doublet interferometer so that

$$\Delta L(\epsilon) = a_0 + a_6 \sin^6 \epsilon + \dots \quad (3.12)$$

The term a_0 represents the constant path difference, which, for a singlet differential interferometer, is given by Eq. (3.9). Parameters of a singlet or doublet system and values for the coefficients in Eqs. (3.11) and (3.12) are derived in Appendix B.

It is shown that a singlet differential interferometer gives

$$\begin{aligned} \frac{\Delta L(\epsilon)}{2} \approx l_{ao} - l_{bo} + n_{a1} l_{a1} - \frac{1}{2} \left(l_{ao} - l_{bo} + \frac{l_{a1}}{n_{a1}} \right) \sin^2 \epsilon \\ - \frac{1}{8} \left(l_{ao} - l_{bo} + \frac{l_{a1}}{n_{a1}} \right) \sin^4 \epsilon \quad (3.13) \end{aligned}$$

Setting the coefficient of $\sin^2 \theta$ equal to zero yields

$$\Delta L(\epsilon) \approx 2 l_{a1} \left(n_{a1} - \frac{1}{n_{a1}} \right) + \frac{1}{4} \frac{l_{a1}}{n_{a1}} \left(1 - \frac{1}{n_{a1}^2} \right) \sin^4 \epsilon \quad (3.14)$$

where

$$l_{bo} = l_{ao} + \frac{l_{a1}}{n_{a1}} \quad (3.15)$$

Comparing Eqs. (3.14) and (3.15) with Eq. (3.9) it can be seen that Eq. (3.15) is the condition for making the distance from the beam splitter to M_b and the apparent position of M_a equal.

The off-axis performance of the singlet interferometer may be established from Eq. (3.14) by assuming 3 realizable parameters and solving for ϵ . For this purpose assume that

$$\Delta L(o) = 1 \text{ cm}$$

$$n_{a1} = 1.5$$

$$\lambda_o = 0.6328 (10^{-4}) \text{ cm}$$

and solve for ϵ at $\Delta L(\epsilon) - \Delta L(o) = \lambda_o/10$. Then $\ell_{a1} = 0.60 \text{ cm}$ and $\epsilon = 5.9 \text{ deg}$.
At $\Delta L(\epsilon) - \Delta L(o) = \lambda_o/100$, $\epsilon = 3.3 \text{ deg}$.

3.2 DIFFERENTIAL INTERFEROMETER - IMPLEMENTATION

The differential interferometer (see Fig. 3-2) is basically a Michelson interferometer with a phase delay element D placed in one beam path. This system requires two precision mirrors A and B, a beam splitter C, and etalon D. The mirrors are placed mutually perpendicular and their relative positions and orientations to the beam splitter C are controlled by the wedge system F and the tilt plate system G. Fine adjustment of mirror B is accomplished by the bias control H. A second beam splitter E is used to provide a reference beam to the photomultiplier system, which is normally attached to J and K. An iris provides an aperture for limiting the incoming beam. Behind the iris is a window to prevent convection currents from creating thermal instabilities in the system. The entire system is contained in a heavy aluminum housing (the cover plate has been removed in Fig. 3-2) and encapsulated in polyethylene foam that serves as an adiabatic shield.

3.2.1 Wedge Assembly

The distance of mirror A from beam splitter C is controlled by the wedge system shown in Fig. 3-3. Distance of mirror A from plate L is determined by the position of wedge F', which is controlled by translation screw O. Stainless steel wedge F' contacts surfaces of plate L and mirror support F' at four points via 10-mil-thick cadmium shims M and N. Cadmium provides an excellent bearing surface and eliminates galling of the metal surface.

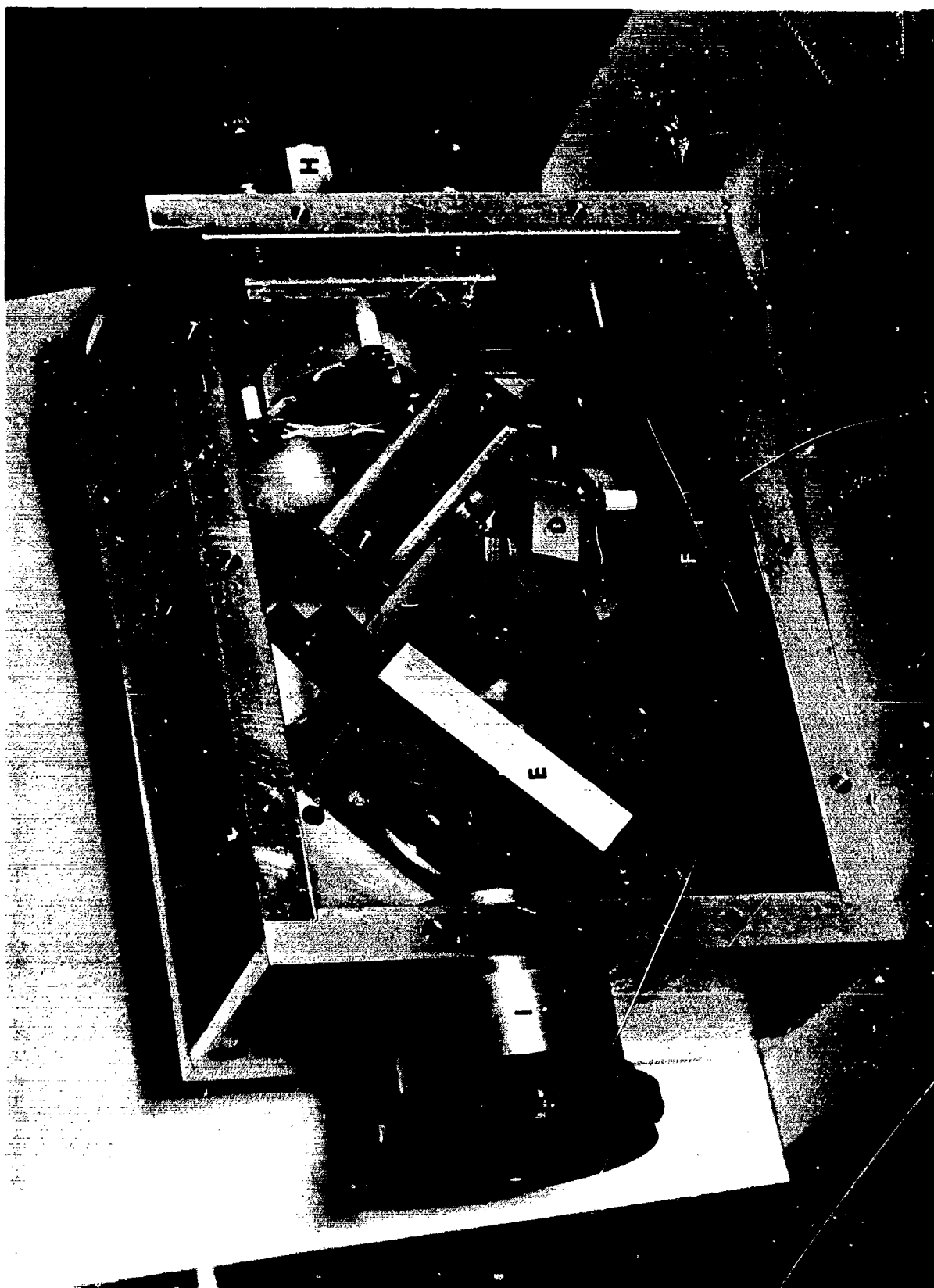


Fig. 3-2 Differential Interferometer Optical Discriminator

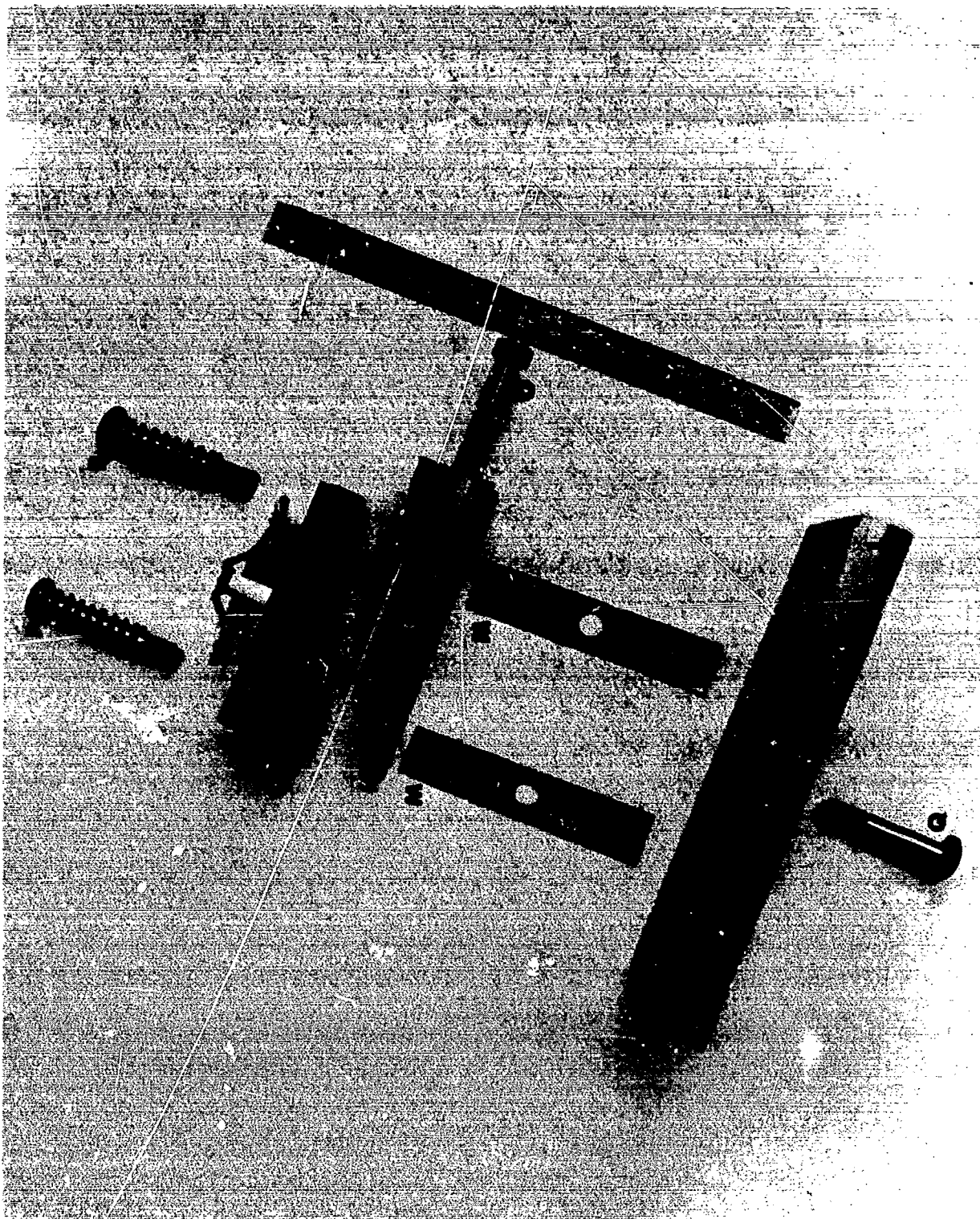


Fig. 3-3 Wedge Assembly

The wedge system is loaded by springs and screws P , and is locked into place by screw Q after the adjustment is complete. Mirror support F is prevented from skewing on wedge F' by guide screws and washers, and a small spring and pin. This ensures proper alignment of the wedge system.

3.2.2 Bias and Tilt Plate Assembly

Tilt plate G , shown in Fig. 3-2, is adjusted by three two-stage coaxial differential screws, which allows the plane of mirror B to be tilted with respect to the beam splitter and mirror A . In addition, when all three differential screws are adjusted simultaneously, a fine adjustment of the relative path length is obtained, as opposed to the coarse adjustment with the wedge system.

The two-stage coaxial differential screw is shown in Fig. 3-4. It consists of a fine control knob R , brass screw S , coarse control knob T , spring U , stainless steel screw V , and locking clamp and screw W and X. Screw S has a 30-threads/in. internal thread. Screw V mates with the latter thread and is rigidly attached to bias plate G' and the tilt plate G. When assembled (see Y in Fig. 3-4) the system is loaded by spring U between plate G and the housing. If the coarse knob is rotated, one obtains an effective 30 threads/in. Coupling of two threads, one with n_1 threads/in. and the other with n_2 threads/in. , into a differential screw assembly provides, effectively

$$\text{threads/in.} = \frac{n_1 n_2}{n_1 - n_2}$$

Upon rotating the fine control knob R , an effective $32 \times 30 / (32 - 30) = 480$ threads/in. is obtained. Screw X is tightened on clamp W just enough to prevent knob T from turning when knob R is rotated.

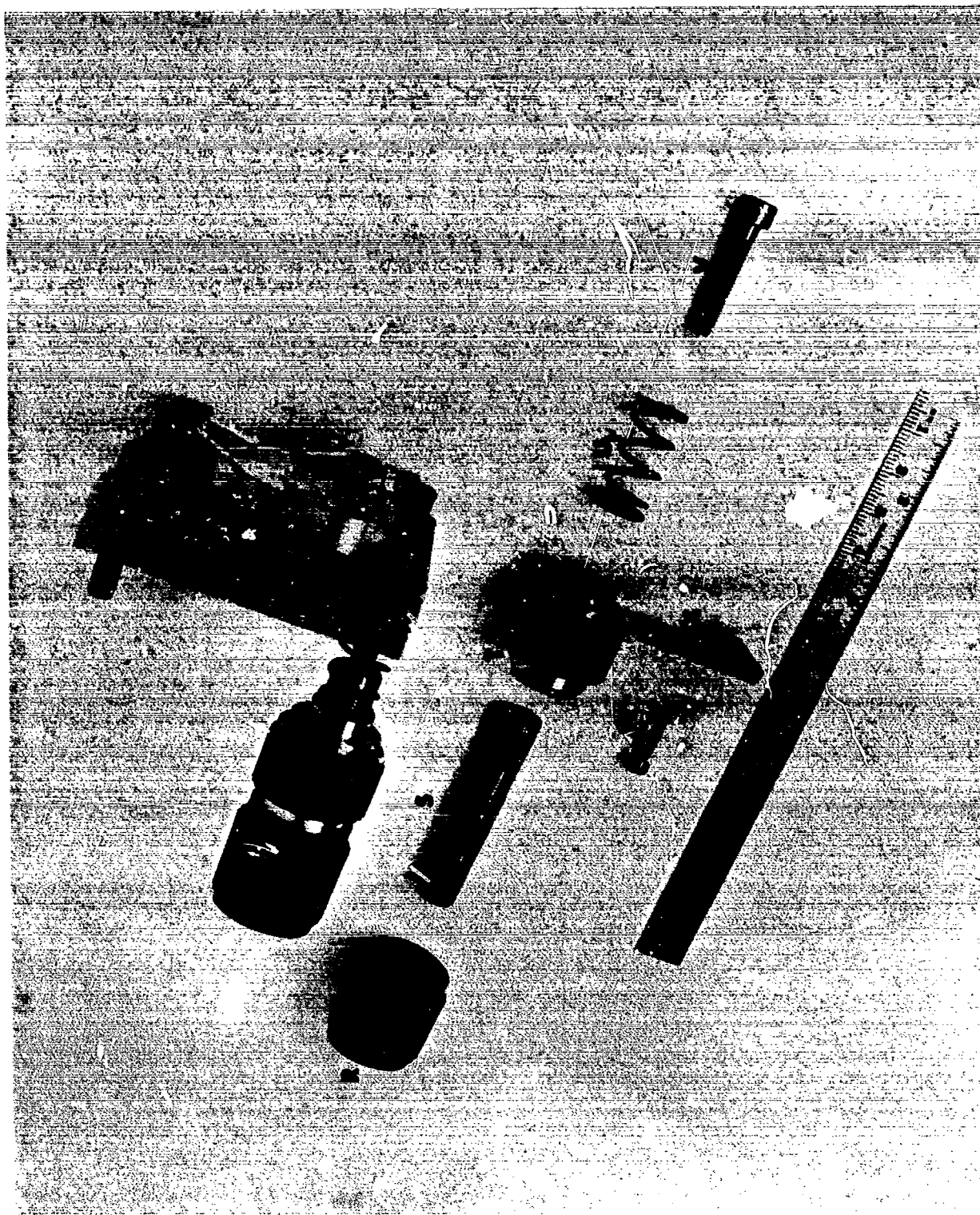


Fig. 3-4 Bias, Tilt Plate, and Differential Screw Assembly

Tilt plate G is suspended at three points located at the vertices of a 45-deg right triangle. At each point is a differential screw as described above. This arrangement offers the advantage of orthogonal control of the fringe pattern.

3.2.3 Bias Control

Minute adjustment of differential path ΔL is accomplished by means of the bias control. This consists of a knob, screw and S-shaped spring (see H in Fig. 3-2). The spring is made of beryllium-copper and is mounted on the back face of the bias plate (see G' in Fig. 3-4). By rotating the bias knob, one can compress the spring and distort slightly the bias plate (i. e. , a differential spring action) thus changing the position of the mirror. No distortion of the mirror occurs because it is mounted at three points equally spaced along the mirror circumference. Thus, a translation of the mirror occurs along an axis perpendicular to the mirror face.

3.2.4 Beam Splitters and Mirrors

The beam splitter C in Fig. 3-5 consists of two optical flats of equal thickness, one with antireflection coatings on both sides, the other with an antireflection coating on one side and a 50-percent reflecting surface on the other. The AR coatings are designed for light of wavelength 6328A incident at 45-deg to the surface. The two optical flats are separated by three paper inserts, equally spaced along the circumference for symmetry. Also for symmetry, the 50-percent reflecting surface is placed adjacent to the other optical flat.

Spring clamps are used to mount the beam splitter elements. Each clamp has two spring legs that contact the optical element and that are covered by plastic tubing to prevent scratching the surface. A third leg extends over the optical element, but is not in contact with it, and prevents the optical elements from jarring loose if accidentally shocked. The support posts are also covered with plastic tubing.



The mirrors on the wedge and bias-tilt plate assemblies (A and B in Fig. 3-5) are similarly mounted. Each mirror is set on three equally spaced cadmium strips along the circumference of the mirror and below the spring clamps. The mirrors consist of 1.5-in. -diameter fused silica optical flats with a high-reflectivity hard coating (greater than 99.9 percent at 6328A) and an antireflection coating on the second surface.

One mirror was originally intended to be used as a second surface mirror so that the substrate might be employed as the delay element. Due to the fact that the antireflection coatings were imperfect, undesirable constructive and destructive interference effects occurred. This element was finally used as a first surface mirror and an etalon was placed in one beam path as the delay element, a change which reduced unwanted interference effects. However, it did not eliminate fringe distortion. Figure 3-6 shows the assembled mirror systems.

3.2.5 Delay Element

The delay element consists of two 6.0-mm-thick crown glass etalon compensating plates (index of refraction = 1.52) that have been optically contacted to reduce the number of reflecting surfaces. The composite etalon is clamped in a holder with paper shims between the metal and glass (see D in Fig. 3-2) and mounted to the bottom plate of the housing by a single screw that allows the angle of the etalon to be adjusted. For the present series of experiments, the etalon was tilted 7 deg to the transmitted beams to eliminate unwanted reflections in the system. This tilt results in an effective path length of 12.1 mm for the transmitted beams.

3.2.6 Iris and Window

An iris was installed to restrict the size of the incoming laser beam. This permits additional means of controlling unwanted reflections within the interferometer. The aperture diameter employed was usually about 6 mm during the Doppler wheel tests and larger for the gas gun tests where better angular control of the return beam was possible.

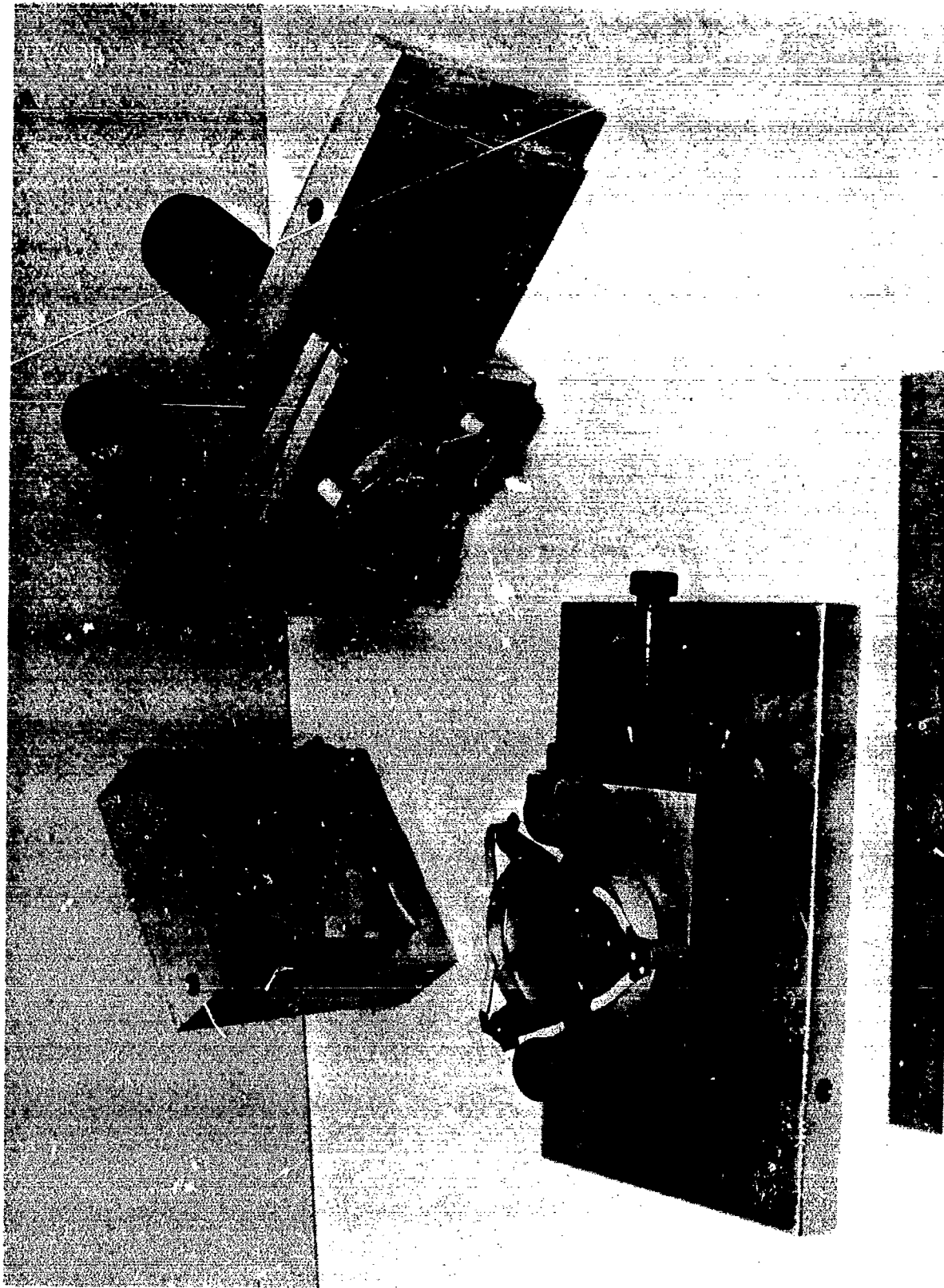


Fig. 3-6 Assembled Mirror Systems

A window is present just behind the iris to prevent convection currents from entering the system and influencing the stability of the system. The window is tilted slightly to eliminate reflections.

3.2.7 Photomultiplier System

The photomultiplier system (Fig. 3-7) is connected directly to the interferometer housing at J and K in Fig. 3-2 by means of two expandable sleeves and consists of two RCA 7850 photomultipliers housed in light-tight aluminum tubes. The photomultipliers are fitted into standard sockets with voltage dividers wired directly to the sockets.

It was found that the voltage dividers dissipated sufficient heat to create convection currents between the photomultiplier tubes and their housings. When in actual use the photomultipliers were positioned vertically, which resulted in a chimney effect causing convection currents within the interferometer. To eliminate this problem, strips of foam rubber were wedged between the photomultipliers and their housings.

3.2.8 Thermal Insulation and Stability

Temperature changes of the surrounding environment were found to be a source of instability, a problem that was largely eliminated by encapsulating the interferometer in 0.75-in. -thick polyethylene foam (see Fig. 5-5). This reduced the bias drift to $\pm 1/30$ of a fringe over a 5-min interval of time, corresponding to a phase displacement of ± 0.2 rad.

One of the more temperature sensitive portions of the interferometer is the bias spring and screw. The screw protrudes outside the foam and presents a low-resistance heat conduction path to the outside. Temperature variation of the spring is suspected as a major cause of bias drift.

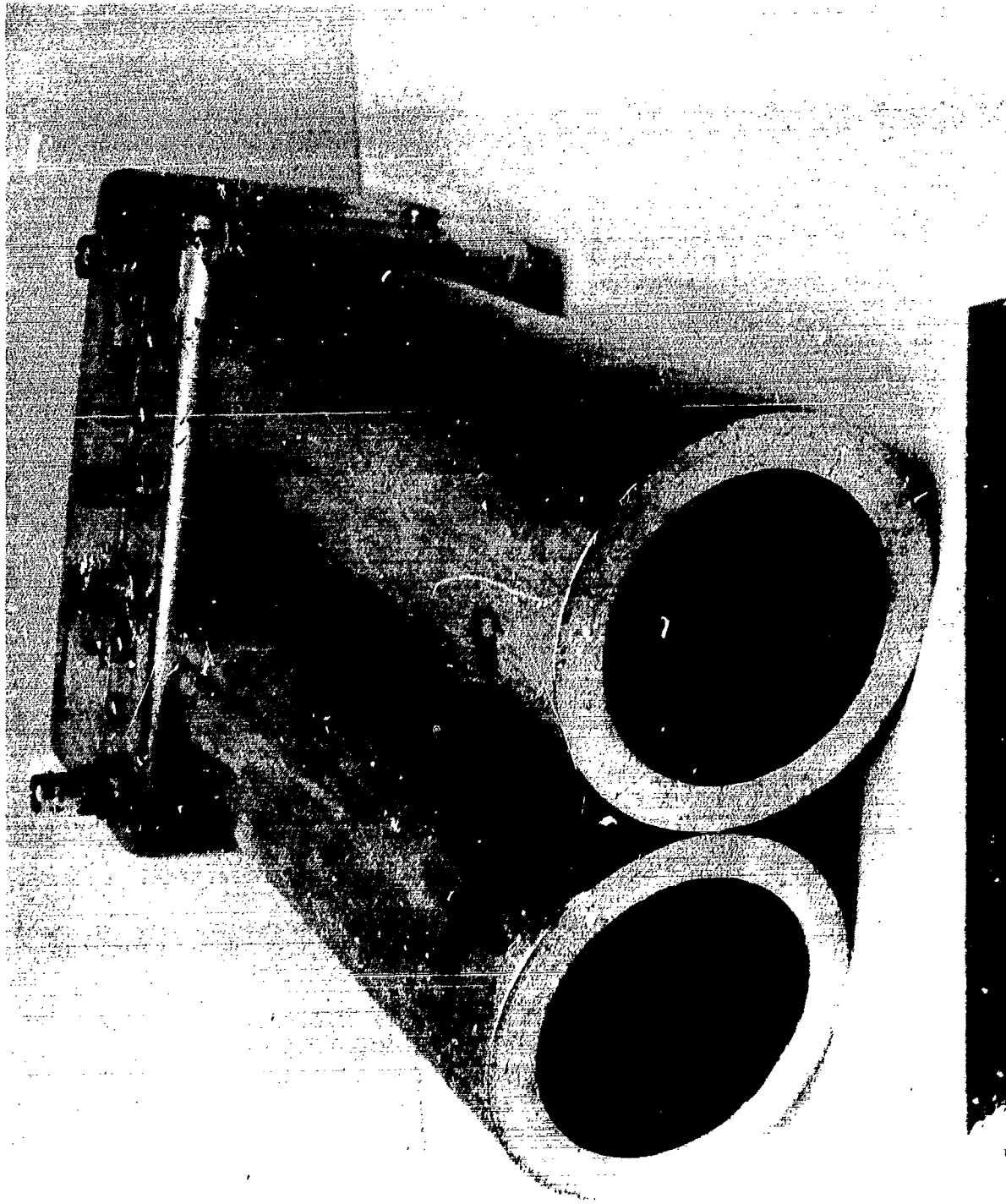


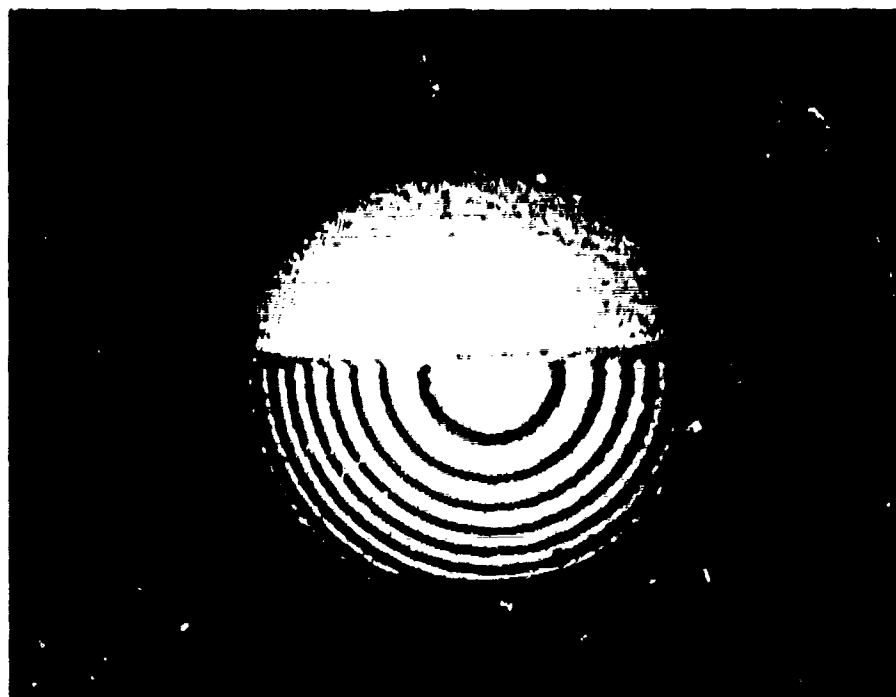
Fig. 3-7 Ratio Amplifier Electronics and Photomultiplier Housing

3.2.9 Initial Adjustment

The interferometer is adjusted initially on an optical bench. Using a pinhole aperture, a narrow laser beam is sent to the interferometer. The output beam is observed at K in Fig. 3-2 using a sheet of paper and with the photomultiplier system removed. When the tilt system is improperly adjusted, two spots appear on the screen. By adjusting the three coarse differential screws, these two spots can be made to coincide. At this point, the two mirror planes and beam splitter plane intersect along an imaginary straight line.

The pinhole is removed and a converging lens is inserted in the light beam in front of iris to expand the field of view and provide a wider fringe pattern at K in Fig. 3-2. The wedge system F is then adjusted by means of the translation screw until the fringes reach a maximum breadth. When properly adjusted the two apparent beam paths are approximately equal. The desired wedge adjustment can be locked in place by the screw (Fig. 3-3). At this point the converging lens can be removed and the fringe pattern will be relatively insensitive to the angle of the incident beam. This adjustment is essential in preventing angular variations of the laser beam from affecting the interferometer output.

Figures 3-8(a) and 3-8(b) are interference patterns obtained with a preliminary mockup differential interferometer using convergent light. To obtain these illustrations the interferometer was set for minimum angular sensitivity with the etalon in the adjustable arm. The etalon was then withdrawn halfway so that the interference pattern central fringe [observed through the etalon in the top half of Figs. 3-8(a) and 3-8(b)] could be compared with the interference pattern without the etalon (bottom half of the figures). Through the etalon the differential path length is nearly 10 mm and approximately 3 mm without it. Yet, the central fringe of the interferometer pattern for the differential path including the etalon element is approximately an order of magnitude greater than for the differential path without the etalon. The only difference between Figs. 3-8(a) and 3-8(b) is in the adjustment of the bias. Bias for the interference pattern of



(a) Maximum Central Fringe Intensity



(b) Minimum Central Fringe Intensity

Fig. 3-8 Effect of Etalon on Fringe Patterns

Fig. 3-8(a) was adjusted for maximum central fringe intensity; in Fig. 3-8(b), it was adjusted for minimum central fringe intensity. Extinction over the central fringe including the etalon [upper half of Fig. 3-8(b)] is not good due to the lack of quality optics employed with the optical mockup.

Finer adjustment of the relative path length can be made by simultaneously adjusting the three fine controls of the bias-tilt assembly. The fine controls are also used to position the fringe pattern more accurately.

The bias control and iris are adjusted to yield an output intensity approximately halfway between complete extinction and complete brightness. At this point the paper screen is removed and the photomultiplier system is attached to the interferometer. Further adjustment is done using the electronics system and an oscilloscope. The bias is then adjusted so that the ratio amplifier output is about $1/4$ of the way between minimum and maximum voltages. When the sample beam is directed to the interferometer, a positive Doppler shift (frequency increase) will shift the ratio amplifier output towards the maximum. As a result of this adjustment, response of the system is generally constrained to the linear region of the $\cos^2(\theta/2)$ curve during a shock event.

Section 4 RATIO AMPLIFIER

4.1 BACKGROUND

The optical discriminator is an optical frequency analog of the radio frequency FM discriminator. A change in frequency of the input signal to the discriminator produces a corresponding change in amplitude of the output signal. Input signal amplitude fluctuations (noise) also appear in the output signal since there is no practical optical analog of the fast clipping or saturation circuits usually found just ahead of the RF discriminator to ensure constant input amplitude. Therefore, input amplitude variations are removed from the signal electronically, after optical detection.

Discriminator input intensity variations are sensed by a reference photomultiplier. Reference signal current out of the reference photomultiplier may be characterized by

$$I_r(t) = K_r I_0(t) \quad (4.1)$$

where $I_0(t)$ is the fluctuating input intensity and may vary with sample reflectivity, optical link gain, etc. K_r is a constant determined by photomultiplier gain and reflectivity of the reference beam splitter.

Optical discriminator output intensity variations are due to both frequency discrimination and input amplitude variations. Current out of the signal photomultiplier may be characterized by

$$I_s(t) = K_s I_0(t) \cos^2 \left(\frac{\pi \Delta L}{c} \nu_D(t) + \frac{\varphi}{2} \right) \quad (4.2)$$

where K_s is determined by losses in the discriminator and gain in the photomultiplier.

Input intensity $I_o(t)$ is eliminated by taking the ratio of $I_s(t)$ to $I_r(t)$

$$I(t) = \frac{I_s(t)}{I_r(t)} = \frac{K_s I_o(t) \cos^2 \left[\frac{\pi \Delta L}{c} \nu_D(t) + \frac{\phi}{2} \right]}{K_r I_o(t)} \quad (4.3)$$

The ratio is thus a time-varying function only of the Doppler frequency.

A fast ratio amplifier has been designed to implement this process.

4.2 BREADBOARD RATIO AMPLIFIER

The breadboard ratio amplifier is shown in Fig. 4-1 and schematically in Fig. 4-2. Signal and reference photomultipliers V1 and V2 may be considered current sources with output currents I_r and I_s above. The photomultiplier anodes are shunted by diodes D1 and D2, which have nearly ideal voltage-current characteristics. The voltage across the diodes is approximately:

$$V_D \approx \frac{kT}{q} \ln I_D \quad (4.4)$$

Signal and reference voltages produced across diodes D1 and D2 are presented to the bases of two transistors, Q1 and Q2, connected as an emitter-coupled differential amplifier. The current I_C in the collector of Q2 is kept constant with the addition of Q3 and therefore reflects a voltage across the base-emitter junction of Q1 which is approximately

$$\begin{aligned} V_{BE1} &= (V_{D1} - V_{D2} + V_C) = \frac{kT}{q} [(\ln I_s - \ln I_r) + \ln I_C] \\ &= \frac{kT}{q} \ln \left(I_C \frac{I_s}{I_r} \right) \end{aligned}$$

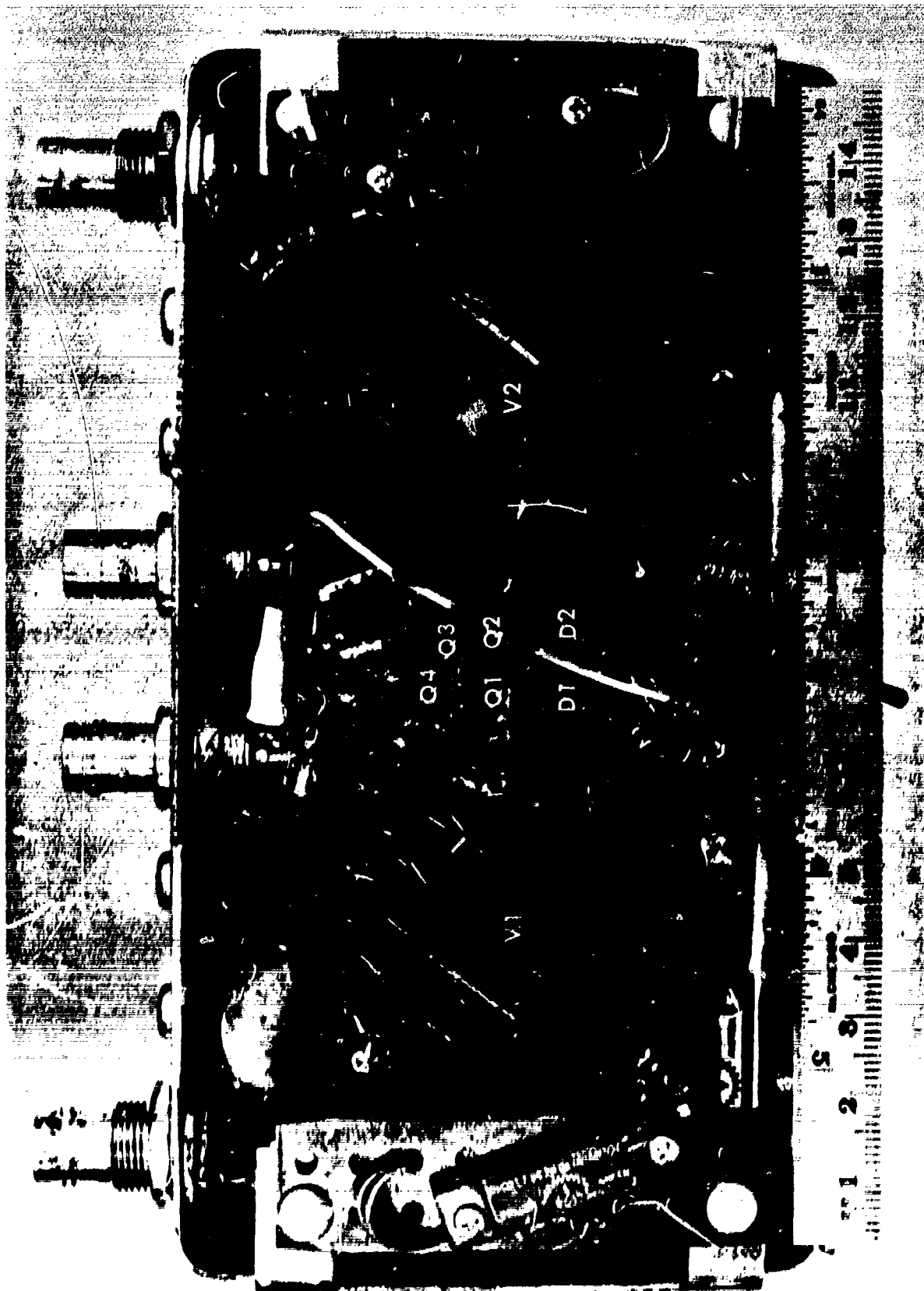


Fig. 4-1 Ratio Amplifier Electronics

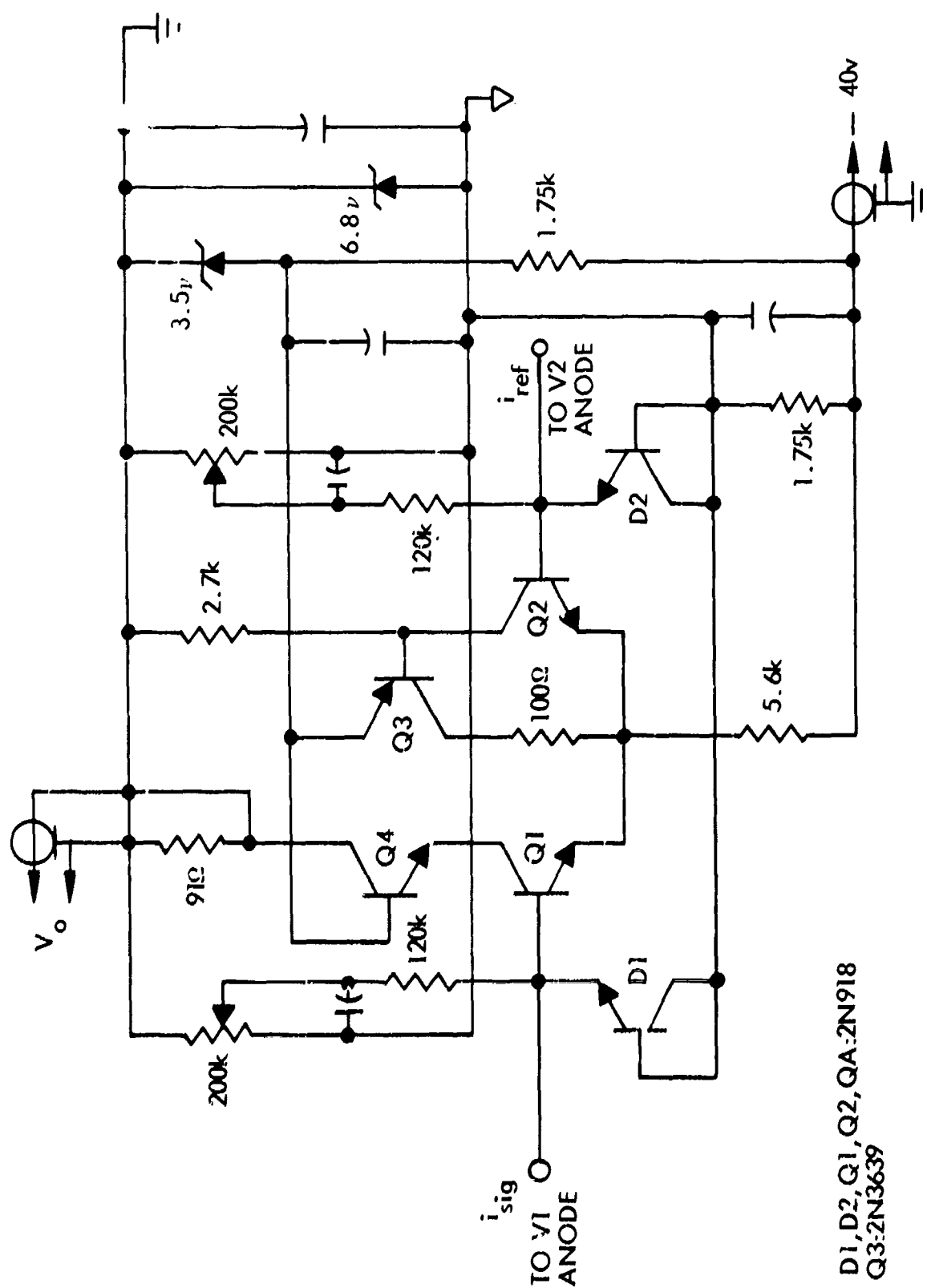


Fig. 4-2 Ratio Amplifier Schematic

Collector current in Q1 will be approximately:

$$I_{C1} \cong I_{E1} \cong K_I \exp \left(\frac{q}{kT} V_{BE1} \right) \cong K_I \left(I_C \frac{I_S}{I_R} \right) \quad (4.6)$$

Transistor Q4 forms an amplifier with nearly unit current gain that lowers the collector impedance of Q1 giving better high frequency response for a reasonable output voltage and resistance.

The ratio amplifier output signal will therefore be

$$V = R_O K_I I_C \frac{I_S}{I_R} = R_O K_O \cos^2 \left(\frac{\pi \Delta L}{c} \nu_D + \frac{\varphi}{2} \right) \quad (4.7)$$

where the scale factor K_O can be determined during system calibration by adjusting φ through 2π radians and measuring the maximum excursion of V .

4.3 LINEARITY

Figure 4-3 relates the output voltage of the ratio amplifier to the input currents. Output voltages are noted for input current ratios of 2 to 1, 1 to 1, and 1 to 2. Variations of output voltage for the same current ratio can be attributed to insufficient time to select matched devices and set biases as described below. Failure of key components just prior to final test led to this problem. A partial error analysis has been carried out and offers explanations for the variations.

The calibration data of Fig. 4-3 has been replotted in a somewhat different form in Fig. 4-4. This plot represents a family of curves given by the equation

$$V - V_O = \frac{M}{I_R} (I_S - I_O) \quad (4.8)$$

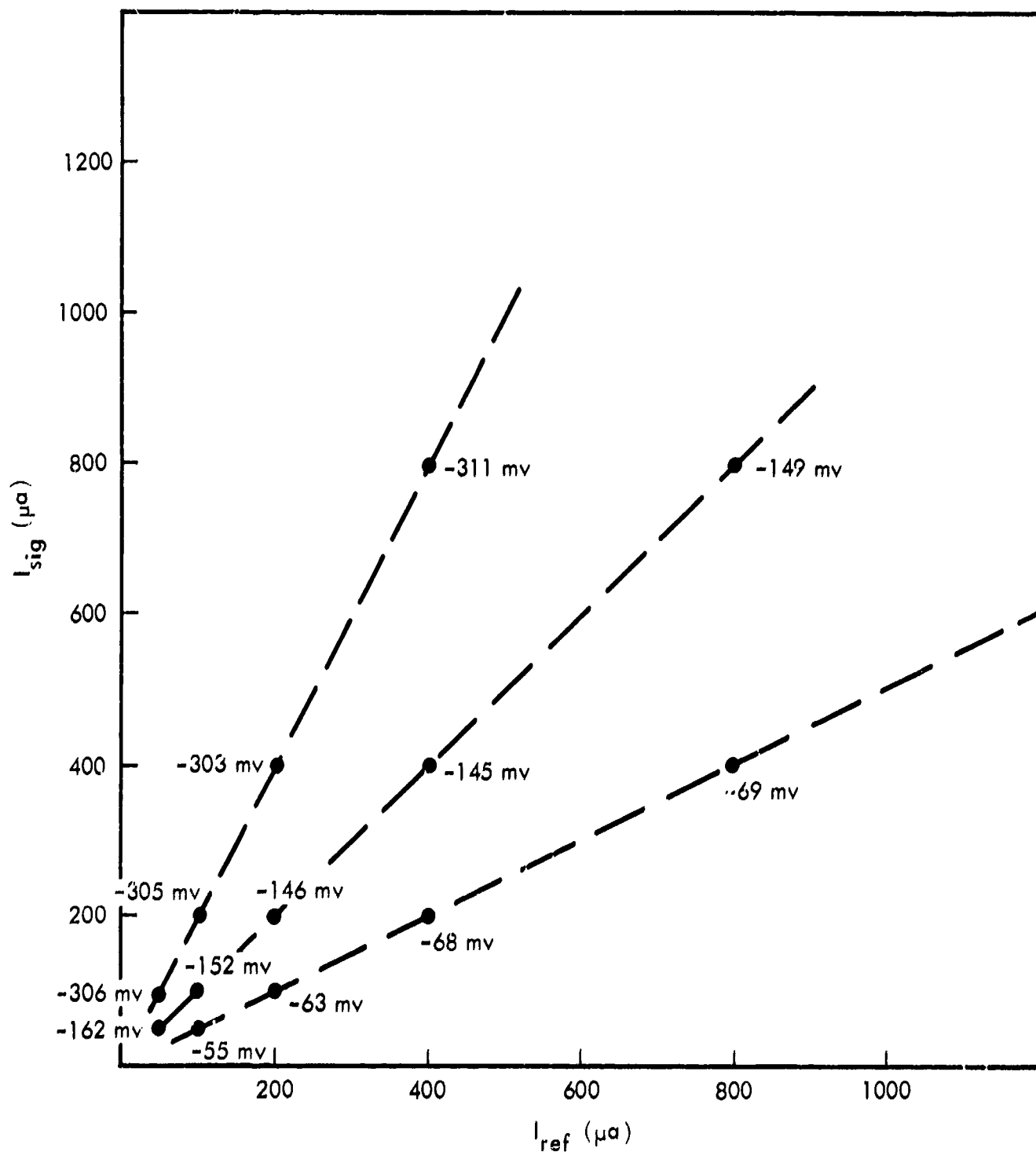


Fig. 4-3 Ratio Amplifier Calibration Curve

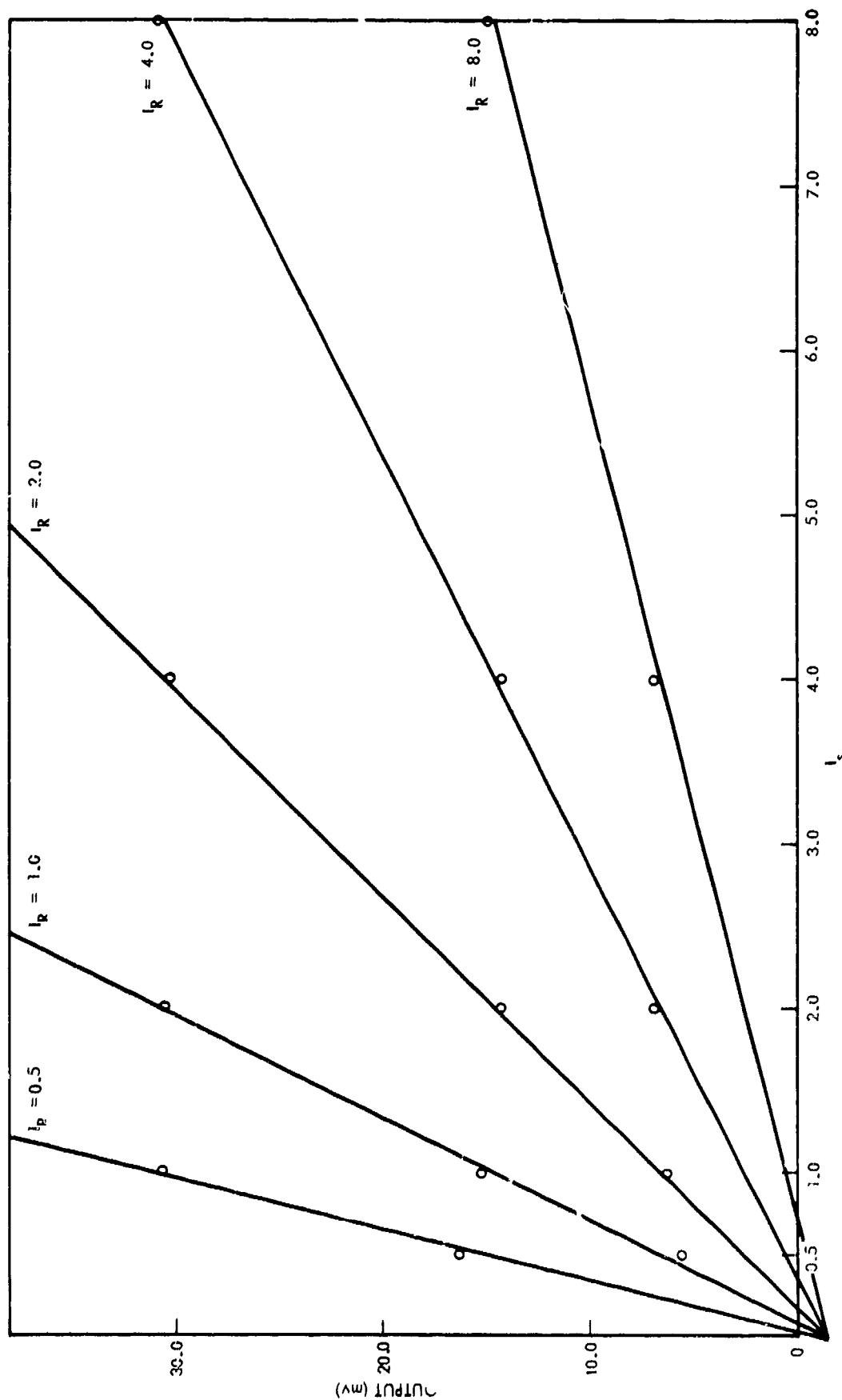


Fig. 4-4 Ratio Amplifier Calibration Curves

rather than by Eq. (4.7). The value of I_0 is essentially zero, but that of V_0 is about 14 mv and is not negligible. The result of using Eq. (4.7) for velocity calibration purposes is to calculate a slope which is too small. The magnitude of the error varies with the particular excursion of the signal over the set of characteristics of Fig. 4-4. Its magnitude may be estimated by considering the experimental cases in which I_R remains fixed and the excursion is over one curve of the family. Then, for a small signal excursion about the 150-mv level, an error of $14/150$ or about 10 percent results. For a signal excursion of about 180-mv centered about the 150-mv level, the slope error varies from a high of $14/150 - 90 = 14/60 = 25$ percent to a low of $14/150 + 90 = 14/240 = 6$ percent.

These calibration errors result solely from the fact that Eq. (4.8) rather than Eq. (4.7) describes the behavior of the ratio amplifier. The effect is that of a built-in negative bias in the ratio amplifier output.

Through inclusions of a distributed intrinsic series resistance, the departure of the diodes D1 and D2 from an ideal voltage-current characteristic [Eq. (4.4)] results in errors that are a function of input current and, therefore, are uncalibratable. To minimize these errors, D1 and D2 are transistors that are diode connected. The gain of the transistor shifts the operating current to a point where series resistance effects are minimized. Transistors with characteristics matched over the current range must also be used.

From the analysis of error sources and from reasonable estimates of ratio amplifier performance with properly matched components, a significant improvement in amplifier performance is possible with a modest additional development effort.

4.4 ELECTRONICS SETUP PROCEDURE

4.4.1 Ratio Amplifier

The ratio amplifier operates best with currents in both channels between 200 and 800 μa . After the optics are set up and a stable beam intensity enters the interferometer, a reference-current resistor is connected to the anode pin of the signal-channel photomultiplier to supply 400 μa from the 40-v power supply. The gain (high-voltage supply) of the reference photomultiplier is then adjusted to obtain an output from the ratio amplifier of -150 mv. This corresponds to a ratio of 1 between the two channels, and gives a reference-channel current of 400 μa .

Next the power supply for the signal channel is turned on. With the interferometer adjusted for maximum fringe visibility (by tilt adjustment to give good extinction on minimum bias), the bias adjustment is set on maximum intensity. The signal channel gain is adjusted to give an amplifier output of 300 mv (2:1 signal-to-reference ratio), giving a maximum signal channel current of 800 μa .

The output voltage of the ratio amplifier is displayed on a Hewlett-Packard 175A oscilloscope with a 1751A plug-in vertical preamp set for 50 mv/div. Since Doppler shifts are measured as close as possible to the 50-percent bias point, this allows the ratio amplifier to operate near its optimum point of operation (see Fig. 4-3).

4.4.2 Intensity Monitor

The intensity monitor consists of a photomultiplier mount containing an RCA 7850 tube, monitoring the approximately 10-percent pickoff reflected from a microscope slide inserted in the beam before its entry into the interferometer (see Fig. 5-8). The output from this photomultiplier was fed directly into a Hewlett-Packard 175A oscilloscope with a 1752A plug-in vertical preamp set to the 10-mv/div scale. To retain good bandwidth properties, the scope input was shunted with a 75-ohm cable termination resistor.

This combination provided a signal of 75-mv scope input for 1-ma photomultiplier output. To stay in the linear region of the tube, operation was normally in the range of 35 to 40 mv, or 0.5 ma. This monitor served to spot any major changes in the intensity of the input beam to the interferometer that might invalidate any reading from the ratio amplifier. The ratio amplifier responds normally (ratio appears unchanged) if the input beam is reduced in intensity by no more than a factor 2 or 3, but the reading changes markedly for much larger light losses.

4.4.3 Triggering and Timing

The events of interest take place on a time scale of several microseconds, with the initial elastic wave precursor leading the plastic wave by only tens of nanoseconds. The instant of impact of the flyer plate (see 5.3) was selected as a trigger. The impact shorted a pair of insulated leads epoxied into a hole through the sample plate near one edge. The ends, on the impact surface, were ground flush. These leads were connected to a coaxial cable charged to -90 v through a 1-megohm series resistor by a battery. The short circuit caused a fast-rise pulse, -90 v to 0 v, that was used to trigger the oscilloscopes.

The shock wave due to the impact on the sample of the flyer plate required about $1.0 \mu\text{sec}$ to travel to the reflective surface under observation. Two different sweep times were used at various times to observe different parts of the shock phenomenon. A scale of $0.5 \mu\text{sec/div}$ ($5 \mu\text{sec}$ total sweep time) showed a broad picture of the event from inception through 2 or 3 cycles of free-plate vibrations of the sample plate, or spalled portion thereof. The shorter scale, $0.2 \mu\text{sec/div}$ ($2 \mu\text{sec}$ total sweep time), was used to gain better time resolution on the leading edge of the shock wave. When using this time scale, a $0.5 \mu\text{sec}$ trigger delay was used to cancel part of the $1\text{-}\mu\text{sec}$ lead time (shock wave travel time through the sample) and display a longer portion of the event.

Section 5

TECHNICAL EVALUATION

Tests and evaluation of the laser velocimeter have been conducted both in the laboratory, using the test velocity simulator, and in the LMSC Shock Facility (2.5-in. gas gun). Data obtained with the test velocity simulator clearly demonstrate that the laser velocimeter system is potentially capable of accuracies on the order of a few percent. Gas gun data, although preliminary, indicate in a qualitative way the functional capability of the laser velocimeter system: it appears to be fast and capable of good velocity resolution, and system noise appears to be primarily limited to the input noise of the photomultipliers. The latter may be reduced by increasing the laser power. Details of the velocity simulator and of the velocimeter system test results obtained both in the laboratory with the simulator and in the gas gun (measuring shock in aluminum) are presented in this section.

5.1 VELOCITY SIMULATOR

The velocity simulator needed to calibrate the laser velocimeter system is mentioned several times in previous sections without going into the details of the system, or its basis of operation. The basis of its operation is the fundamental principle that an optical signal reflected from a moving mirror becomes Doppler shifted. Figure 5-1 represents a mirror moving with velocity v_n in the direction of the surface normal. A light beam at frequency ν_o at angle α to the normal is reflected by the mirror. It is shown in Section 2 that to first order in v_n/c the incident light beam is Doppler shifted an amount ν_D , given by the expression

$$\nu_D = 2 \nu_o \frac{v_n}{c} \cos \alpha \quad (5.1)$$

Consider the mirror arrangement illustrated by Fig. 5-2. Mirrors M_1 and M_2 are mounted on a high-speed wheel and are oriented at 45 deg to a diameter, as illustrated.

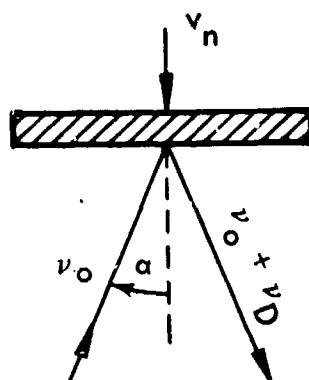


Figure 5-1 Reflection From a Moving Mirror

If the effective radius of a mirror location on the wheel is r_e , then by Eq (5.1) and the geometry of Fig. 5-2

$$\begin{aligned}
 \nu_D &= \pm 2 \nu_o \frac{v_n}{c} \cos \alpha \\
 &= \pm 2 \nu_o \frac{\omega r_e}{c} \cos^2 45^\circ \\
 &= \pm \nu_o \frac{\omega r_e}{c}
 \end{aligned} \tag{5.2}$$

which is the Doppler shift produced by any one mirror. Note that the Doppler shift is independent of the direction taken by the beam as long as $\alpha = 45^\circ$, and that the positive sign goes with counter-clockwise ω . The beam leaving mirror M_2 is parallel in direction to the input beam, but it shifts slightly from side to side as the wheel rotates. By employing a third mirror M_3 to reflect the beam back through the system, two advantages are gained: the magnitude of the Doppler shift is increased to

$$\nu_D = \pm 4 \nu_o \frac{\omega r_e}{c} \tag{5.3}$$

and the output beam appears as a stationary, pulsed source of light with the magnitude of the Doppler Shift being directly proportional to the pulse rate.

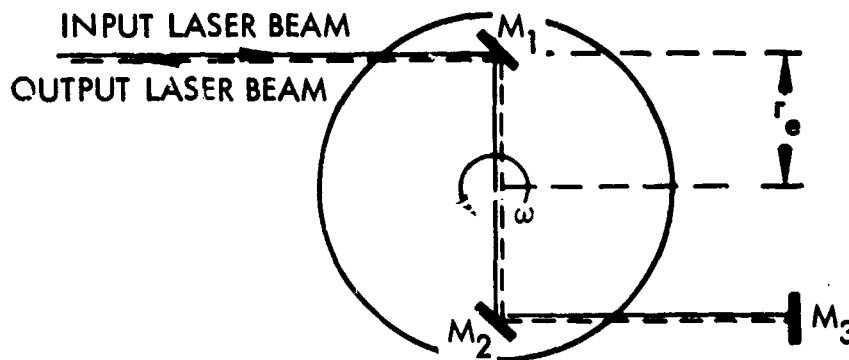


Figure 5-2 Rotating Mirror Doppler Shifter

Parameters of the velocity simulator system illustrated in Fig. 5-3 are $r_e = 9$ cm, $\omega_{\max} = 700$ (21,000 rpm), and $\lambda_o = 6328$ Å. Using these values in Eq. (5.2) yields a maximum $\nu_D = \pm 1.2$ GHz. Calibration range of the velocimeter is thus some 2.5 GHz, corresponding to shock velocities in the range 0 to 10^5 cm/sec (0 to 2450 ft/sec).

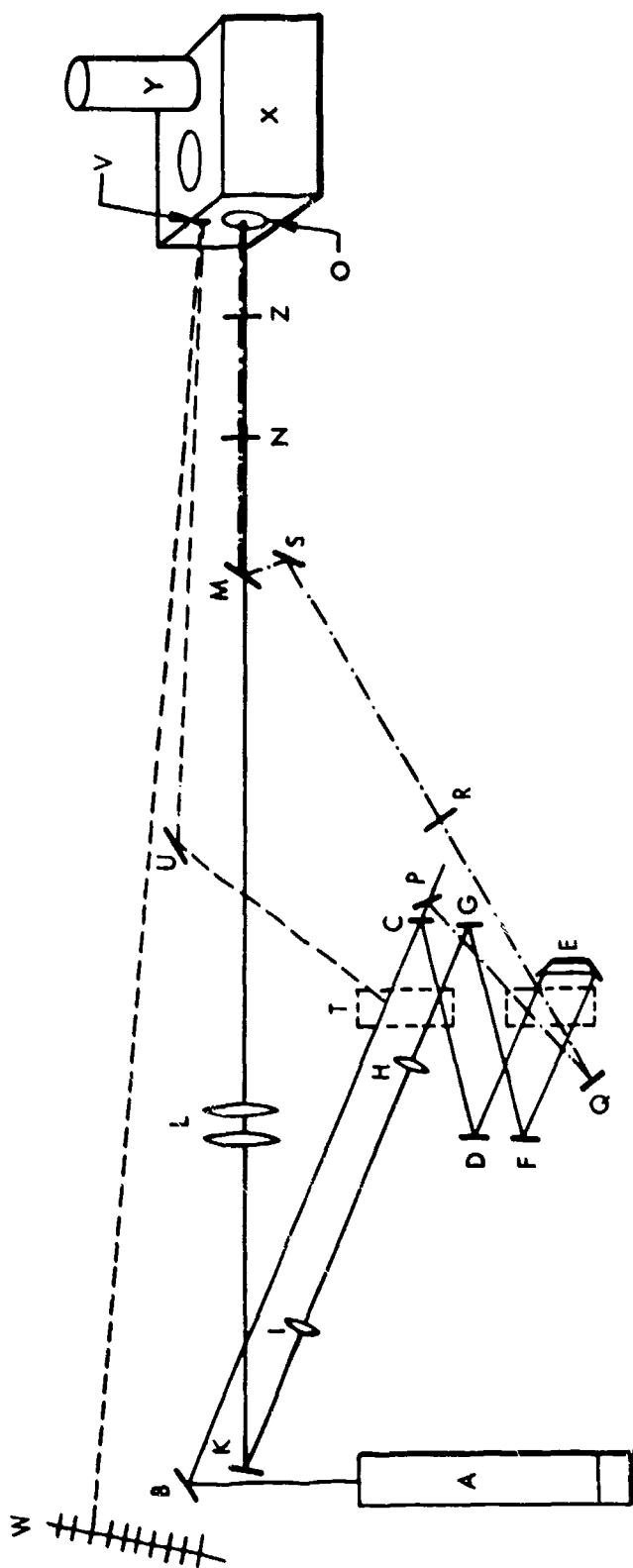
5.2 EXPERIMENTAL WORK WITH THE VELOCITY SIMULATOR

Experiments were run with the velocity simulator to verify the performance of the differential interferometer as compared with theoretical expectations. Initial use of the ratio amplifier was attempted, with a simple optical system (see Fig. 5-4) omitting lenses H and I, reference beam mirrors P, Q, and S, beam splitter M, and polarizers N and R as well as the pickoff mirrors U and V, which were used later to measure more readily the angular position of the interferometer by the reflected spot appearing on scale W. This simple setup gave extremely anomalous results. Ratio amplifier problems prevented initially identifying the underlying cause, and setting up for use of a single photomultiplier with no ratio amplifier proceeded while the latter was being repaired.

To permit use of a single photomultiplier despite drifts in laser output, interferometer, etc., the reference beam system P-Q-R-S-M-N-Z-O was introduced, which provided a reference pulse, twice per wheel revolution, that had experienced no doppler shift. Polarizer N ensured that the reference beam would have the same polarization as the signal beam. For each velocity, polarizer R was adjusted so that the maximum intensities for signal and reference were equal, shifting bias back forth on the



Fig 5-3 Velocity Simulator (Doppler Wheel)



A	laser	O	entrance aperture of differential interferometer
B	mirror on gimbal mount	P	stationary mirror in velocity simulator, for reference beam
C, D	top mirrors on velocity simulator wheel	Q, S	mirror on gimbal mount
E	prism	T	entrance window to velocity simulator
F, G	bottom mirrors on velocity simulator wheel	U	mirror
H	first spot-wander control lens	V	mirror on front of interferometer
I	field lens	W	angle scale
K	mirror on gimbal mount	X	interferometer, rotatable about a vertical axis through entrance aperture
L	second spot-wander controllers	Y	photomultiplier
M	50-50 beam splitter	Z	attenuator
N, R	polarizer		

Fig 5-4 Optical Layout for Velocity Simulator Measurements

interferometer to inspect each maximum in turn. For each velocity measurement, the bias was adjusted to make the reference pulse 50 percent of maximum. The intensity of the signal pulse was then observed. To cancel small errors in equalizing maxima and setting at the 50 percent point involved biasing alternately on both sides of a fringe and averaging the differences. The results are tabulated in Table 5-1 for 11, 12, 13 October 1967.

Serious anomalies remained. The instrument was examined in detail and it was observed that the theoretical angular insensitivity was being seriously impaired by two effects:

- The optical surfaces are flat to only $\lambda/20$. An analysis of the effects of errors in the surfaces (Appendix D) shows a probable variation in path differential over various parts of the aperture of greater than $\lambda/4$. In practice we observed somewhat less than this, based on visual estimate, but it was unquestionably worse than $\lambda/10$. In the second interferometer (see paragraph below) this would correspond to an error in apparent velocity of greater than 2,500 ft/sec and is more than enough to account for an unreasonable sensitivity to beam geometry.
- All surfaces other than mirrors and the beamsplitting surface are antireflection coated (0.25 percent). But even with this precaution the residual reflections present in the system, adding and subtracting coherently, were sufficient to produce noticeable auxiliary fringe patterns which moved rapidly as a function of angle. Better antireflection coatings (about 0.1 percent) should be used.

Careful beam alignment for each datum point was undertaken for the run of 14 October 1967. This minimized the two effects of above. Then this interferometer (designated, No. 1) was modified by inverting the mirror with integral delay plate and inserting a pair of optically contacted crown glass etalon plates for the delay element. They were tilted to remove the reflections off their surfaces from the system. This removed the rapid angular dependence of the subsidiary fringe system, though extra fringes were still observed. Of course the first effect was somewhat worsened by this change. This modified interferometer is designated as No. 2.

Table 5-1
VELOCITY SIMULATOR DATA FOR FIRST INTERFEROMETER

Wheel Speed (cps)	Equiv Source Speed (ft/sec)	(Scale of 2) Relative Signal	Comments
111	777	1.13	10/11/67 - Taken by C. Gillard
150	1050	1.19	
212	1550	1.23	
238	1670	1.28	
263	1840	1.35	
282	1970	1.37	
318	2230	1.43	
126	882	1.10	10/12/67 - Taken by C. Gillard and J. Rapier
135	945	1.29	
148	1040	1.17	
161	1130	1.19	
182	1270	1.28	
186	1300	1.19	
205	1440	1.19	
240	1680	1.37	
248	1740	1.19	
270	1890	1.41	
302	2114	1.31	
46	322	1.05	10/13/67 - J. Rapier
71	497	1.08	
98	686	1.10	
136	952	1.25	
136	952	1.36	
182	1280	1.34	

Table 5-1 (Cont.)

Wheel Speed (cps)	Equiv Source Speed (ft/sec)	(Scale of 2) Relative Signal	Comments
102	714	1.10	10/14/67 - C. Gillard.
152	1060	1.15	Excessive angular sensitivity
193	1350	1.20	discovered. Special pre-
240	1680	1.25	cautions taken to reduce beam
260	1820	1.27	wandering. Note improved fit.

Figures 5-3, 5-4, and 5-5 illustrate the experimental setup used in the final data-taking of 6 and 7 November 1967. The common key to all three figures is found in Fig. 5-3. Earlier data are found in Table 5-1; the data of 6 and 7 Nov. are tabulated in Table 5-2. Table 5-3 gives relevant parameters and useful conversion factors for use with both interferometers.

An analysis of deviations of the data in Table 5-2 indicates that interferometer No. 2 can measure apparent velocities to within ± 200 ft/sec or free-surface velocities to within ± 100 ft/sec over a range of 5000 ft/sec apparent-source velocity or 2,500 ft/sec free-surface velocity. There is no reason to expect any loss of accuracy up 7,000 or 3,500 ft/sec, respectively, for source and free-surface velocities.

It was necessary in obtaining the data of 6 and 7 November 1967 to maintain beam alignment to within $\pm 1/2$ deg, selecting a rotational position of the interferometer such that both beams fell within a region of flat angular response.

These data are presented in graphic form, together with the theoretical calibration curves, in Figs. 5-6 and 5-7. The curves were obtained from the relationship given by Eq. (3.10)

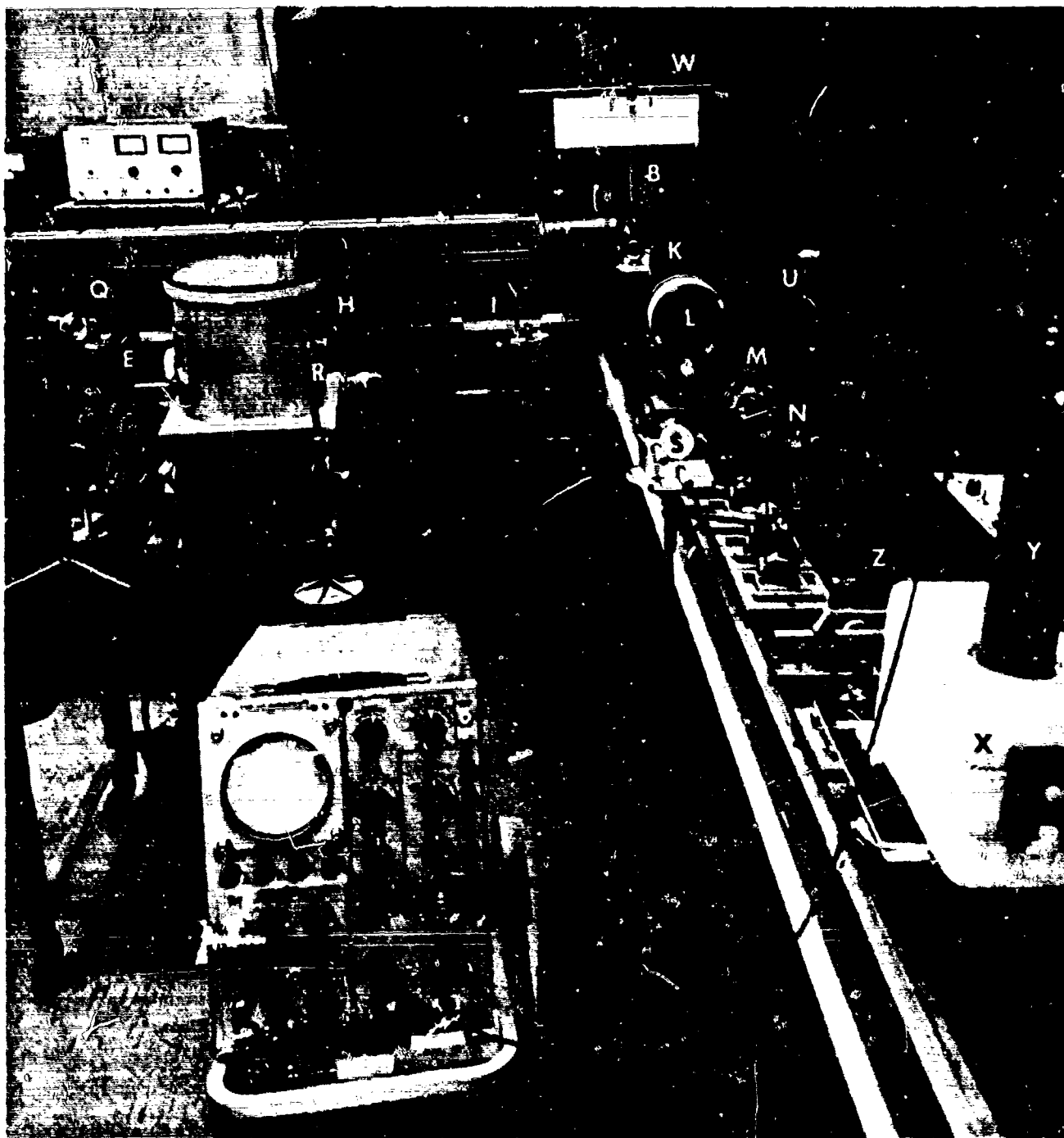


Fig. 5-5 Laboratory Velocity Calibration Setup
Using the Velocity Simulator

Table 5-2
VELOCITY SIMULATOR DATA FOR SECOND INTERFEROMETER

Wheel Speed (cps)	Equiv Source Speed (ft/sec)	Relative Signal (Scale of 2)	$\Delta\theta$ [Signal-] [Theory]*	$\Delta\theta^2$ (10^{-4})	Comments
270	1890	1.41	.00	0	11/6/67
271	1900	1.40	-.01	1	Gillard
271	1900	1.41	.00	0	
354	2280	1.56	.08	64	
7.5	52	1.05	.04	16	11/7/67
7.7	54	1.06	.05	25	Rapier
7.7	54	1.08	.07	49	
7.8	55	1.01	.00	0	
7.8	55	1.02	.01	1	
42.6	258	1.11	.05	25	
47.0	329	1.08	.01	1	
100	700	1.13	-.02	4	
102	714	1.20	.04	16	
102	714	1.13	-.03	9	
156	1090	1.24	.00	0	
156	1090	1.22	-.02	4	
232	1620	1.35	.00	0	
267	1870	1.32	-.08	64	
357	2500	1.51	-.02	4	
357	2500	1.50	-.03	9	

$\sigma_\theta = 0.038$ rad

$\sigma_{vel} = 200$ ft/sec effective source velocity

$\sigma_{vel} = 100$ ft/sec free surface velocity, for a reflector at near-normal incidence

* See Fig. 5-7

Table 5-3
RELEVANT PARAMETERS OF INTERFEROMETERS NO. 1 AND NO. 2

No. 1: Delay plate thickness: 0.93 cm
 Delay plate refractive index: 1.4585 (fused silica)
 Path differential, ΔL : 1.43 cm
 Change in apparent source velocity for 180° phase shift: 20,600 ft/sec

Intercomparison of phase shifts, wheel rotation rate, apparent and free-surface velocities.

	Phase Shift (deg)	Phase Shift (rad)	Wheel Speed (rev/sec)	Apparent Source Vel (ft/sec)	Free-surface Velocity (ft/sec)
1 degree phase shift =	1	0.0174	16.3	114	57
1 radian phase shift =	57.3	1	935	6540	3270
1 rev/sec wheel speed =	6.13 (10^{-2})	1.07 (10^{-3})	1	7.0	3.5
1 ft/sec apparent source velocity =	8.77 (10^{-3})	1.53 (10^{-4})	0.143	1	0.5
1/ft/sec free-surface velocity =	1.75 (10^{-2})	3.06 (10^{-4})	0.286	2	1

Table 5-3 (Cont.)

No. 2: Delay plate thickness: 1.21 cm
 Delay plate refractive index: 1.52 (crown glass)
 Path length differential, ΔL : 2.07 cm
 Change in apparent source velocity for 180° phase shift: 14,200 ft/sec

Intercomparison of phase shifts, wheel rotation rate, apparent and free-surface velocities.

	Phase Shift (Deg)	Phase Shift (Rad)	Wheel Speed (rev/sec)	Apparent Source Vel. (ft/sec)	Free-Surface Velocity (ft/sec)
1 degree phase shift =	1	0.0174	11.3	78.9	39.5
1 radian phase shift =	57.3	1	647	4520	2260
1 rev/sec wheel speed =	8.87 (10^{-2})	1.55 (10^{-3})	1	7.0	3.5
1 ft/sec apparent source velocity =	1.27 (10^{-2})	2.21 (10^{-4})	0.143	1	0.5
1 ft/sec free-surface velocity =	2.53 (10^{-2})	4.42 (10^{-4})	0.286	2	1

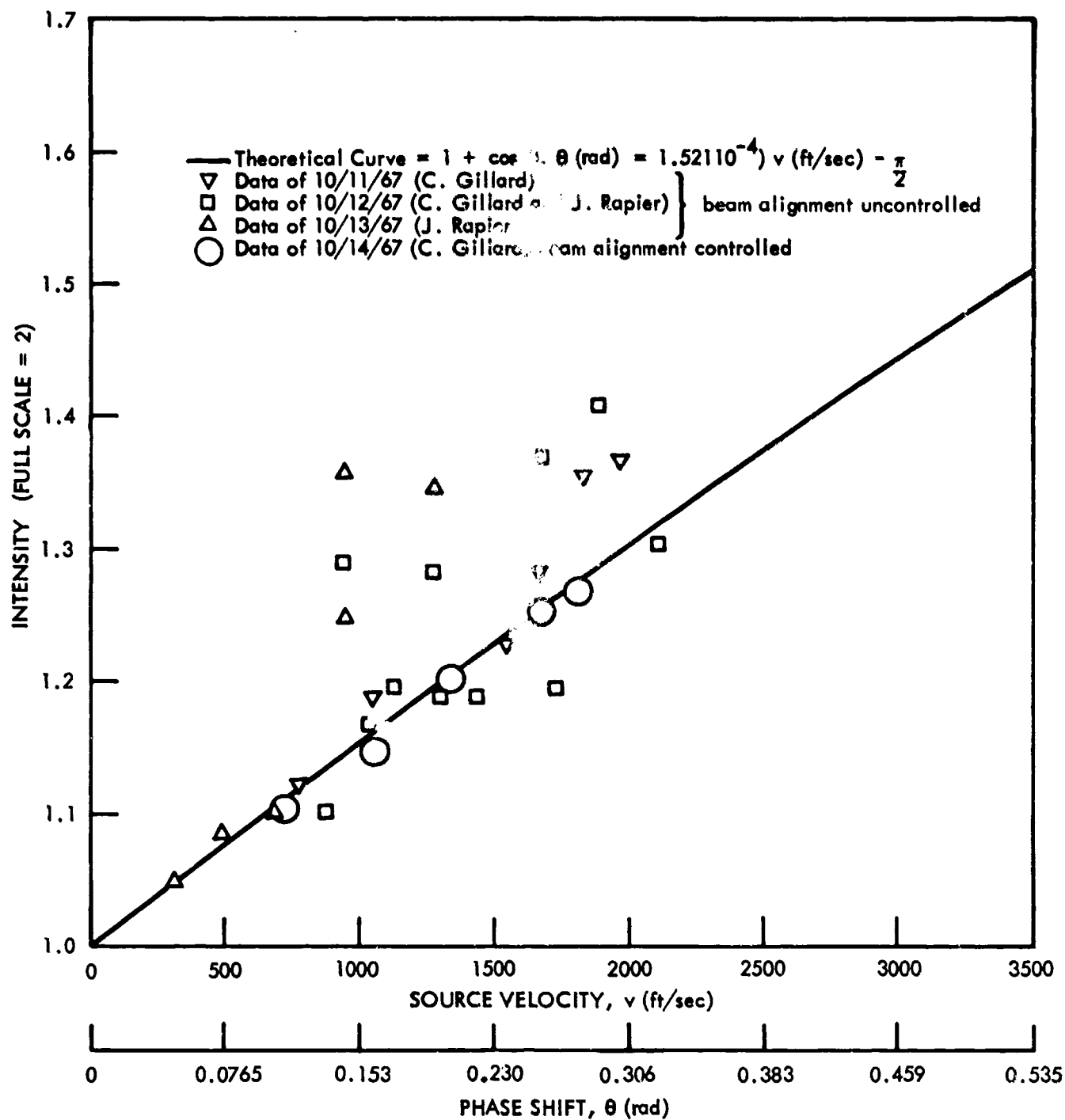


Fig. 5-6 Experimental Data and Theoretical Curve for Response of First Interferometer to Source Velocity

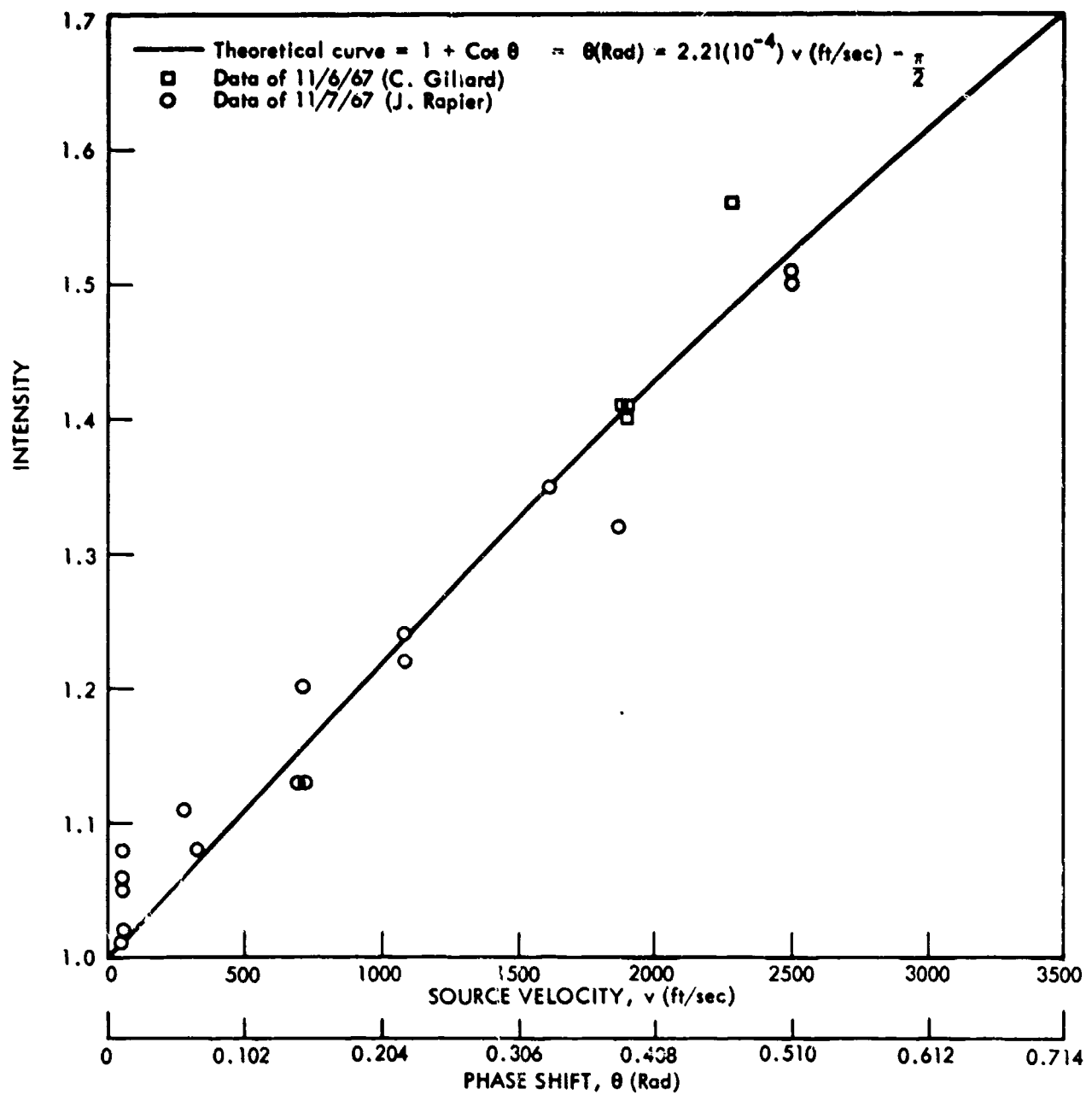


Fig. 5-7 Experimental Data and Theoretical Curve for Response of Second Interferometer to Source Velocity

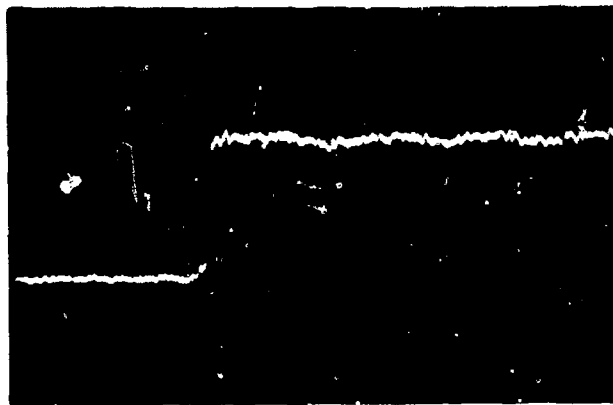
$$I = \frac{I_0}{2} \left[1 + \cos \left(\frac{2\pi \Delta L}{c} \nu_0 + \varphi \right) \right] \quad (3.10)$$

where I_0 is the maximum intensity of light output from the interferometer, I is the resultant intensity on recombining, ΔL is the total differential path length introduced in the delay leg, ν_D is the doppler shift in frequency of the incident light, and φ is a phase factor introduced by the bias. To plot the curve, the phase factor was set to -90 deg and I_0 to 2 and the value of I as a function of equivalent light source velocity was plotted.

5.3 EXPERIMENTAL WORK IN SHOCK FACILITY

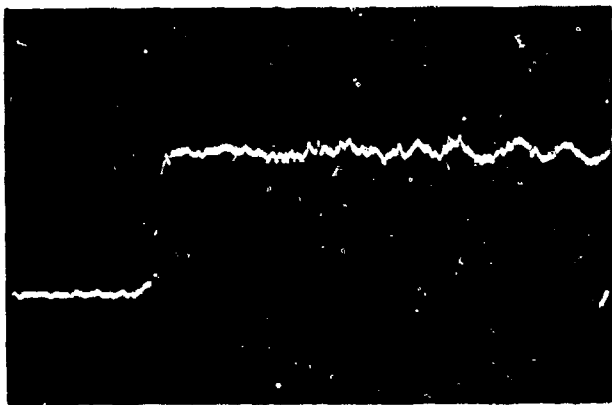
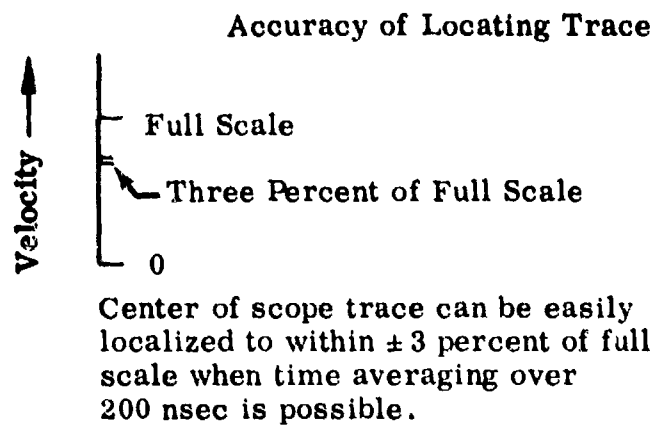
An experimental setup as shown in Fig. 5-8 was assembled. The laser beam was focused to a point to pass through a small aperture in mirror B, then was refocused by lens L to allow for deviation in angle of sample G in flight. The new focus was at the aperture of the catcher, H, upon exit. The beam spot on the sample was imaged by lenses and mirrors D, L, B, M, N, O onto the entrance aperture to the interferometer with a magnification of three. This reduces angular variations by a factor three and simultaneously prevents the beam from leaving the entrance aperture as long as it passes through the optical system. The optical system allowed a maximum angular variation in the input beam to the interferometer of approximately 1/2 deg in any direction before vignetting removed the beam from the system. Microscope slide R and photomultiplier S were used to monitor the amount of light traversing the system, to determine if the ratio amplifier had sufficient input to function properly when recording data. The outputs of the ratio amplifier and of the monitor were fed to Hewlett-Packard 175A oscilloscopes, with camera attachments. The resulting data are shown in Table 5-4 and Figs. 5-9(a) through 5-9(i).

Specimens examined for free-surface velocity due to shock were 0.25-in. 6061-T65 aluminum, ground flat to 0.002-in. on both sides, then polished to a mirror finish on one side for reflecting the laser beam. Each sample was struck by a 1/8-in. flyer plate of the same material ground to similar tolerance and mounted on a light, hollow piston, such that in the first few microseconds only the flyer plate is seen by the

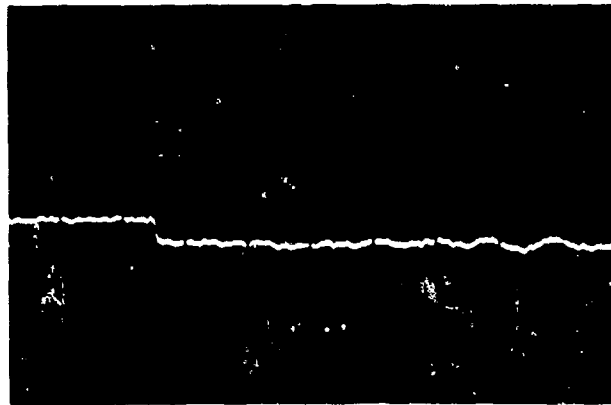


Time →

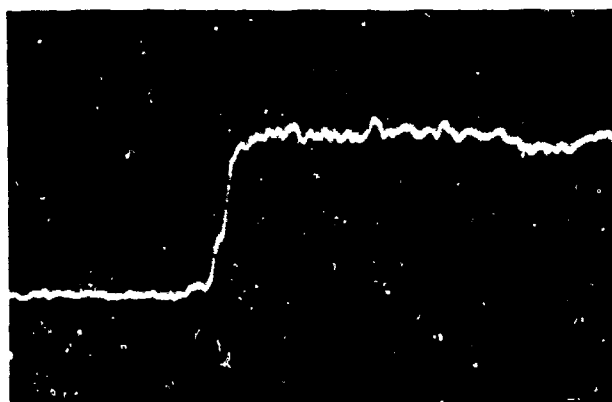
(a)



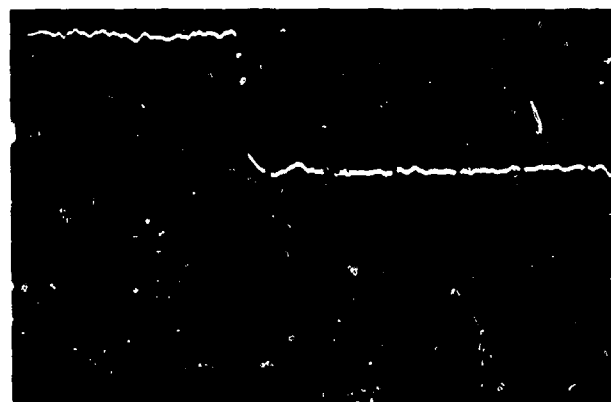
(b)



(b')

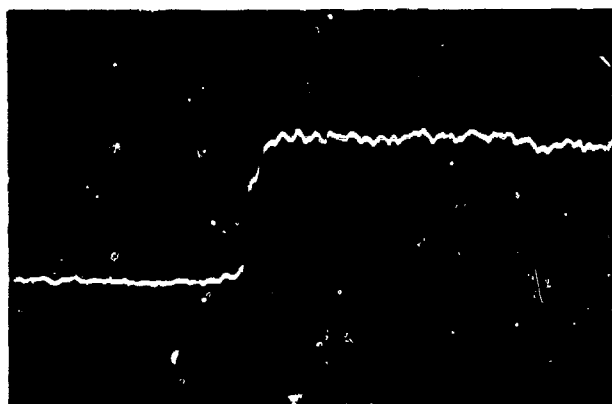


(c)

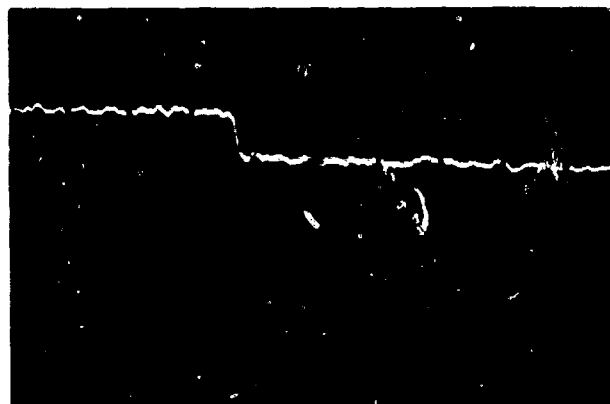


(c')

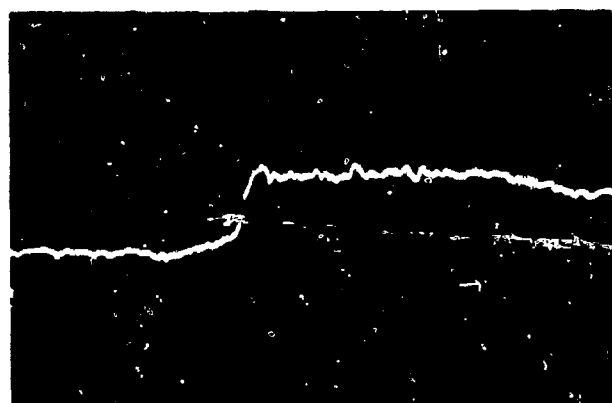
Fig. 5-9 Laser Velocimeter Free-Surface Velocity Traces of Shock-Loaded Aluminum



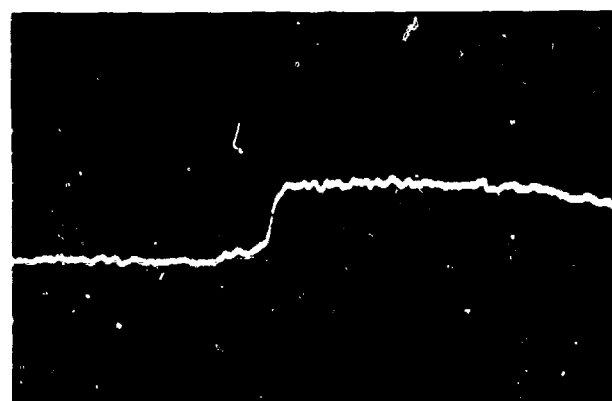
(d)



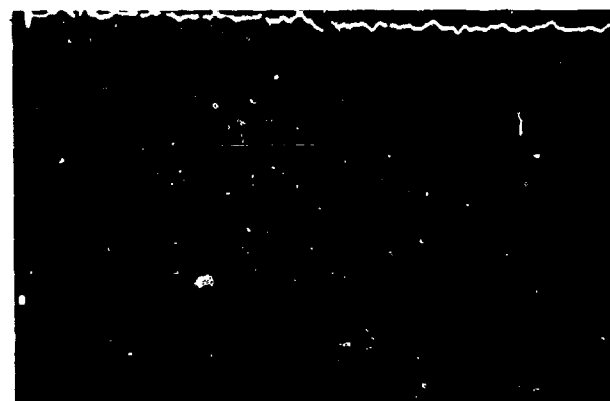
(d')



(e)

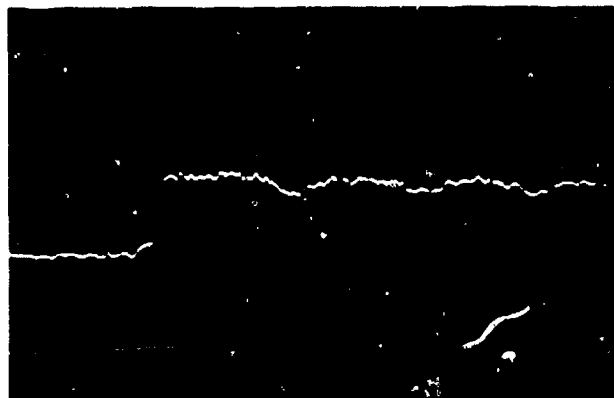


(f)

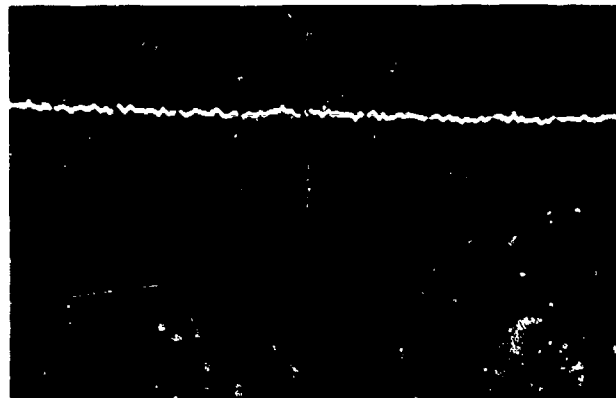


(f')

Fig. 5-9 (Cont.)



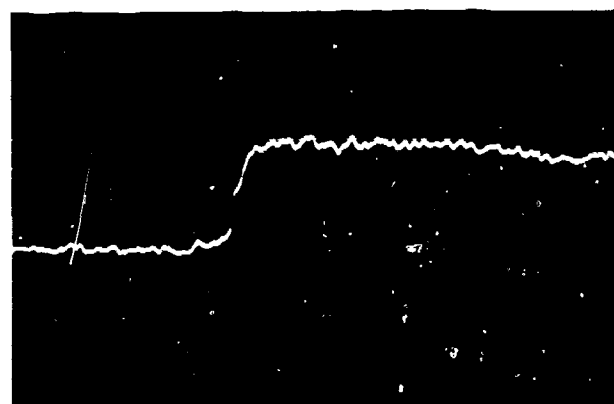
(g)



(g')



(h)



(i)

Fig. 5-9 (Cont.)

Table 5-4
VELOCIMETER DATA FROM LMSC SHOCK FACILITY

Figure	Projectile Velocity (ft/sec)	Time Scale, x axis (μsec/div)	Impact Time (μsec)	Time Scale, y axis (mv/div)	Signal Maximum (mv)	Precursor Surf. Vel. (ft/sec)	Plastic Surf. Vel. (ft/sec)	Baseline (msec)	Free Oscillations		Monitor Light Loss (%)	Comments
									Recorded	Amplitude		
5-9(a)	3,040	0.5	0.65	50	300	-	2,190	<50	1 μsec 3 cycles	100 ft/sec Neg pulses	No monitor	Oscillation is probably reflection of plastic wave (for all shots).
5-9(b)	3,016	0.5	0.15	50	300	990	2,250	~100	~1 μsec one cycle then 1 μsec, aperiodic then	~100 Neg pulses	40	Recovered sample showed small (originally 1/8-in. thick) had again split, into two ~1/16-in. layers. Slow rise not understood.
5-9(b')		0.5	0.15	10					0.5 μsec 4 cycles	400 slow wave		
5-9(c)	3,020	0.2	-0.38	50	300	990	2,560	~80			60	Disagrees with others. Note that this shot suffered from worst light loss on impact. Slow rise not understood.
5-9(c')		0.2	-0.38	10					1 One cycle only obs.	100 Neg pulses		
5-9(d)	3,019	0.2	-0.38	50	300	1,570	2,300	50	1 One cycle	100 Neg pulses	25	
5-9(d')		0.2	-0.38	10								
5-9(e)	1,514	0.2	-0.38	50	300	1,060	1,220	40	1 One cycle	250 Neg pulse	No monitor	Note larger amplitude of oscillation in lower velocity shot, this showed consistently.
5-9(f)	1,525	0.2	-0.27	50	300	1,060	1,220	40	1 One cycle	250 Neg pulse	3	
5-9(f')		0.2	-0.27	10								
5-9(g)	1,540	0.5	0.15	50	300	-	1,240	<50	1 3 cycle	250 Neg pulses	0	
5-9(g')		0.5	0.15	10								
5-9(h)	800	0.5	-0.27	50	300	-		~200	2 2 cycles	~250 Square wave	No monitor	Below spill threshold. Entire plate oscillated in flight. Slow rise not understood.
5-9(i)	2,235	0.2	-0.38	50	300	920	1,620	60	None observed	None observed	No monitor	Sample spalled normally. Failure to observe oscillation as not understood.

central part of the sample. Impact velocities ranged from 800 to 3,000 ft/sec, with measured free-surface velocities averaging 77.4 percent of the impact velocity. Estimated velocimeter system error based on Doppler wheel measurements is ± 100 ft/sec, and observed scatter in the gas gun data and the appearance of the traces [except for Fig. 5-9(c) where light loss was severe] suggest that this estimate is valid for slowly changing velocities where one can average over a time exceeding one or two tenths of a microsecond. Quantum noise in the phototubes degrades accuracy on rapidly changing velocities (see Fig. 5-9).

A shot run before the optical system was optimized demonstrated a rise time in the response to some beam variation of ≤ 20 nsec. Thus, despite the slower rise times cited in Table 5-4, it is known that the response of the electronics allows a time resolution of that order.

The low free-surface velocities measured with the laser velocimeter cannot be explained by the shock physics group with whom we worked (a free-surface velocity equal to the impact velocity is to be expected), but are seemingly borne out by work underway in the LMSC Research Facility, Palo Alto.* In a private communication with the LMSC Research Facility team, measurements performed with a streak camera on the free-surface velocity of aluminum struck by aluminum were disclosed. Their alloy was 6061-T6. The flyer was 1/4-in. thick and the sample 1/8-in. thick. They reported to us the results of two shots with impact velocities of 590 and 545 ft/sec. Measured free-surface velocities were 478 and 397 ft/sec (± 5 percent). This is 81 percent and 67 percent, respectively, of the impact velocity. The apparatus was checked by measuring a piston surface in free flight with the streak camera. This result was within 3 percent of the electronically measured velocity, thus removing the likelihood of a serious systematic error in the system. We plan to do a similar test with our apparatus, but lacked time to do so as of this writing.

The columns of Table 5-4 are interpreted as follows:

- Projectile velocity – velocity of flyer plate immediately before impact, measured electronically by timer

*Part of this discrepancy has been resolved and the instrument was tested on a free-flying piston (see Section 7).

- Time scale — time elapsed per division on the X-axis of the figures, measured left to right
- Impact time — computed time of impact of flyer plate on rear of sample plate, based on known delay times in trigger and signal circuits, referred to the first graduation on the figures (far right)
- Signal scale — mv/div scale setting on vertical amplifier of oscilloscope
- Signal maximum — difference between scale reading for extinction and maximum transmission bias settings on the interferometer
- Precursor surface velocity — velocity of free surface after arrival of elastic wave precursor through sample
- Surface velocity — velocity of free surface after arrival of plastic wave at front of sample
- Rise time — time elapsed between beginning of rise from precursor to plastic velocity and attainment of peak value (smoothed curve, neglecting noise)
- Free oscillations — data on oscillations in front spalled portion or entire plate, whichever is relevant, as it travels in free flight following impact
- Monitor light loss — percentage of initial return beam lost as the free surface begins to move and is either deflected, causing some vignetting, or its reflectivity reduced by an orange-peel effect that has been observed on recovered samples, or some other unknown cause. If this loss is less than 50 percent, the ratio amplifier can be assumed to give a trustworthy reading of the phase difference in the interferometer
- Comments — any other relevant information

In Fig. 5-9 is a calibration curve for the interferometer. Setting full scale (maximum transmission) of the interferometer at 2, the intensity reading is a function of phase shift as follows [see Eq. (3.8)] :

$$I = 1 + \cos (\theta - 90^\circ)$$

where θ is the angular phase shift in the delay leg from the position of 50 percent bias ($I = 1$). Relating phase angle to free surface velocity as in Table 5-4, second half, the calibration curve is obtained for output versus velocity, relative to 50 percent bias.

In practice, we start with a bias figure below 50 percent for the zero point and try to end up with a free-surface velocity trace equidistant from and above the midpoint (50 percent). The velocity readings are taken by subtracting the initial reading from the final one using Fig. 5-10. For example, assume the initial bias setting was 25 percent (0.5 on the graph), and the final reading for the plastic wave was 71 percent of maximum (1.42 on the graph). The corresponding velocities are, respectively, -1,180 and +980 ft/sec. The resultant velocity reading is thus 2160 ft/sec.

5.4 CALIBRATION MEASUREMENTS IN SHOCK FACILITY

Efforts were made to resolve the discrepancy between Columns 2 and 7 (shown in Table 5-4). These were done on in-house funding and have been included for informational purposes.

Special fliers were prepared which contained a simple form of retroreflector. This is shown in Fig. 5-11. The target was replaced by a Lucite window and the laser beam was directed down the length of the gas gun to the retroreflector. When the special fliers were fired, the velocity was measured down the length of the gun until the window was destroyed. The measurement of flier velocity by the contact pins of the gas gun took place just before window destruction and provides one reliable calibration point on each velocity-time record.

The duration of the observation was in the range of milliseconds rather than microseconds and the records were taken with a fast galvanometer-type recorder. Two good records are shown in Fig. 5-12. They show less contrast than those of Fig. 5-9 and are visually less satisfactory because of the type of recorder used. The comparison between velocimeter measurements and those of the gas gun instrumentation (time-of-flight) are shown in Table 5-5. Both velocimeter records yield low values of maximum

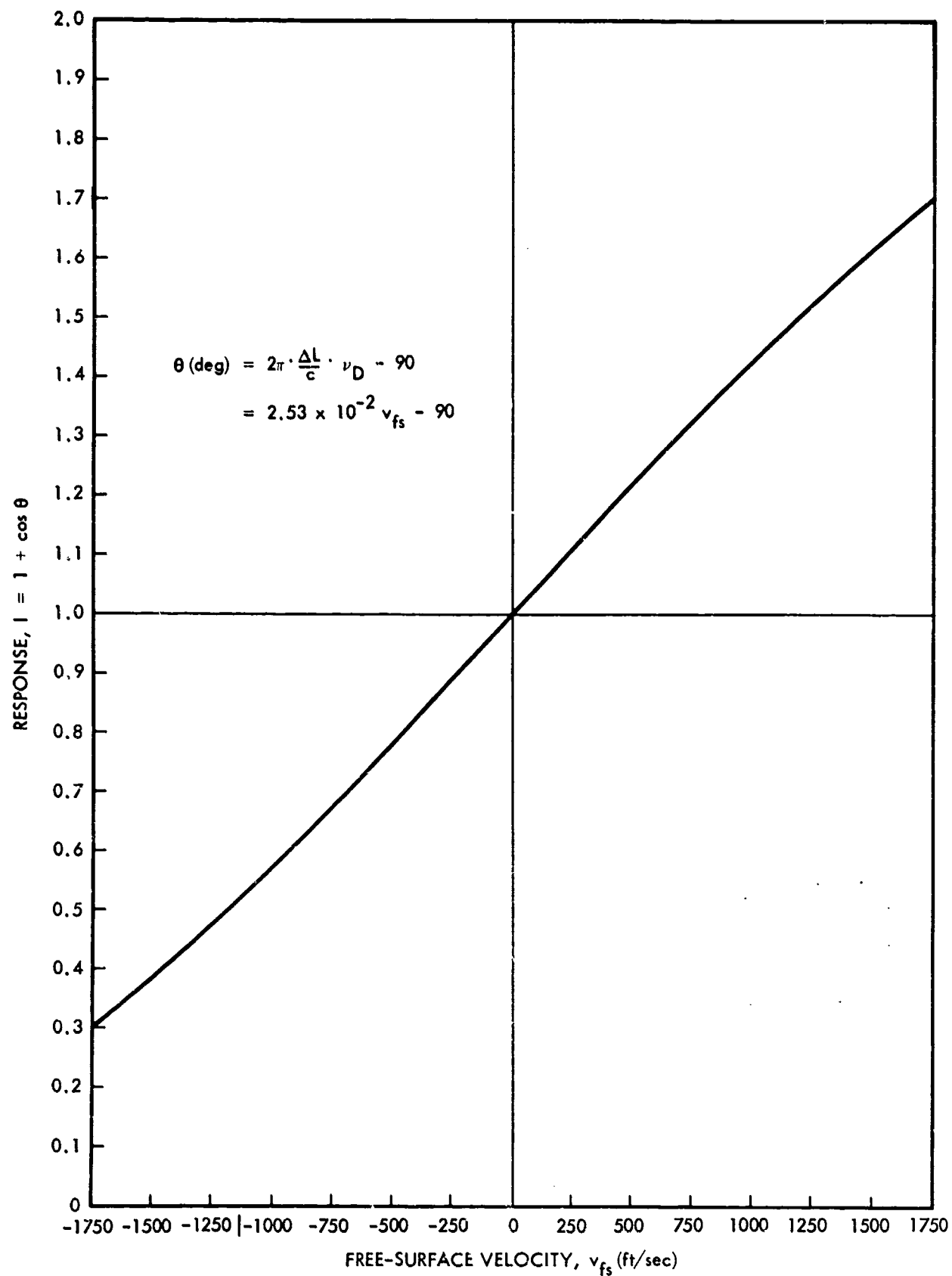


Fig. 5-10 Response vs. Free-Surface Velocity

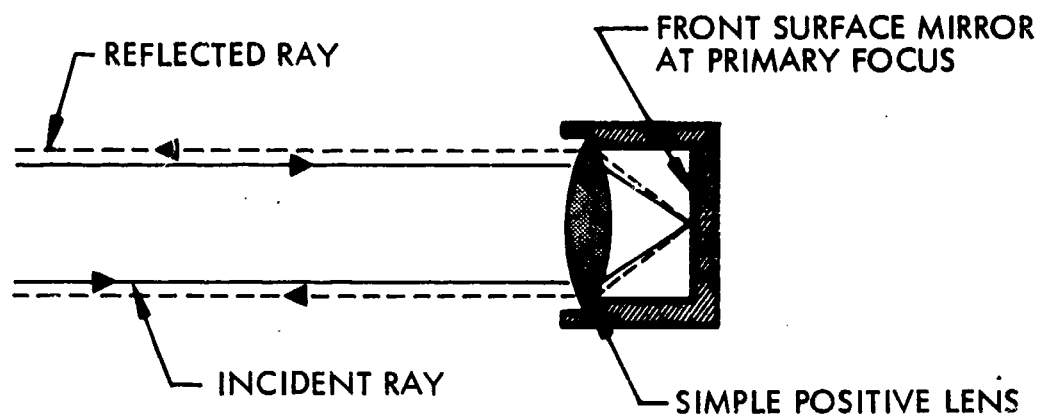
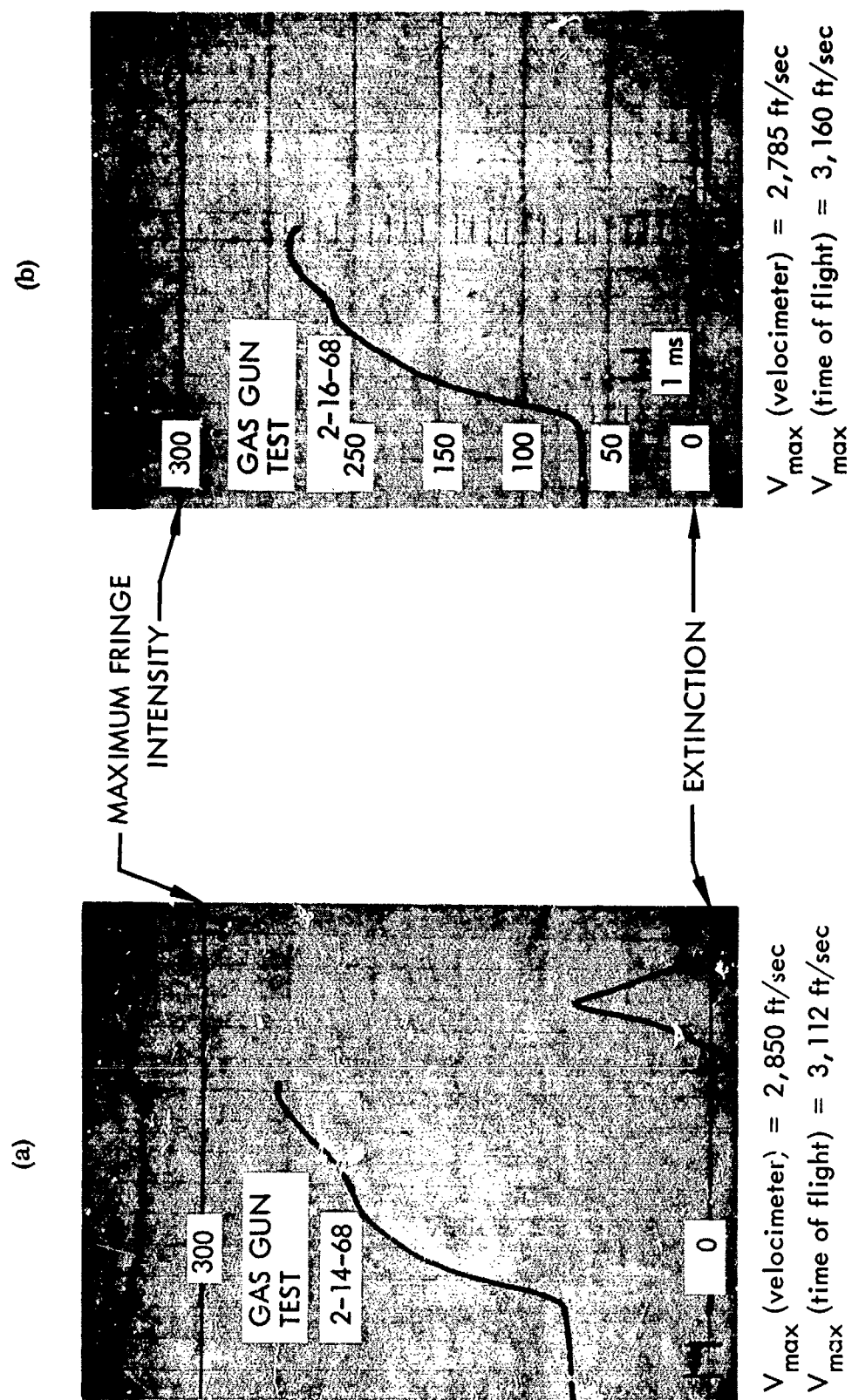


Fig. 5-11 Principle of Operation of Cat's Eye Retroreflector

velocity compared to the time of flight values. The relative discrepancies are 8.4 percent and 11.8 percent, respectively.

In subsection 4.3 it was shown that the character of the ratio amplifier was responsible for a bias in its measured output voltage and a resulting calibration error. The results of Table 5-5 were not corrected for this calibration error. The reason is that a complete correction requires a detailed record of the absolute output voltages of the ratio amplifier and these records were not taken. However, it was pointed out in subsection 4.3 that an average 10 percent slope correction was required when the reference photocurrent I_R remained fixed. The records of Fig. 5-12 were taken with essentially constant I_R because of the use of the retroreflector on the flar target.



Note: Markers show interference maximum and minimum corresponding to a calculated Doppler velocity excursion of 7,100 ft/sec.

Fig. 5-12 Velocimeter Flight Records of Special Pistons (Fliers) Down Gas-Gun Barrel

Table 5-5

VELOCIMETER SPECIAL FLYER DATA

Figure No.	Projectile Maximum Velocity (ft/sec)	Time Scale X-Axis (ms/dev)	Velocimeter Maximum Velocity (ft/sec)	Relative Discrepancy (%)
12a	3112	1	2850	- 8.4
12b	3160	1	2785	- 11.8

Applying this approximate correction we can correct the relative discrepancies of the preceeding paragraph to - 1.6 percent and 1.8 percent, respectively. Despite the approximate nature of the correction, these discrepancies approach the 1 percent velocity resolution which was a design goal for this program.

Several final comments are appropriate. The portions of the velocity record for which qualitative or semi-quantitative predictions can be made are found to be in satisfactory agreement with these predictions. In the initial portion of flight, and assuming the driving gas to expand adiabatically, the dynamic equation for the flier is approximately

$$\ddot{x} = \frac{\text{Constant}}{(V_0 + Ax)^\gamma} \quad (5.4)$$

where x is displacement down the gun barrel, V_0 is the fixed volume prior to firing, A is the cross-section to gas pressure of the flier, γ is the ratio of specific heats and the constant lumps flier mass, cross-section, and gas parameters. The significance is that when Ax is small relative to V_0 , the acceleration, \ddot{x} , is constant corresponding to a constant initial slope on velocity-time records. If a and b in Fig. 5-12 are examined, it will be seen that the initial portions of each record (after the onset of acceleration) have an essentially constant slope. When Ax becomes comparable to V_0 , Eq. (5-4) predicts a reduction in slope and this is the qualitative character of the referenced record curves. At the terminal end, the flier encounters a short "choke" region of the gas gun barrel which should produce a slight deceleration. This is seen as the short negative slope region at the end of each record curve.

In summary, for these measurements in which behavior predictions can be made, the observations agree well with predictions. The one velocity reference point on each record agrees with the corrected absolute velocimeter measurements to within ± 2 per cent. It is hard to avoid the conclusion that the laser velocimeter measured the velocity-time histories with accuracy consistent with its current state of development.

Section 6

CONCLUSIONS AND RECOMMENDATIONS

It is evident from the reported investigations that laser velocimeter systems designed along the lines of the system described in this report will provide a practical, convenient, and efficient way to measure the free-surface velocity history of a shock-loaded, solid material. Although hardware implementation of our investigations were limited to breadboard developments, results from our measurements, both in the laboratory using the velocity simulator and in the LMSC Shock Facility using a 2.5-in. gas gun, indicate that:

- Although there are calibration discrepancies which are still unresolved, the velocity resolution relative to full scale is in the range of 2 to 4 percent
- practical ways to implement the electronic system requirements of the AM-clipping function of the optical discriminator exist and time resolution of the associated electronics of less than 20 nsec appears to be feasible
- preliminary velocity-time measurements obtained with the breadboard velocimeter show what is interpreted as a precursor wave, suggest the possibility of elastic-plastic wave interaction, and give strong evidence that a significant amount of elastic wave energy remains with the spalled element after separation occurs. In several spalled elements distinct periodic vibrations have been observed that correlate well with what would be expected from a reverberating elastic wave in each of the free-flying, spalled elements.

Two phenomena which, as yet, have no explanation have been observed as a result of the shock tests using the LMSC gas gun:

- Five of the nine gas-gun firings indicate an anomaly in the rapid velocity jump. The effect is indicated in Figs. 5-9(b), 5-9(c), 5-9(d), 5-9(e), possibly 5-9(f), and 5-9(i), where the oscilloscope traces distinctly show that the velocity did not increase uniformly, but reached a plateau (indicating constant velocity) that

appears to be some 20 nsec in duration. It is believed that this plateau represents the elastic precursor and that it should have built up to a terminal maximum velocity of approximately 2,800 ft/sec. Yet all of the plateau velocities except one were approximately 1,200 ft/sec, the exception being approximately 2,000 ft/sec. As a possible explanation for the discrepancy, it is reasonable to suppose that the elastic wave, due to the small sample thickness, did not have an opportunity to build up to terminal velocity. We do not know whether the discrepancy was real or in our instrumentation. It is difficult to attribute the effect to noise, however.

- A discrepancy exists between flier velocity, as determined with the LMSC Shock Facility instrumentation, and free-surface terminal velocity during the period 0 to 5 μ sec after impact. In all cases the measured free-surface velocity was low, with the discrepancy being of the order of 20 to 25 percent.* In view of the good agreement between theoretical and experimental results using the Doppler wheel, it is difficult to see how our instrumentation could be in error by this amount.

These anomalies will have to remain a mystery until further investigations can be conducted.

A number of technical developments and refinements are recommended that, if implemented, would increase the accuracy of the laser velocimeter and make its deployment as an operational instrument simpler and more efficient.

- Optics. Better optical elements are needed to widen the acceptance angle of the differential interferometer and to reduce the spatial interference overlying the main interference pattern due to residual multiple reflections from the many air-dielectric interfaces in the system. Optical flats that are flat to within $\lambda/100$ or possibly $\lambda/200$ to both transmitted and reflected waves should be employed. V-coated antireflection surfaces with reflectivities of 0.1 percent or better should be specified.

*Approximately 10 percent of the discrepancy is explained by the ratio amplifier behavior as noted in subsections 4.3 and 5.4.

- Thermal compensation. Practical operational requirements, judging from our experience using the LMSC gas gun to obtain shock data, dictate a need for more thermal stability than was provided by our breadboard optical discriminator. Fabricating a differential interferometer from thermally stable materials such as invar and fused quartz would probably provide the needed stability. The possibility of employing an electronically controlled thermal enclosure for the differential interferometer might also be considered.
- System noise. Noise on the oscilloscope traces [Figs. 5-9(a) to 5-9(i)] may be reduced by employing photodetectors with more efficient photo-surfaces, by increasing the laser power, or both. The possibility of using vacuum photodiodes* or solid-state photodiodes for photodetection should be given serious consideration. If both the photodetector efficiency and the laser power are improved by employing an argon ion laser, it should be possible to obtain velocity measurements from diffuse surfaces. This would minimize, and possibly eliminate, beam deviation during the shock event; shock investigations using both nonspecular materials and curved surfaces might then be considered.
- Electronics. Experimental shock data using aluminum targets with free surfaces polished to a specular finish give clear evidence that an irreversible change in the optical property of the free surface occurs during the rapid velocity jump. This implies that the use of some form of ratio amplifier will be necessary as part of a practical laser velocimeter prototype. The breadboard ratio amplifier employed with our tests needs further development to reduce nonlinearities, increase dynamic range, increase common mode rejection, and, possibly, improve frequency response.

*Further increase in light input would tend to overload photomultipliers.

BLANK PAGE

Section 7

UNDERGROUND TEST FEASIBILITY

This addendum section examines the feasibility of using the LMSC Laser Velocimeter for underground testing of shock effects. The scope of the study is delineated in subsection 7.1; in 7.2 the character of the underground test environment is given insofar as it would affect fielding the laser velocimeter; the configuration options are discussed in 7.3; in subsection 7.4, the degree and nature of laser velocimeter redesign are considered in detail; and the conclusions and recommendations resulting from this study are presented in 7.5.

Following subsection 7.5, a comparison chart is presented for three laser velocimeter types. These types are the Sandia (Barker) instrument, the Los Alamos Scientific Laboratory instrument, and the one developed by Lockheed Missiles & Space Company. The direct comparison of the actual instruments was judged to be infeasible because of their widely differing parametric characters; consequently, the comparison is based on the capabilities of each instrument type, reduced as far as possible to a common denominator. Where this cannot be done, the particular conditions are cited in footnotes.

The general conclusions are that no problems other than those of good design exist for either a velocimeter which can be fielded or for the performance of an underground test experiment. The comparison charts present a group of striking advantages provided by the LMSC velocimeter.

7.1 INTRODUCTION

The purpose of this addendum is to examine the laser velocimeter system described in the preceding sections of the report and determine the feasibility of extending the present design to enable the instrument to operate, furnish accurate free surface velocity data, and survive in an underground test environment.

It has been suggested that the laser velocimeter offers several advantages in measuring free surface velocity histories of radiation-shocked samples. The only contact between the velocimeter and the sample is the laser beam. Samples may therefore be examined over any area with no concern for "loading." No electrical components need be subjected to the same environment as the sample and no components of the measuring system need be placed behind the sample.

An application suggested by the above characteristics for which the laser velocimeter is uniquely qualified is the measurement of free surface velocity of thin samples (transparent to radiation) and materials undergoing spall.

This addendum describes the probable physical environment to be encountered in underground tests and presents what are believed to be worst case calculations of the radiation environment. In the light of these environmental conditions, some possible experimental configurations will be suggested.

A major portion of the addendum considers the degree of redesign of the velocimeter system required for operation in an underground test environment and outlines a possible approach to this redesign. Each of the major elements of the system is examined separately, considering the following objective overall system specifications:

- Full-scale velocity of 100 m/sec and higher, with interchange of delay elements
- Free surface velocity resolution of 1 percent of the full-scale range employed
- Time resolution of the order of 10 nsec
- Insensitivity to changes in input angle or convergence of reflected beam
- Insensitivity to background input intensity changes of 10:1

To be practical for field tests, the instrument must also be capable of:

- Transmitting data to recording instruments several thousand feet away
- Being remotely controllable or automatically servocontrolled (personnel may be evacuated far in advance of the test)

- Being set up and operated by technician-grade personnel
- Operating throughout and surviving the nuclear detonation, if possible

The report is followed by conclusions and recommendations. The capability of the LMSC velocimeter to operate in the underground test is being reviewed, and recommendations for possible continued effort toward this end are made.

7.2 UNDERGROUND TEST ENVIRONMENT

7.2.1 Physical Environment During Setup

During the time in which the experiment is being set up and tested, there may be construction work, earth moving, sand blowing, concrete curing, and many other operations which will combine to create a hostile environment for a sensitive optical/electronic system. Heavy machinery may be moving about and earth moving operations may be in progress. This can result in considerable vibration. Large amounts of sand, cement dust, and other types of particles in suspension in the air would be deposited on or in the equipment. Temperatures can be expected to vary during these operations from nearly 60°F to as high as 100°F, according to LMSC personnel who have participated in these tests. The relative humidity may rise as high as 100 percent and supersaturation and condensation or mist can occur inside the tunnel.

7.2.2 Physical Environment During Operation

All subsystems are required to operate continuously from final calibration (with personnel in the alcove) until detonation or to be turned on and adjusted automatically before detonation without the chance for human intervention at the tunnel site.

The large fluctuations in physical environment described previously should have disappeared before evacuation, and operation of heavy machinery should have ceased. The only vibrations encountered during this period will be due to rotating machinery

necessary to the test (motor-generators, vacuum pumps, the air circulation system, cooling systems, etc.). The suspended particulate matter caused by construction work will have settled and the alcove will have reached an equilibrium temperature dependent upon the amount of heat generated by equipment, air circulation, and the earth thermal sink.

Humidity variations will be significantly diminished after the concrete setting and curing are effectively complete. Air circulating systems are shut off just before detonation; however, temperature and humidity should not change in that short time period.

7.2.3 Radiation Environment During Operation

No specific test has been chosen. The radiation environment conditions cited here are order-of-magnitude estimates, based on a yield of 10 KT at a distance of 400 ft with no shielding. This is being conceived to be worst-case estimate. Unclassified source material has been used to keep this report unclassified. (6, 7)* **

7.2.3.1 Gamma Radiation

An unshielded total gamma ray flux of somewhat less than 10^6 r, of an average energy near 0.9 Mev may be expected. Much of this radiation will appear as a short, intense pulse of an effective length of 2×10^{-7} sec and a peak intensity of 2×10^{11} r/sec. In terms of photon flux, this amounts to a peak value of 4×10^{20} photons/sq cm/sec at 400 ft.

*Assumed proportionality to yield in comparing data from (6) and (7) and drawing conclusions.

**Assumed inverse square law to get estimate.

7.2.3.2 Neutrons

Expected total flux for postulated conditions is about 3×10^{15} sq cm. Reference (7) suggests an upper limit as high as ten times this figure, or 3×10^{16} /sq cm.

7.2.3.3 Thermal Radiation

Total heat radiation would be 400 cal/sq cm. The temperature of the fireball will be of the order of magnitude 10^7 °K⁽⁶⁾ implying that most of the thermal radiation will be in the form of x-rays of 10 Kev, or 2.9 Å.

7.2.3.4 Electromagnetic Pulse

A rapidly varying electronic field may reach values of order 10^5 V/m, and magnetic field pulsations may reach 500 Oersted.

7.2.3.5 Prompt Shock

Absorbed radiation will set up shock waves in test sample and neighboring fixtures, occurring at about the time of data transmission (since the experiment is to examine this effect in a sample).

7.2.4 Physical Environment for Survival

This is the period of time following the experiment and preceding removal of surviving equipment. All power will have been shut off.

Reference (6) provides a formula for computing acceleration due to ground shock waves. Application to our cause suggests that accelerations as high as 40 g may be encountered. Lockheed personnel who have fielded equipment previously state that motions of several feet in amplitude are possible.

The tunnel is set up to minimize flying debris by various self-closing blast doors and collapsing structures. However, part of the time, according to cognizant Lockheed personnel, equipment not mounted in alcoves well isolated from the direct line-of-sight region will be destroyed by debris which comes through the closure mechanisms. Collapse of the tunnel and alcove may occur, necessitating digging to retrieve equipment. Depending on the particular situation, special protection for equipment may be required.

7.3 POSSIBLE CONFIGURATIONS FOR UNDERGROUND TESTS

In light of the environmental conditions described in section 7.2 above, three possible layouts for an underground test using the laser velocimeter are illustrated in Fig. 7-1. All three configurations show the velocimeter interferometer and its signal and control electronics and support equipment installed in an alcove to one side of the test chamber. The differences in the three proposed configurations are in the methods by which the laser illumination reaches the sample under test.

In Configuration 1, the laser output beam traverses exactly the same path as does the return beam from the sample to the interferometer. Optically and mechanically this is the simplest of the three configurations. The output laser beam traverses a maze through the alcove shielding, enters the test chamber through a single port, reflects off a transfer mirror directly behind the sample under test, then reflects from the free surface of the sample and returns off the transfer mirror through the optical train and into the interferometer. This system has one major disadvantage in that the transfer mirror in the test chamber is directly behind the sample under test. For samples that have significant shine-through, the transfer mirror would then be subjected to radiation effects (shock, heating, etc.).

The other two configurations proposed in Fig. 7-1 have the laser illumination of the sample traversing a different path than the return beam from the sample. In the second configuration, the laser is again in the same alcove as the velocimeter. The output beam to the sample traverses the maze slightly to one side of the return beam,

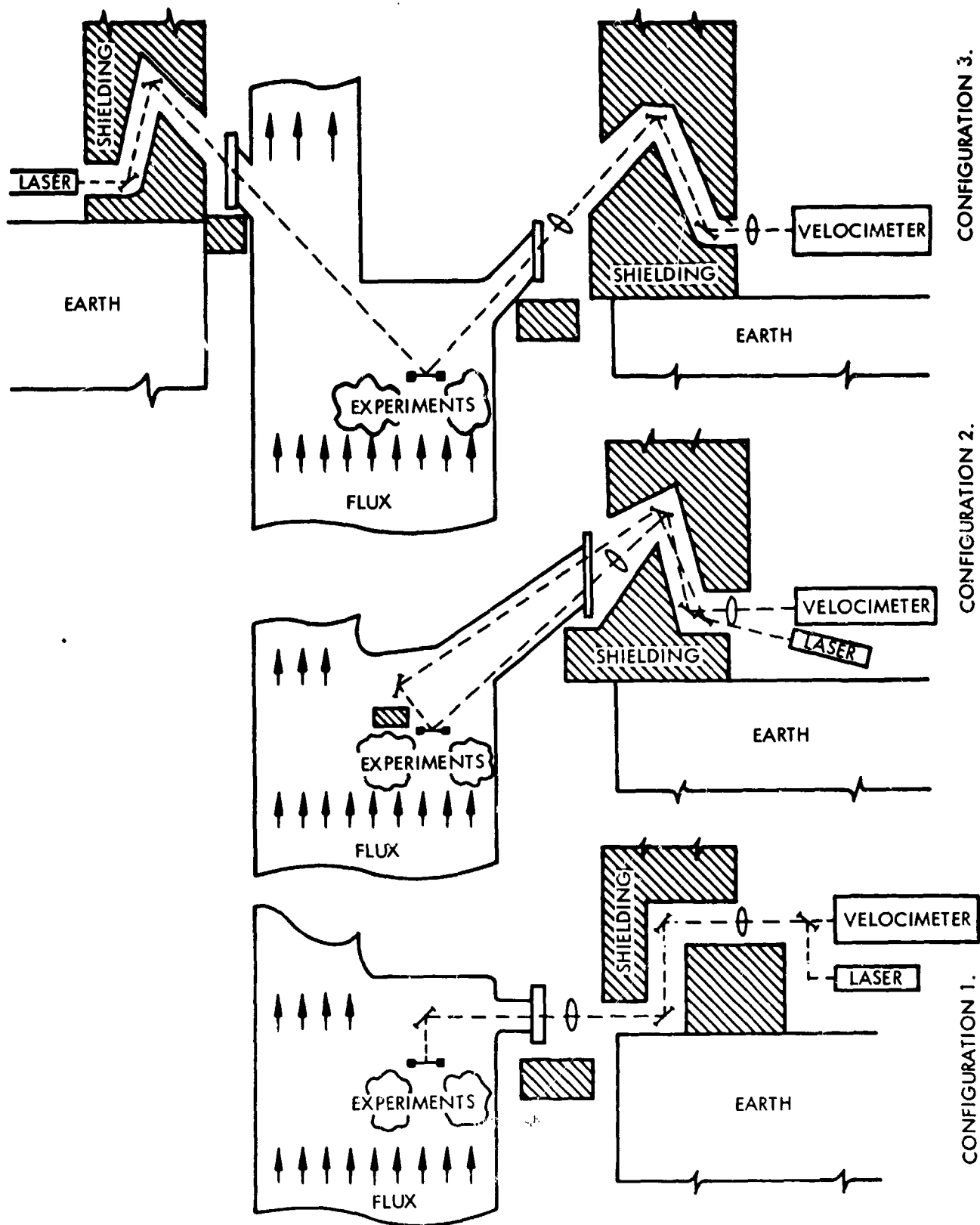


Fig. 7-1 Possible Velocimeter Test Configurations

reflects off a transfer mirror which may be shielded behind other experiments and some shielding of its own, then reflects off the sample at a slight angle and back through the transfer optical system into the interferometer. This configuration allows the transfer mirror to be shielded and will assure its not being significantly shocked or heated during the test. All of the transfer optical system can therefore be shielded from direct radiation and can be reasonably assured of not significantly degrading the signal or adding spurious signals to the return beam.

There is a possibility that the amount of shielding required for this transfer mirror may be awkward to install, even behind other experiments, and therefore Configuration 3 is suggested as an alternative. It is slightly more complicated to field, but it does not require any part of the system inside the test chamber except for the test sample itself. In Configuration 3, the laser and projection optics are in a separately shielded alcove in one side of the tunnel, the beam traverses a maze in the shielding for the laser alcove, enters the test chamber through a shielded window, reflects off the sample, then reflects out through a second shielded window through the shielded relay optics and maze into a second alcove that contains the velocimeter, its interferometer, the electronics etc.

For Configurations 1 and 2, the velocimeter system probably should be provided with a master mounting structure which would provide system orientation, shock and vibration isolation, a general sealed environment to protect against moisture and dust, electrical shielding and ground isolation, and some protection from debris and alcove collapse. Configuration 3 would require a second protective structure for the laser and transmitting optics. These structures should be anchored to rock bolts in the earth.

For the purposes of this discussion the sample is considered to be a flat, specularly reflecting metal disc, edge mounted in a foam ring. This system and these configurations are applicable to non-specular samples (diffuse reflector). This, however, adds some complication to the optical system and considerable laser power will be lost by any distance between the sample and the first focusing lens in the optical relay chain.

If a shielded lens can be mounted quite close to the diffuse reflector, a considerable fraction of laser power can be directed into the LMSC velocimeter, using its acceptance angle of several degrees to good advantage.

All of the relay optics and windows in the chain between the laser and interferometer should probably be constructed of fused quartz which needs only to be shielded to protect it from a level of radiation greater than 10^{17} N/sq cm or 10^8 rads. Coatings on the windows may be difficult because of the environmental conditions; however, the windows can be tilted and therefore should cause no significant losses. Multiple reflections which could cause degradation of visibility in the interferometer are thus eliminated. The relay lenses can be antireflection coated since they are easier to shield.

Radiation-hardened coatings are also available for the relay lenses and relay mirrors. A reasonable radiation shield can be installed in the front of the alcove at the side of the tunnel to guard the interferometer, photomultipliers, and other equipment installed in the alcove against scattered radiation from the test chamber and samples therein. Direct radiation from the detonation will obviously be shielded by considerable thickness of earth and is therefore expected to be of little significance. In individual system descriptions, further discussion will be provided on the problem of shielding of the elements of the velocimeter system which are particularly vulnerable to the radiation environment.

7.4 VELOCIMETER REDESIGN

Possible redesign of the three main subsystems of the velocimeter system is described in the following paragraphs. The interferometer optics will be considered in detail concerning quality, mounting, and coatings. The interferometer structure which supports these optics and which has to be extremely stable, adjustable, and controllable, will also be considered. The electronics for servoing the interferometer tilt and bias adjustments and controls will be discussed along with the electronics for the trigger and signal systems. A fourth section will consider the calibration and test simulation required for this system.

7.4.1 Interferometer Optics

Improvement in the quality of the interferometer optics and optical mounts over that of the present system must be considered in order to eliminate errors introduced into the system by motion of the input laser beam. Beam motion could be due to vibration- or radiation-induced prompt shock in any part of the optical relay system, bowing or tilt of the sample, or radiation-induced index changes in the relay optics.

7.4.1.1 Element Quality

Common intensity variations that enter the reference and signal photomultipliers will be removed by the ratio amplifier electronics. Any motion of the beam which changes output in one channel relative to the second, however, will cause an uncalibratable error in the output.

These errors could be caused by unequal vignetting in the two channels or a variation of path length in the interferometer for a beam motion within its normal angular acceptance. These variations in path length are caused by irregularities across the surfaces of optical elements.

The acceptance angle for the LMSC interferometer can be found from Eq. (3.14). Rewritten slightly it becomes:

$$\Delta L(\epsilon) = \Delta L(0) \left[1 + \left[\frac{1}{8n^2 a_1} \right] \sin^4 \epsilon \right]$$

To obtain the angle for a 1 percent path variation set $\Delta L(\epsilon) - \Delta L(0) = \lambda_0/400$ since the full scale variation is $\lambda_0/4$. From Appendix A we obtain

$$\Delta L(0) = \Delta \theta_{\max} \frac{\lambda_0}{2\pi} \frac{C}{2v_D}.$$

The angle variation which will cause a 1 percent error with a full-scale velocity of 100 m/sec and phase angle of $\pi/2$ is:

$$\sin^4 \epsilon \approx 8n_1^2 [\Delta L(\epsilon) - \Delta L(0)] \frac{4\pi u_{D(\max)}}{\lambda_0 C \Delta \theta_{(\max)}}$$

$$\epsilon \approx \pm 1^\circ$$

Therefore, for a full-scale velocity of approximately 100 m/sec, the interferometer would have an inaccuracy due to angular variations of less than 1 percent of full scale as long as the input angle varies no more than ± 1 deg. It is obvious that angular acceptance and accuracy for full-scale velocity; however, the foregoing were the design parameters chosen for this addendum.

Experience with the breadboard interferometer discussed in the preceding sections of this document has shown it incapable of using its full angular aperture. This is due to the surface irregularities of the optical elements. Appendix D shows the effect of surface irregularities of the various optical elements of the interferometer on the total path differential through it. The rms surface irregularities of the individual optical elements (shown in Appendix D) will be multiplied by a factor of approximately 5.3 when considering the entire interferometer, as the pencil beam wanders over the surface. Even with the best available quality optical flats (i.e., 1/200 wave), this still leads to an uncalibratable velocity error of approximately 10 percent; i.e., 1/200 multiplied by 5.3, or approximately 1/40 of a wave which is 10 percent of the full-scale velocity. The input beam to the interferometer may be expanded to flood the entire aperture and will produce an averaging effect rather than a single pencil effect. This averaging will decrease the absolute uncertainty in the interferometer but will lead to a secondary loss of fringe visibility in the output. Fortunately this fringe visibility loss will cause only a calibratable error in the output. The absolute minimum will be increased and the maximum will be decreased by a factor measurable at the time the instrument is calibrated. Second-order uncalibratable errors (velocity

uncertainties) will occur even in the filled aperture system due to a non-uniform intensity distribution across the input beam. The intensity non-uniformities will wander with the beam or as it changes convergence. The effect on non-uniformities over an increment of path-length variation is a velocity uncertainty which is proportional to the product of the intensity and path uncertainties. The product of uncertainties may lead to velocity uncertainties on the order of 1 percent. In this event, then, during calibration there are tradeoff options. The input angular acceptance of the interferometer may be limited to somewhat less than the ± 1 deg described previously or the interferometer aperture may be decreased to reduce uncalibratable errors caused by beam wander to less than 1 percent.

A second consideration concerning beam wander is in the aperturing of the reference and signal optical systems. In the flooded system, the limiting apertures of channels must be the same and the same distance apart. Otherwise, as the beam wanders, it will cause errors due to different portions of the beam arriving at the photomultipliers.

In the present system, anti-reflection coatings of 0.25 percent are used on all non-reflecting surfaces. Surfaces which are at normal incidence to the beam cause a significant amount of undesired reflection which in turn leads to a loss of fringe visibility. This fringe visibility loss will decrease the absolute magnitude of the intensity curve as described previously and will decrease the number of resolvable signal increments with any given laser power. All surfaces should be anti-reflection coated to the state-of-the-art extent which, at present, appears to be of the order of 0.1 percent.

7.4.1.2 Element Mounting

It follows from the previous discussion that the individual elements of the interferometer must be mounted with extreme care so as not to distort them and degrade their inherent optical quality. Simple strain calculations show that the individual elements may be mounted in any orientation without their weight causing a deformation of the optical surface sufficient to cause inaccuracies in the system. An optical flat, approximately 1 cm in thickness and 5 cm in diameter, made of fused quartz and supported by

a ring around its rim would distort somewhat less than 1/1000 of a wave due to its own weight. Clamping forces approximately twice the weight of the optical flats would cause no significant distortions. This sort of clamping force, however, would be insufficient to hold the optical flats under the heavy g-loads encountered as the result of ground shock from an underground burst. It is necessary to provide a secondary and stronger backup for the mounts very close to the optical flat, which, in normal operation, is not in contact with the optical flat. Typical mounts which could fill this requirement are illustrated in Fig. 7-2. They would include a plate of Invar (A) slightly thicker than the fused quartz disc (B). The Invar would have an opening slightly larger than the diameter of the optical element. Clamp rings (C), would be placed on the outside of the opening on either side of the optical element. The element, supported in the middle of this structure, would be potted into the aperture with a suitable density silicone rubber. The density of silicone rubber and the clearance between the structure and the optical element would be chosen to supply enough mounting force to hold the element in position and yet not stress the element during any temperature cycling of the mount.

Temperature gradients within the interferometer cannot be tolerated. A temperature gradient of $1/3^{\circ}\text{C}$ from one part of an optical flat to another can give rise to errors of the order of $\lambda_0/200$.

7.4.1.3 Extra Range

The interferometer discussed in this addendum has been chosen to have a full scale range of 100 m/sec and is therefore adaptable to higher ranges. This will necessitate compensating optical delay elements as long as 15 cm. Such delay elements may be fabricated from the same high-quality fused quartz as the other optical elements by using state-of-the-art techniques. Fused quartz has an extremely low physical expansion rate for a given change in temperature; however, the change of index of refraction with temperature is of the order of $9.5 \times 10^{-6}/^{\circ}\text{C}$. It will be necessary, therefore, to make up a thermally compensating mounting structure for the fused quartz optical delay element which, by motion of the entire element, compensates for the change in delay length with temperature. The delay length change, with temperature, is:

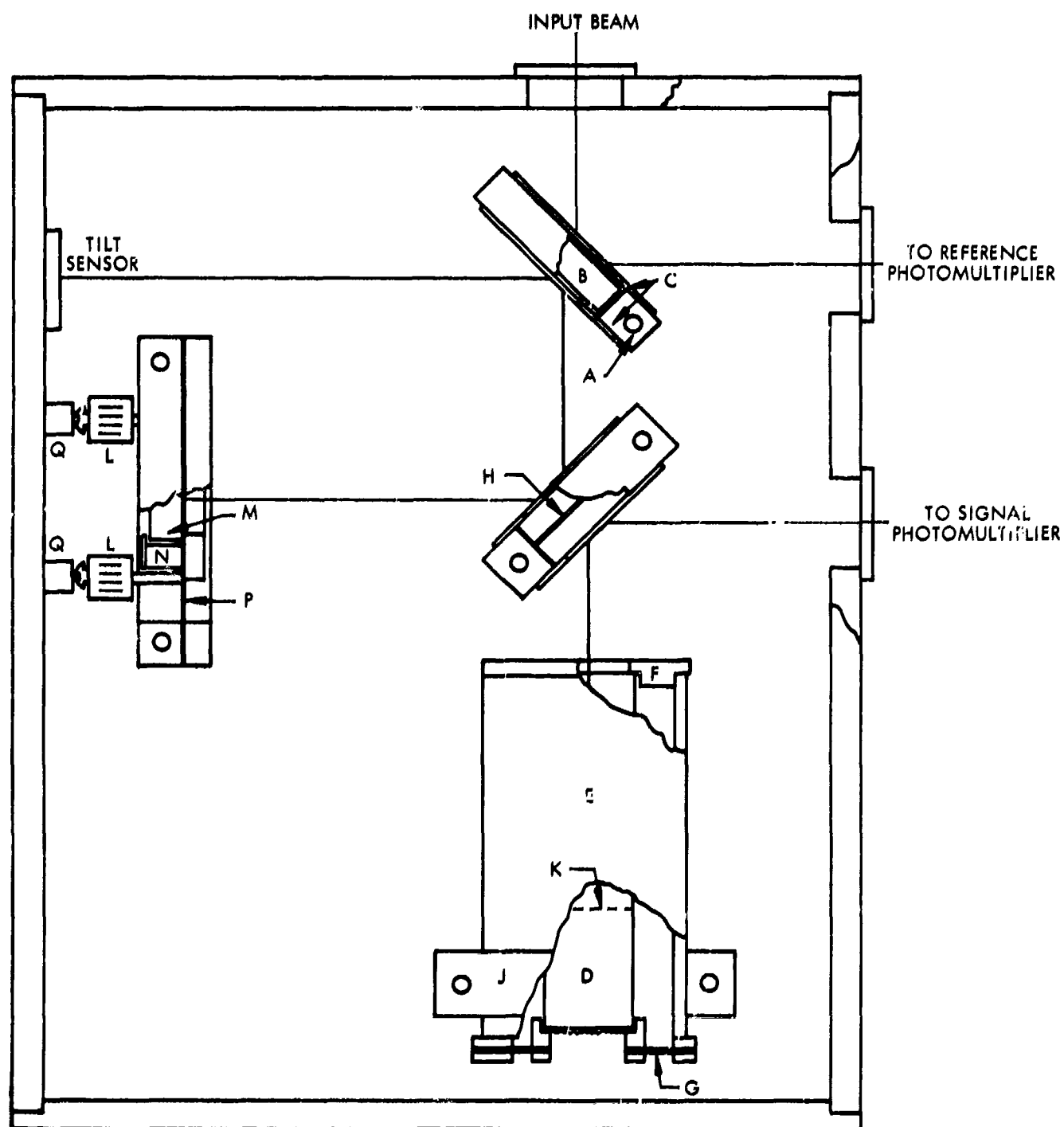


Fig. 7-2 Tentative Interferometer Concept

$$\frac{1}{\Delta L} \frac{\partial \Delta L}{\partial T} = \frac{1}{l_{a_1}} \frac{\partial l_{a_1}}{\partial T} + \frac{1}{n_{a_1}} \frac{\partial n_{a_1}}{\partial T}$$

For a fused quartz delay element approximately 15-cm long, this change would be of the order of 5 wavelengths per degree centigrade. If this element were suitably mounted in a cylinder of stainless steel, this increase in optical path could be compensated. One such structure is illustrated in Fig. 7-2. The delay element (D) would be mounted inside the stainless tube (E) with its input end mounted rigidly (F) to the compensating tube and its reflecting end mounted to the tube by a flexible diaphragm (G). The diaphragm will allow the longitudinal motion due to difference in thermal expansion without a transverse motion. The increase in path length inside the dielectric would then be compensated by a decrease in the distance between the beam-splitter (H) and the mirror due to the thermal increase in length of the stainless tube. The tube would be mounted on the support structure near the free end of the delay element and it would therefore expand toward the beam splitter, whereas the optical path length change in the dielectric would be away from the beamsplitter. The mounting point (J) of the tube to the Invar structural members of the interferometer can be moved along the tube, allowing adjustment of the thermal compensation of the structure and, in fact, the thermal compensation of the entire interferometer. The total path is therefore compensated for temperature variations, thus maintaining fringe stability. This method will not quite compensate for motion of the apparent mirror position (K), for small angular variations, in the delay element. The difference of a few wavelengths, however, in the apparent position of this mirror relative to the reference mirror will not significantly degrade the angular tolerance of the interferometer.

7.4.1.4 Radiation Effects on the Optical Elements

All of the optical elements of the system have been considered to be of high-quality fused quartz. The resistance of this material to radiation darkening and index or density changes has been studied by a number of authors. (8, 9)

High-quality fused silica shows no change in transmittance in the region of interest with 10^8 rads of 1-mev gamma rays and/or 10^{20} neutrons/sq cm. At 10^{20} neutrons/sq cm, there is a density change of a few percent. In the region below 10^{17} sq n/m there appears to be no such change in density. Considering the environment discussed in subsection 7.2.1, these will be no problem in the shielded alcove for the interferometer optics and only nominal shielding will be necessary in front of the relay optics.

7.4.2 Interferometer Structure

The interferometer structure is that portion of the system which supports and encloses the optical elements of the interferometer. It encompasses the mirror mounting structure, the coarse adjustment and stabilization structure, and the thermally compensating elements of the interferometer. A candidate design configuration for the interferometer was shown in Fig. 7-2.

7.4.2.1 Stability

The stability of the velocimeter is largely dependent on the mechanical and thermal stability of the optical elements previously described and the interferometer structure. To obtain a 1-percent velocity accuracy, the interferometer structure must maintain a path-length difference stable to better than 1 percent of the maximum excursion. Since only a quarter wave is used for the full-scale velocity measurement, a path-length difference stable to better than $1/400$ of a wave is required.

An extremely rigid, thermally compensating structure is therefore required for the support of the optical elements of the interferometer. Several materials have been considered for the basic structure. The two low-expansion-coefficient materials with the most favorable characteristics are fused silica and Invar-36. Fused silica has the advantage of being matched in thermal expansion to the elements of the optical system. Invar, on the other hand, has the advantage of ease of machining and assembly, need less protection from impact, has a thermal conductivity 10 times that of fused silica, and a thermal coefficient of expansion only two to two and one half times that of fused silica.

For these preliminary design considerations, Invar has been chosen in preference to fused quartz for the interferometer structure. While the use of quartz as the interferometer structure would decrease the dimensional variations due to temperature, these variations are insignificant when compared to the optical path-length variation due to thermal index of refraction changes in the quartz optical delay element. As the structured material, Invar has a combination of low thermal expansion coefficient and sufficiently high thermal conductivity that will preclude misalignment of the interferometer due to thermal gradients in the structure. Invar allows the element mounts described previously to closely match the thermal coefficient of the optical elements and yet be capable of the fine machining and adjustment necessary to manufacture a practical interferometer.

7.4.2.2 Adjustment and Control

As discussed in subsection 7.4.1.3, the optical delay element mounted in its compensating tube will have the capability of adjusting the thermal compensation of the interferometer. There will also have to be a coarse adjustment mechanism (L) on the reference mirror (M) similar to that of the present interferometer. This mechanism can combine the functions of the coarse angular adjustment and wedge of the breadboard model by arranging to move the three adjusting screws together for a path-length adjustment. This adjustment is necessary to place the reference mirror at precisely the same optical distance from the beamsplitter as the apparent position of the mirror within the delay element at the operating temperature.

An LMSC-designed, compensated, differential screw mechanism can be used to eliminate path-length drift due to the adjusting screws. This mechanism can itself be thermally compensated to less than $1/10$ fringe/ $^{\circ}\text{C}$. The differential screw mechanism uses four materials with four different coefficients of expansion and allows adjustment of spacing over a large range while maintaining thermal compensation. Each of the two differential screws in each mechanism has a thermal expansion coefficient proportional to its pitch. Adjustment of the relative lengths of the two screws during assembly allows the sum of their length change with temperature to be adjusted

to compensate for the net negative thermal change in the two-material barrel of the mechanism. The mechanism can therefore adjust the spacing over an appreciable range and remain thermally compensated. Three of these adjusting screw mechanisms could be installed between the wall of the interferometer and the reference mirror mount (N) which is supported by a diaphragm (P). These mechanisms would then be capable of separate operation to adjust the tilt of the mirror or the three could be operated together to adjust the path length. These adjustments would be manual adjustments used to originally align the interferometer.

Electro-mechanical transducers placed between the mechanical adjusting mechanisms and the mirror mount could act as a combination of the fine adjustment and servo-control mechanism for adjusting both tilt and bias of the interferometer. If standard 1/2-in. by 1/2-in. piezoelectric cylinders (Q) are used for these electromechanical transducers, the combined tilt and bias range would be approximately \pm four fringes. This technique would eliminate the backlash and instabilities inherent in the complex spring mechanisms of the breadboard model. This range of adjustment should be sufficient to allow feedback control (described in the electronic subsections) to compensate for residual (after thermal compensation) thermal drift over a temperature range of approximately 5°C.

The course and fine adjustments can be designed to operate in the plane of the mirror surface and, therefore, the action of one adjusting screw can be decoupled from that of the other two.

7.4.2.3 Environment Control

The interferometer structure, which would be basically a box of 0.5-in.-thick Invar plates similar in construction to the breadboard instrument, would act (approximately) as an isothermal structure. It should be enclosed in a "thermal blanket" and temperature-controlled at slightly above ambient temperature in the alcove. Windows installed over all openings to the outside environment would seal out both dust and

moisture. The slightly elevated temperature should preclude condensation on the windows, even in a high humidity environment. The box can be slightly pressurized from a dry nitrogen source if necessary. The thermal blanket is desirable both for path-length stability and to preclude any thermal gradients over the box from misaligning the interferometer.

7.4.3 Electronics

The electronics discussed in this section include the tilt and bias sensing and servo system for interferometer control and the signal system for generation, detection, processing, and transmission of the signal caused by the Doppler frequency change.

7.4.3.1 Tilt and Bias Servo

There is a large residual thermal sensitivity even with the most careful design of a thermally compensated interferometer. It is unlikely that sufficient long-term stability can be obtained to preclude the necessity of adjusting the bias and/or tilt of the interferometer mirrors shortly before the event of interest. The tunnel area must be evacuated well before the event. Some remote control scheme will be needed to adjust the interferometer during the period between evacuation of the tunnel and the event. The suggested scheme would require tilt and bias sensing and a servo control system to operate the piezoelectric fine adjusting mechanisms. A system with the sensor outputs transmitted to the surface and a man to close the loop and adjust the interferometer from the surface has been examined. It appears more complicated and expensive to field such a system than to design one with a completely automatic feedback loop local to the interferometer.

A servo system similar to that shown in the block diagram in Fig. 7-3 should be capable of automatic control of the interferometer. The system would consist of: (1) a group of semiconductor photodiodes arranged in a cross-shaped pattern to sense tilt misalignment, (2) a monitor of the signal channel to sense the bias position, and (3) comparison electronics to convert this information into error signals and amplified voltages

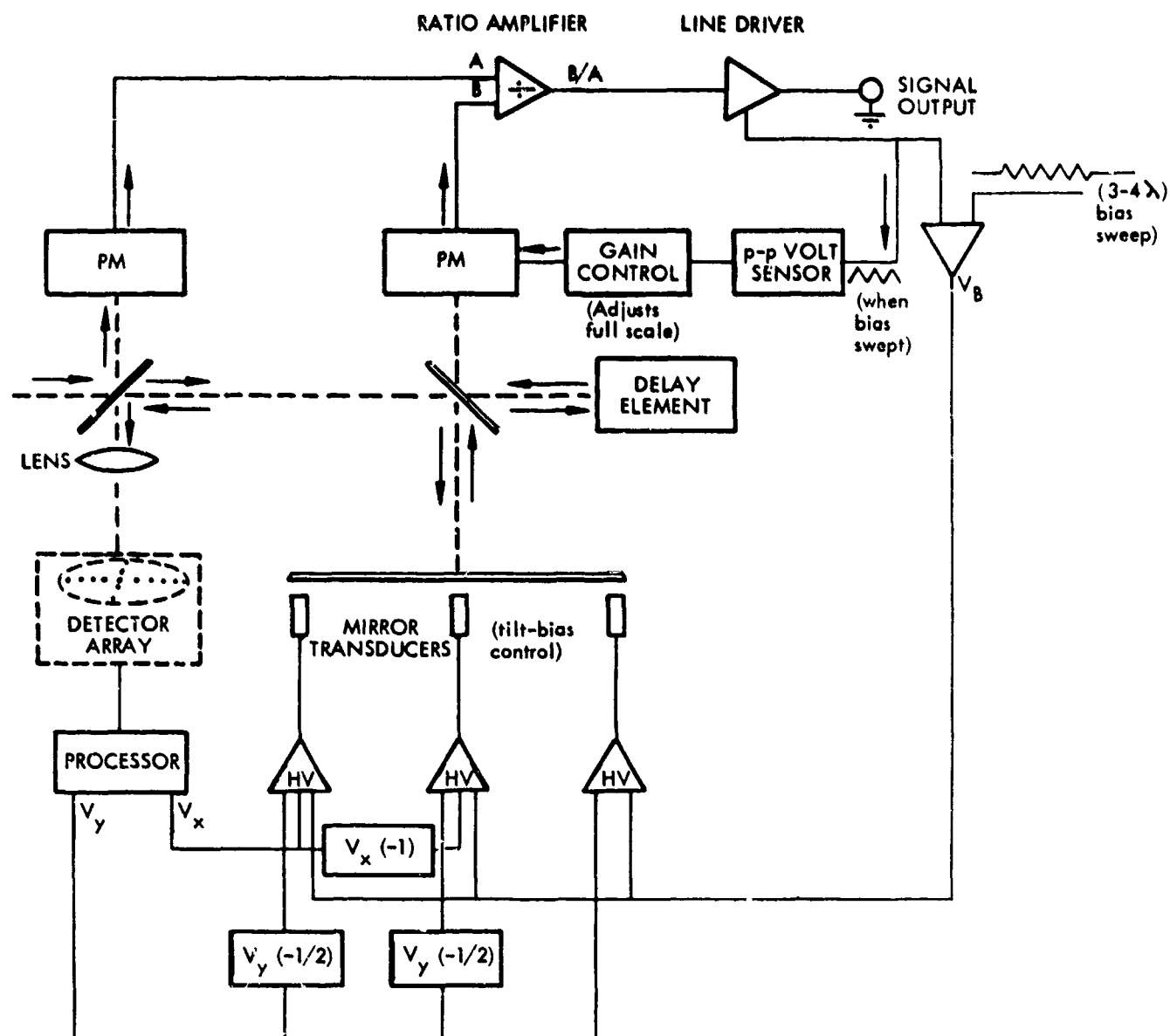


Fig. 7-3 Electronic Block Diagram

to drive the piezoelectric transducers on the reference mirror mount. The bias voltage would be swept periodically to automatically check the relative gains of the signal and reference photomultiplier and to establish zero and full-scale calibration for the recording electronics. The same bias sweep would be used to facilitate sensing of tilt misalignment. The tilt sensing detector array would be installed opposite the reference photomultiplier and would sense the unused output of the interferometer (reflected off the back of the reference beamsplitter).

The system would be designed to minimize radiation-induced effects, but, in any case, it should have a radiation sensitivity considerably less than the photomultipliers of the signal system discussed below. Any shielding adequate for the photomultipliers will protect this system.

7.4.3.2 The Signal System

The signal system will consist of the laser with its power supply, the photomultipliers and their power supplies, the ratio amplifier, and cable driving electronics and their supply. The coaxial cables with line equalizers and the recording equipment are considered to be GFE and a part of the underground test facility, as are the trigger and timing signals. As such, they are not discussed further, except when their performance requirements are stated. The cables, line equalizers, and recording instrumentation must be capable of transmitting and recording analog signals with rise times less than 10 nsec and have a dc capability for calibration of the equipment.

The laser and its power supply would be standard commercial equipment which, when installed in a suitably shielded alcove, should require little or no modification. The laser and its supply will have to be enclosed by the system structure to preclude the entrance of dust or moisture and also to shield against the electromagnetic pulse generated in the underground test. During the initial setup period, temperature fluctuations may be sufficient to require periodic adjustment of the laser; however, during the unattended period, alignment should not be needed. At worst, the problem could be solved in a manner analogous to the remote control scheme suggested for

the interferometer. Slight variations in laser power will, in any case, be removed by the ratio amplifier.

The photomultiplier power supplies are standard units and similar units have previously been operated in the underground test environment with no adverse effects. They should be enclosed in the system mounting structure which will provide electromagnetic shielding and environmental control.

The photomultipliers are the system components believed most sensitive to the radiation environment. A signal will be induced in the photomultiplier by incident nuclear radiation. Photoelectrons are generated in the tube structure and luminescence in the glass envelope by the radiation. Each high-energy photon absorbed in the structure can be expected to produce more than one photoelectron. However, most of these will be produced far down the dynode chain and should not experience the full multiplication effect. It is safe to assume that an "average" gamma photon absorbed in the tube is, at most, roughly as effective in generating a signal as a 6328 Å photon absorbed at the photocathode.

By considering Eq. (2.11) and a photomultiplier with 10 times the quantum efficiency of that used in the breadboard system, we obtain a minimum incident full-scale optical power for each photomultiplier of approximately 200 μ w. This 200 μ w signal corresponds to approximately 6×10^{14} photons per sec, releasing somewhat more than 3×10^{13} electrons per sec from the cathode. The photomultiplier will have a gamma absorption efficiency of about 10 percent, giving the reasonable density of about 10 lb/ft of structure internal to the photomultiplier. This structure's cross-section will not exceed 100 sq cm for typical photomultipliers.

To keep the effect on the signal well below 1 percent, 10^{11} absorbed photons per second or a gamma ray flux of 10^{10} photons/sq cm sec in the initial fast pulse can be tolerated. Shielding for the photomultipliers must therefore attenuate the gamma ray flux by a factor of approximately 4×10^{10} .

The earth between the alcove and the detonation will more than suffice to attenuate the direct radiation. Allowing for a buildup factor* of several hundred, and assuming that all gamma rays are the highly energetic nitrogen capture radiation (most are much less penetrating) and using the quoted tenth** value earth thickness for the nitrogen capture radiation (26 in.), we see that 26 ft of earth will adequately shield photomultipliers from the direct radiation and, hence, will shield the rest of the electronics.

The breadboard ratio amplifier which was developed under the contract is limited in flexibility by the choice and matching of components rather than by its basic design. By suitably choosing and matching transistors and diodes, the ratio amplifier could be greatly improved. Variations in input common to both channels could be accommodated over a range of as much as 10:1. An accuracy of 1 percent of the full-scale output should be possible for input ratios from 0.5 to 2. The elements of the ratio amplifier can be matched for a dc accuracy on the order of 1 percent for temperature variations over the range of 0 to 50°C, provided that the ratio amplifier is designed to minimize thermal gradients. The components also need to be chosen for matched high-frequency characteristics. The mechanical design of the ratio amplifier must be modified to allow it to survive as much as a 40-g ground shock after the event.

Additional amplification stages must be added to the output of the ratio amplifier. These are needed to drive the high frequency cable connecting the velocimeter output to recording equipment on the surface and to compensate for equalized cable losses. A driver amplifier output stage to maintain the high frequency capability of the ratio amplifier and to supply an approximately 2 v output into the 50 ohm cable is a routine design task. It is understood and assumed that cables with line equalizers which can have a flat response from dc out to 100 MHz with reasonable attenuation over the 2000 ft will be supplied as a test facility. The ratio amplifier and line driver electronics designed for the radiation environment should be considerably less sensitive to that environment than the photomultipliers previously described.

*Term for decrease in shield effectiveness at large thicknesses and/or with large-area shields, due to continued effectiveness of forward scattered photons.

**Absorber thickness which reduces radiation to 10 percent of incident value.

All of the electronic blocks associated with the velocimeter need to be isolated from the local earth ground and connected to a separate system ground to minimize noise.

A separate isolated power source will be necessary to supply all of the electronic equipment with standard 115-v power. The line power must be neither interrupted at time zero nor contain large transient changes at that time.

7.4.4 Calibration and Test Simulation

This subsection concerns itself both with laboratory calibration and simulation testing of the velocimeter system and calibration and "dry-run" test of the system in the underground environment.

7.4.4.1 Velocity Simulator

A velocimeter system, to be operated in the underground test environment, should be calibrated with the LMSC velocity simulator described in the final report and used to calibrate the breadboard velocimeter. The velocimeter system would need to be thermally stabilized and adjusted for its maximum angular sensitivity position (that position for which the interferometer's fringes are of maximum diameter). This position can be uniquely determined by the reaction of the interferometer to rotation about the center line of the interferometer. At this fixed temperature, then, the rotational speed of the wheel would be used to calibrate the output of the velocimeter. If the velocimeter is subsequently and at another location again stabilized at the same temperature and the point of maximum angular insensitivity is reset, the velocimeter would then have the same full-scale velocity calibration as determined in the laboratory calibration procedure. It would therefore not be necessary to set up the velocity simulator calibration at the underground test site.

7.4.4.2 Fast Pulser

No fast optical pulser was available for calibration of the rise time and common mode rejection of the breadboard velocimeter system previously described. Within the next few months, such a fast optical pulse source will be available within LMSC. The

equipment which would be used as a fast-pulse calibration source is a "mode-locked" helium-neon laser consisting of a Spectra Physics 125 laser and an internal cavity modulator operating at its cavity frequency. This gives rise to very fast, high-power pulses with a high repetition rate ideal for testing the response time and common mode rejection of the velocimeter equipment.

A secondary method has been devised to test the rise time of the velocimeter system. This pulse would be electrical and not optical. It would pulse the voltage on one dynode stage of one or both of the photomultipliers. If the voltage between the two dynodes on the photomultiplier is varied by 50 v with constant light input, the output signal will be decreased by as much as 90 percent. It is therefore possible to apply a fast rising pulse across one of the dynode stages and obtain a high degree of modulation of the output current. In this manner, a calibration pulse may be applied to the ratio amplifier, the line driver, and the cable and line equalizers, and may be recorded on the recording oscilloscopes. This same fast pulse may be used in any "dry runs" for testing the system and its interaction with other equipment. It should therefore not be necessary to transport the complicated optical pulser to the underground test site.

7.4.4.3 Gas Gun

The breadboard velocimeter discussed in the final report has been tested by measuring free surface velocities in the LMSC gas gun facility. Any velocimeter system for use in an underground test should be subjected to considerable simulation testing before being fielded. Extensive tests should be carried out on materials to be tested in the underground experiments. Gas gun tests would allow simulation of the remote sensing and automatic control characteristics of the velocimeter system during the measurement of actual shock phenomena. This would give experience with relating the type of data to be obtained from an underground shot with backface pressure and also improve the understanding of the present modeling.

7.5 CONCLUSIONS AND RECOMMENDATIONS

In this section, conclusions as to feasibility of using the laser velocimeter in the underground test environment are summarized. Tasks to redesign the velocimeter to include the performance capabilities outlined in the introduction are recommended. A comparison chart of the characteristics and performance capabilities of three types of laser velocimeters is also provided. These are the birefringent discriminator type such as the LASL instrument, the fringe counting interferometer typified by the Sandia instrument, and the LMSC compensated differential interferometer discriminator.

7.5.1 Conclusions

The problems of physical environment before, during, and after operation of the instrument have been examined in detail by interaction with LMSC personnel who have experience in underground testing. There appear to be no unmanageable problems imposed by any of these environmental situations.

The instrument will have to be built into its own mounting and shielding structure which would control its environment and then placed in an appropriately shielded alcove. The radiation shielding will have to be designed for the specific test in which the instrument is to be used. The specific flux expected to be scattered from the experimental station into the alcove and the accuracy to which the instrument is expected to operate must be considered in the shielding design. The various optical transfer elements are capable of being placed in a number of configurations allowing flexibility in the experimental setup. Only minimal shielding should be necessary to assure satisfactory operation of these elements. The laser velocimeter appears to be capable of surviving the ground shock and most other environmental conditions after the operational period.

The velocimeter design can be extended to cover maximum Doppler velocities as low as 100 m/sec. This will allow its operation with other materials having shock levels considerably below those examined by the breadboard velocimeter. The design

problems associated with stability of the velocimeter fringe pattern can be solved in a reasonably straightforward manner, even with the greater drifts of this extended velocity range. The interferometer structure will need considerable redesign using low thermal coefficient materials such as Invar and designing for thermal compensation. An apparently satisfactory solution has been developed for the continuous and vernier control and adjustment of the interferometer for extended time periods. This solution allows both adjustment of the central fringe to keep it centered on the detector aperture (tilt control) and longitudinal translational adjustment to maintain a desired bias point (intensity control).

The quality of the critical optical surfaces for the interferometer elements has been considered and it appears that state-of-the-art surfaces with a flatness of $1/2000$ wave or better are available and offer adequate accuracy for the interferometer system.

Experience with the breadboard velocimeter developed under the current contract described in the earlier sections shows that velocity can be measured within ± 3 percent of full scale and with 20-nsec resolution time and that these should not be regarded as best performance capability of the ratio amplifier. The ratio amplifier is limited in its flexibility by component selection and arrangement rather than by the basic design. By appropriately choosing both the components for the amplifier and its operating point, it should be possible to achieve a dynamic range of as much as 10 to 1. This dynamic range has proved adequate for gas gun tests with aluminum targets and should be adequate for successful tests with other metallic targets, even in the underground test environment.

Amplification of the output signal from the ratio amplifier is feasible within current state-of-the-art and compatible with expected signal degradation in the coaxial cable to the recording instrumentation if suitably equalized, high-frequency cables are available. Before any underground test of the instrument, however, this cable should be available to verify the distortion-free character of transmission through this extended length of to calibrate the distortion.

It appears possible to design the velocimeter to meet the overall objectives specified in the introduction to this addendum. The achievable velocity resolution and time resolution may have to be compromised to the choice of parameters of an instrument to be fielded as compared to one for laboratory use.

7.5.2 Recommendations

The experimental performance achieved with the breadboard velocimeter during the current contract shows the capability of upgrading to a prototype instrument. This can be a delivered item and can be used either in a laboratory or underground test application in a manner which would be comparable with other laboratory diagnostic techniques at a similar stage of development. The following three efforts represent what LMSC feels is needed in order to implement the design, building, and demonstration of the referenced instrument.

- Effort 1. Redesign and build the velocimeter to include the following characteristics and performance capabilities:
 - (a) A thermally stable and probably compensated interferometer structure of Invar and appropriate structure materials
 - (b) Higher quality optical elements for the critical interferometer components (approximately 0.01 fringe surface flatness)
 - (c) Improved design of the support for the critical optical components to minimize strain distortion
 - (d) A servoed support for the reference interferometer mirror to allow continuous or periodic correction of any drift in the interferometer pattern and, consequently, long-term stability of the velocimeter operating point
 - (e) Design of the exterior interferometer structure for thermal stabilization of the order of a few degrees
 - (f) Redesign of the ratio amplifier to minimize heating and vibrational effects and use of selected components to radiation-harden and improve speed and accuracy. The revision should also include an output stage to raise

the maximum output signal level to approximately 2 v and still be compatible with the input impedance represented by the cables carrying the signal to the recording instrumentation

- (g) Optional design for a lowest Doppler velocity range of approximately 100 m/sec (An instrument design to this specification could cover higher velocity ranges with the use of interchangeable delay elements while the converse is not true.)
- Effort 2. Integrate and test the total velocimeter as follows:
 - (a) Perform static tests which would include testing of the instrument in environmental chambers to evaluate performance under simulated temperature and humidity extremes. The purpose of these static tests would be particularly to observe the stability of velocimeter performance over the referenced environmental range.
 - (b) Perform careful dynamic testing with the use of the LMSC velocity simulator.
 - (c) Perform thorough dynamic testing in the LMSC gas gun facility with the use of various target materials of current interest and also including the use of non-specular reflection from the test samples.
- Effort 3. Participation in an underground test: The need to perform this task is to assure that the instrument usage would be in the hands of the people most familiar with its operation and most capable of insuring successful test results during its primary employment for this purpose.

7.5.3 Performance Comparison

A comparison of the performance and capabilities of three types of velocimeters is provided in Table 7-1.

COMPARISON OF VELOCIMETER TYPES

Design Considerations	Type		
	I - Uncompensated Unequal Path Differential Interferometer, Fringe Shift Counting	E - Birefringent Crystal FM Discriminator, Optical Intensity Measuring Over 1/2 Fringe	III - Compensated Equal Path Differential Interferometer FM Discriminator, Optical Intensity Measuring Over 1/4 Fringe
Critical Design Features (Optical)	<ol style="list-style-type: none"> 1. Quality of optical surfaces 2. Interferometer alignment 3. Accuracy of angles in fabric of optical prisms 4. Homogeneity of transmission components 	<ol style="list-style-type: none"> 1. Homogeneous crystal component 2. Optic axis alignment in crystal 3. Limited choice of crystal materials 	<ol style="list-style-type: none"> 1. Quality of optical surfaces 2. Interferometer alignment 3. Maintenance of adjustments 4. Low-reflection coatings 5. Adjustment of apparent optical path lengths (compensation) 6. Homogeneity of transmission components
Critical Design Features (Structural)	<ol style="list-style-type: none"> 1. Fabrication and/or adjustment to provide resolvable fringes 2. Design for thermal stability 3. Control of fringe shifts 4. Full-scale velocity set by length-refractive index product delay element 	<ol style="list-style-type: none"> 1. Optic axis alignment during fabrication of crystal 2. Thermal stabilization of crystal in particular 3. Full-scale velocity set by length-refractive index difference of delay element(a) 	<ol style="list-style-type: none"> 1. Provision of alignment/adjustment features 2. Distortion-free support 3. Design for thermal stability 4. Provision of beam splitting for reference channel 5. Full-scale velocity set by length-refractive index product of delay element
Critical Design Features (Electronic)	<ol style="list-style-type: none"> 1. Frequency response to match maximum fringe counting rate(b) 2. Fringe visibility and detection at maximum fringe counting rate 	<ol style="list-style-type: none"> 1. Provision of reference photo-detector channel 2. Provision of fast ratio amplifier to compensate intensity variation 3. Frequency response to match time resolution 	<ol style="list-style-type: none"> 1. Provision of reference photo-detector channel 2. Provision of fast ratio amplifier to compensate intensity variation 3. Frequency response to match time resolution
Display, Recording, and Readout of Data	<ol style="list-style-type: none"> 1. Fast CRT oscilloscope with photographic record 2. Digital time history with time markers set by fringe maxima or minima 	<ol style="list-style-type: none"> 1. Fast CRT oscilloscope with synchronous sweep trigger and photographic record 2. Analog time history with some calibratable non-linearity from discriminator and from non-linear amplifier effects 	<ol style="list-style-type: none"> 1. Fast CRT oscilloscope with synchronous sweep trigger and photographic record 2. Analog time history with some calibratable non-linearity from interference and from non-linear ratio effects
Design Advantages	<ol style="list-style-type: none"> 1. Interferometer design and adjustment relatively uncritical 2. Absolute measurement independent of intensity 	<ol style="list-style-type: none"> 1. Advantages of optical in-line system 2. Simple alignment scheme 3. No output velocity ambiguity 	<ol style="list-style-type: none"> 1. Large interferometer apertures are possible 2. Optical components of needed quality and precision are state-of-the-art 3. Relatively large acceptance cones for incident light 4. Large range of full-scale Doppler velocity easily accommodated 5. Lends itself to high thermal stability design(c) 6. Analog output record minimizes data reduction needs 7. No output velocity ambiguity 8. Inherent equal interfering beams
Design Disadvantages	<ol style="list-style-type: none"> 1. Velocity resolution limited by maximum fringe number (d) 2. No analog output record - data reduction needed 3. High-velocity range difficult to accommodate 4. Possible ambiguity in output on velocity reversal 5. Laser source of long coherence required 6. Very small acceptance angle for incident light 7. Special effort to maximize fringe visibility 	<ol style="list-style-type: none"> 1. Optical crystal components of high quality and large size not available 2. Resulting velocimeter aperture sizes are small 3. Low end of Doppler velocity range hard to accommodate 4. Relatively small cone for incident light 5. Birefringent crystals are thermally sensitive - thermal stabilization needed 6. Not absolute instrument - use of reference beam is required 	<ol style="list-style-type: none"> 1. Not absolute instrument - use of reference beam and a compensation scheme needed 2. Relatively stringent adjustment requirements

<p>velocity easily accommodated</p> <p>5. Lends itself to high thermal stability design (c)</p> <p>6. Analog output record minimizes data reduction needs</p> <p>7. No output velocity ambiguity</p> <p>8. Inherent equal interfering beams</p>	<p>1. Not absolute instrument - use of reference beam and a compensation scheme needed</p> <p>2. Relatively stringent adjustment requirements</p>	<p>1. Optical crystal components of high quality and large size not available</p> <p>2. Resulting velocimeter aperture sizes are small</p> <p>3. Low end of Doppler velocity range hard to accommodate</p> <p>4. Relatively small cone for incident light</p> <p>5. Birefringent crystals are thermally sensitive - thermal stabilization needed</p> <p>6. Not absolute instrument - use of reference beam and a compensation scheme needed</p> <p>7. Special effort to maximize fringe visibility</p>	<p>100 m/sec to desired upper limit</p> <p>± 1° based on 10² m/sec maximum Doppler velocity</p>	<p>Drift of 25 percent of full-scale range, 0.01°C without thermal compensation - with thermally compensated design, 0.25-2.5 percent drift per 0.01°C (f)</p>	<p>10 nsec with 100-MHz video bandwidth</p>	$\frac{S}{N} = K'' \gamma_{11} \left(\frac{\Omega_a P_L A}{\Delta f} \right)^{1/2}$
<p>Design Disadvantages</p>	<p>1. Velocity resolution limited by maximum fringe number (d)</p> <p>2. No analog output record - data reduction needed</p> <p>3. High-velocity range difficult to accommodate</p> <p>4. Possible ambiguity in output on velocity reversal</p> <p>5. Laser source of long coherence required</p> <p>6. Very small acceptance angle for incident light</p> <p>7. Special effort to maximize fringe visibility</p>	<p>Dependent (e)</p>	<p>Dependent on aperture and velocity range. Sample value: ~2 arc min (e)</p>	<p>Drift of 2.3 percent of full-scale range per 0.01°C without thermal compensation. Thermal compensation feasible (f)</p>	<p>10 nsec for 100-MHz BW - 100 nsec for 100-MHz BW for full-scale change within listed resolution time (g)</p>	$\frac{S}{N} = K'' \gamma_{11} \left(\frac{\Omega_a P_L A}{\Delta f} \right)^{1/2}$
<p>Velocity Range</p>	<p>Dependent (e)</p>					
<p>Acceptance Angle</p>						
<p>Thermal Stability</p>						
<p>Time Resolution</p>						
<p>Sensitivity</p>						

(a) Refractive index difference is that of ordinary and extraordinary rays, i.e., $n_o - n_e$.

(b) Maximum needed fringe counting rate equals maximum number of fringes, N (for full velocity range), divided by minimum time interval in which they may occur. Worst case would be N divided by τ , the desired time resolution. This is approximately the frequency response needed.

(c) Based on use of fused quartz optics and Invar or Super Invar-A support structure.

(d) Velocity resolution limited to $1/2N$ times full-scale velocity range. Attempts to improve resolution by increasing N result in impractical path differences. For example, for N fringe shifts $N = \Delta L / \lambda (2v_D / c)$. With $\lambda = 0.63 \times 10^{-6}$ m, $v_D = 10^3$ m/sec, $c = 3 \times 10^8$ m/sec, $\Delta L = 0.096$ N m. For $N = 10$, $\Delta L = 0.96$ m; $N = 100$, $\Delta L = 9.6$ m. For large enough ΔL , the coherence length will be exceeded.

(e) This depends on the detection visibility of interference fringes. High laser power, large acceptance angle, high mutual coherence (associated with short differential paths), and detector sensitivity all enhance detection visibility. Low laser power, small acceptance angle, low mutual coherence, and low detector sensitivity all degrade detection visibility.

(f) Based on 1-in. aperture beam splitter and 9.6-m differential air path (100 m/sec velocity range) and maximum deviation of half fringe.

(g) Based on 1-cm aperture \times 10-cm length calcite crystal which currently seems maximum component size which can be obtained.

(h) Using a differential air path of 9.5 m to obtain 10⁻⁷ m/sec full-scale with 10 fringe shift.

(i) Using crystal length of (e), and following information: Full velocity scale - 1000 m/sec, corresponding to $\pi/2$ phase shift $n_o = 1.655$, $n_e = 1.455$, coefficient of expansion (normal to C-axis) = $-5.5 \times 10^{-6}/^\circ\text{C}$, temperature coefficient of $n_o = 2.1 \times 10^{-6}/^\circ\text{C}$, (temperature coefficient of n_e) = $11.8 \times 10^{-6}/^\circ\text{C}$, $\lambda = 0.63 - 0.64$ microns, temperature range: $0^\circ - 60^\circ\text{C}$.

(j) Using delay element of 15 cm length maximum ($v_D = 100$ m/sec) and based on temperature change in optical path length in fused quartz. With maximum $v_D = 1000$ m/sec, the drifts are reduced to $1/10$ values given.

(k) Factors are as follows: γ_{11} is mutual coherence (maximum value, 1.0), Ω_a is solid acceptance angle, P_L is available laser power, A is area of limiting aperture in velocimeter, and Δf is electronic bandwidth. The η -factor is special to the fringe counting velocimeter and is the signal attenuation if used beyond the frequency response limit.

Section 8
LIST OF SYMBOLS

c	Velocity of light
I	Actual light intensity output
I_0	Maximum light intensity output
ΔL	Total optical path difference of the interferometer
l	Geometric distances
n	Index of refraction
T	System response time
α	Angle between light ray and normal to surface
ϵ	Angle between incoming beam and normal to the interferometer aperture
θ	Optical phase difference
λ_0	Unshifted wave length
ν	Frequency
ν_0	Unshifted frequency
ν_D	Doppler difference frequency
ϕ	Phase bias
τ	Travel time difference of interferometer

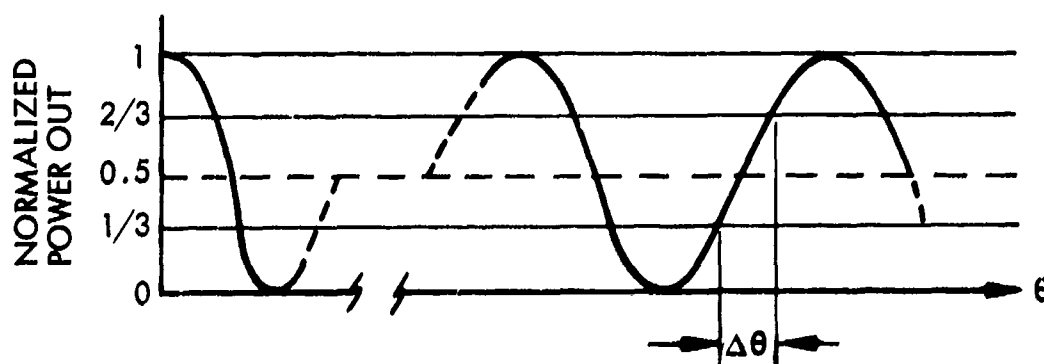
Section 9
REFERENCES

1. Sandia Laboratory, Fine Structure of Compressive and Release Wave Shapes in Aluminum Measured by the Velocity Interferometer Technique, by L. M. Barker, SC-DC-66-2447, Albuquerque, New Mexico, 1966.
2. L. M. Barker and R. E. Hollenback, "Interferometer Technique for Measuring the Dynamic Mechanical Properties of Materials," Review of Scientific Instruments, Vol. 36, No. 11, Nov 1965
3. G. Stavis, "New Velocity Sensing Technique Using Laser Light," Proceedings of the East Coast Conference on Navigational Electronics, Oct 1964
4. G. A. Morton, "Image Intensifiers and the Scotoscope," Applied Optics, Vol. 3, No. 6, Jun 1964
5. Lockheed Missiles & Space Company, Laser Velocimeter Development, Bimonthly Progress Report No. II, LMSC-677936, Sunnyvale, Calif., 9 May 1967
6. Glasstone, ed., Effects of Nuclear Weapons, VSAEC, 1962
7. Defense Atomic Security Agency, TREE Handbook (Unclassified portions of SRD supplement), DASA 1420-1, Washington, D.C.
8. United States Government, Space Materials Handbook, 2nd Edition, ML-TDR-64-40, pp. 193-197
9. Corning Optical, Properties of Fused Silica, Code 17/40

BLANK PAGE

Appendix A SELECTION OF ΔL

To operate on the linear portion of the intensity curve with a minimum of error, the bias control is used to set the initial point of the system such that the maximum excursion along the FM-AM response curve of the interferometer will occur symmetrically about the half-intensity point (see sketch below). As a compromise between linearity and maximum utilization of the curve, a value of ΔL should be chosen such that the signal will go initially from approximately $1/3$ maximum output to $2/3$ maximum output at the maximum expected velocity, v_{\max} .



Under these conditions, the change of phase is given by

$$\cos^2 \frac{\theta_1}{2} = \frac{1}{3} \quad , \quad \cos^2 \frac{\theta_f}{2} = \frac{2}{3} \quad ;$$

$$\frac{\theta_1}{2} \approx \pm (54.5^\circ \pm 2n\pi) \quad , \quad \frac{\theta_f}{2} \approx \pm (34.5^\circ \pm 2n\pi)$$

Therefore, $\Delta \theta \approx 40^\circ = \frac{2\pi}{9} \text{ rad}$.

The required path difference is then

$$\Delta L = \Delta \theta \left[\frac{\lambda_0}{2\pi} \frac{c}{2v_{\max}} \right] .$$

Choice of ΔL now depends upon the maximum velocity expected and the system may be adjusted to get an excursion from $\frac{I_{\max}}{3}$ to $\frac{2I_{\max}}{3}$. If, for example, $v_{\max} = 10^5$ cm/sec we find

$$\Delta L = 1.05 \text{ cm}$$

Appendix B

DETERMINATION OF $L(\epsilon)$

As seen from the text, ΔL must remain a constant from one measurement to the next to facilitate calibration and also to prevent any movement on the $\cos^2 \frac{\theta}{2}$ output curve that is not due to Doppler shift. Assuming that the discriminator can be built in such a fashion as to eliminate changes in ΔL due to thermal stress and mechanical vibration, the remaining source of change can be attributed to angular variations of the input beam. This effect becomes important when using convergent light or a moving beam.

A mathematical analysis, requiring that ΔL be approximately constant for small variations to input beam angle, is given below for both the singlet system (one dielectric delay element) and the multiplet (many dielectric) system.

B.1 THE SINGLET SYSTEM

This is the system employed experimentally and outlined in the text. Figure B-1 depicts the elements of the system and associated notation. Note that Fig. B-1 illustrates the special case where the effective length to the mirror in the dielectric arm, $l_{a\epsilon}$ and the length to the second mirror l_{bo} are equal. This is not exactly true for all angles, and in fact it is this variation that is the crux of the analysis. It is shown in subsection B.2 that this variation can be made to vanish with an infinite number of dielectric plates.

Our analysis assumes the following.

- (1) The two mirrors make equal angles with the beamsplitter. This can be accomplished by careful adjustment of one mirror.
- (2) All dielectric surfaces in a given arm (other than the beamsplitter) are parallel to the mirror surface in that arm.

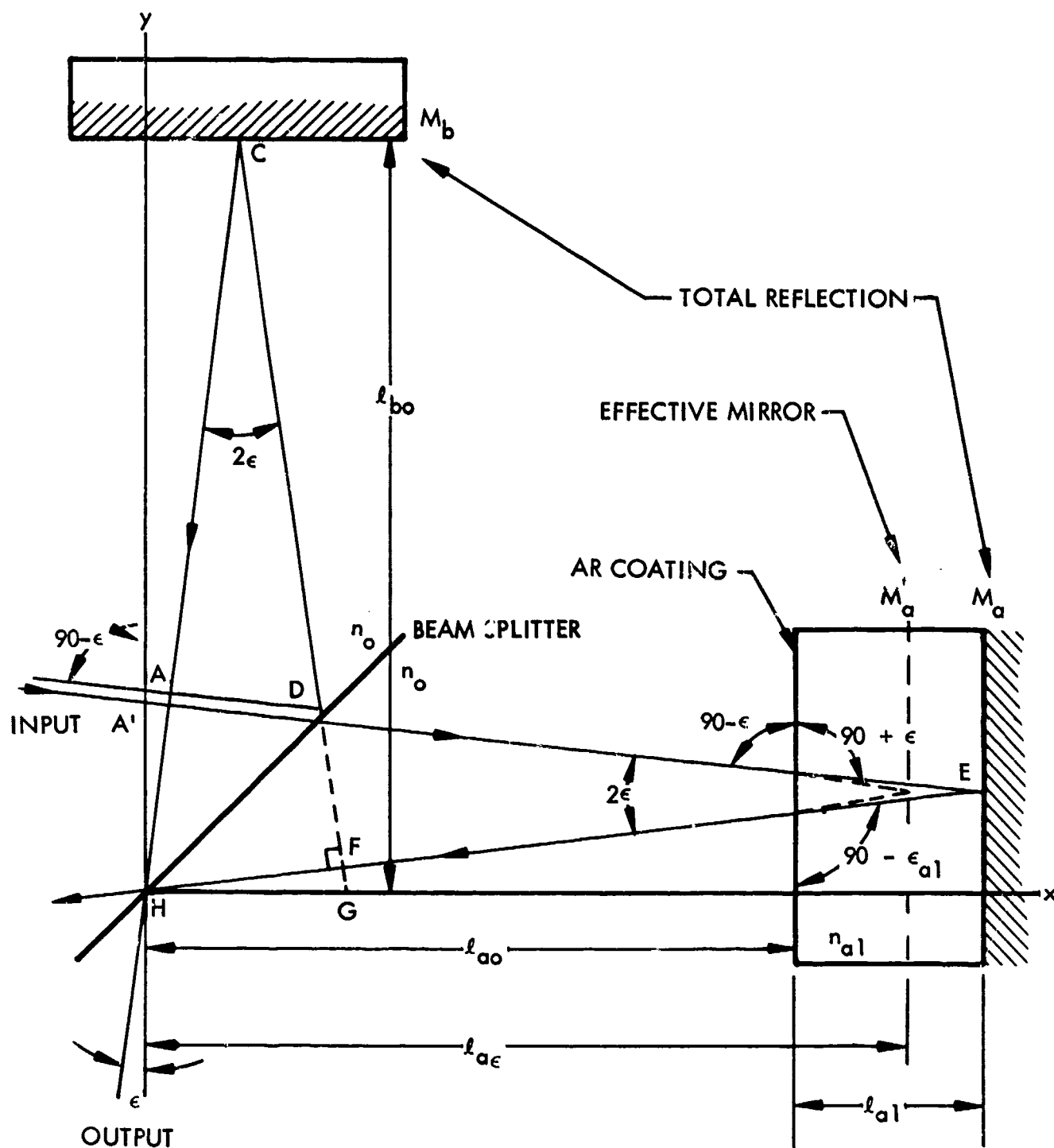


Fig. B-1 The Singlet Interferometer

B-2

LOCKHEED MISSILES & SPACE COMPANY

- (3) The beam splitter is an infinitely thin plane. This can be approximated through the use of a parallel plate beam splitter and compensator.
- (4) The space on both sides of the beam splitter has a refractive index of n_o .
- (5) Snell's Law: $n \sin x = n' \sin x'$.

Referring to Fig. B-1,

$$\Delta L^* = B'EH - BDCH \quad (B.1)$$

Note from symmetry that

$$AD = DG \text{ and } AB = GF$$

Now

$$\Delta L = (A'EH - A'B') - (GCH - GF) \quad (B.2)$$

Given the physical distances l_{ao} , l_{bo} , l_{a1} , $l_{a\epsilon}$, the optical path lengths may be evaluated term by term.

$$A'EH = 2 \left(\frac{n_{a1} l_{a1}}{\cos \epsilon_{a1}} + \frac{n_o l_{ao}}{\cos \epsilon} \right) \quad (B.3)$$

$$A'B' = n_o (HA') \sin \epsilon$$

$$HA' = 2 (l_{ao} \tan \epsilon + l_{a1} \tan \epsilon_{a1})$$

$$A'B' = 2 (l_{ao} \tan \epsilon + l_{a1} \tan \epsilon_{a1}) n_o \sin \epsilon$$

$$A'B' = 2 \left(n_o l_{ao} \frac{\sin^2 \epsilon}{\cos \epsilon} + n_{a1} l_{a1} \frac{\sin^2 \epsilon_{a1}}{\cos \epsilon_{a1}} \right) \quad (B.4)$$

* ΔL = optical path length differential of interferometer

$$GCH = 2 \frac{n_o \ell_{bo}}{\cos \epsilon} \quad (B.5)$$

$$GF = n_o (GH) \sin \epsilon = 2 n_o \ell_{bo} \tan \epsilon \sin \epsilon$$

$$GF = 2 n_o \ell_{bo} \frac{\sin^2 \epsilon}{\cos \epsilon} \quad (B.6)$$

Gathering terms gives

$$\begin{aligned} \frac{\Delta L}{2} &= \frac{n_{a1} \ell_{a1}}{\cos \epsilon_{a1}} + \frac{n_o \ell_{ao}}{\cos \epsilon} - n_o \ell_{ao} \frac{\sin^2 \epsilon}{\cos \epsilon} - n_{a1} \ell_{a1} \frac{\sin^2 \epsilon_{a1}}{\cos \epsilon_{a1}} - \frac{n_o \ell_{bo}}{\cos \epsilon} \\ &\quad + n_o \ell_{bo} \frac{\sin^2 \epsilon}{\cos \epsilon} \end{aligned}$$

$$\frac{\Delta L}{2} = \frac{n_o (\ell_{ao} - \ell_{bo})(1 - \sin^2 \epsilon)}{\cos \epsilon} + \frac{n_{a1} \ell_{a1} (1 - \sin^2 \epsilon_{a1})}{\cos \epsilon_{a1}}$$

$$\frac{\Delta L}{2} = n_o (\ell_{ao} - \ell_{bo}) \cos \epsilon + n_{a1} \ell_{a1} \cos \epsilon_{a1} \quad (B.7)$$

$$\frac{\Delta L}{2} = n_o (\ell_{ao} - \ell_{bo}) [1 - \sin^2 \epsilon]^{1/2} + n_{a1} \ell_{a1} \left[1 - \frac{n_o^2 \sin^2 \epsilon}{n_{a1}^2} \right]^{1/2} \quad (B.8)$$

where we have made use of Snell's law $n_o \sin \epsilon = n_{a1} \sin \epsilon_{a1}$

With no dielectric (i.e., with $n_o = n_{a1}$ and $\ell_a = \ell_{ao} + \ell_{a1}$, $\ell_b = \ell_{bo}$) this reduces to

$$\frac{\Delta L(\epsilon)}{2} = n_o (\ell_a - \ell_b) \cos \epsilon = n_o (\ell_a - \ell_b) (1 - \sin^2 \epsilon)^{1/2} \quad (B.9)$$

Equations (B.8) and (B.9) can be expanded in terms of $\sin^2 \epsilon$ and $\frac{n_o^2}{n_{a1}^2} \sin^2 \epsilon$ through the use of the binomial theorem. In the case of Eq. (B.9) there will be one $\sin^2 \epsilon$ term, one $\sin^4 \epsilon$ term, etc., giving the form

$$\frac{\Delta L(\epsilon)}{2} = n_o (\ell_a - \ell_b) (c_o + c_2 \sin^2 \epsilon + c_4 \sin^4 \epsilon + c_6 \sin^6 \epsilon + \dots)$$

However, when the expansion is applied to Eq. (B.8), two such series evolve, giving

$$\begin{aligned} \frac{\Delta L(\epsilon)}{2} = & n_o (\ell_{ao} - \ell_{bo}) (c_o + c_2 \sin^2 \epsilon + c_4 \sin^4 \epsilon + \dots) \\ & + n_{a1} \ell_{a1} (d_o + d_2 \sin^2 \epsilon + d_4 \sin^4 \epsilon + \dots) \end{aligned} \quad (B.10)$$

where $d_i \neq c_i$ due to the n_o^2/n_{a1}^2 factor. Regrouping terms gives

$$\begin{aligned} \frac{\Delta L(\epsilon)}{2} = & n_o (\ell_{ao} - \ell_{bo}) c_o + n_{a1} \ell_{a1} d_o \\ & + \sin^2 \epsilon [n_o (\ell_{ao} - \ell_{bo}) c_2 + n_{a1} \ell_{a1} d_2] \\ & + \sin^4 \epsilon [n_o (\ell_{ao} - \ell_{bo}) c_4 + n_{a1} \ell_{a1} d_4] \\ & + \dots \end{aligned} \quad (B.11)$$

By inspection it may be seen that for a correct choice of $(\ell_{ao} - \ell_{bo})$ and (assuming n_{a1} to be known) the $\sin^2 \epsilon$ term may be made zero. This reduces the dependence of ΔL on ϵ to fourth-order terms.

At this point it can be mentioned that the above expressions could have been expanded in powers of ϵ (expand the powers of $\sin \epsilon$ and regroup) to show the angular dependence directly, in which case the ϵ^2 term could have been made zero instead of the $\sin^2 \epsilon$ term. Actually both conditions are equivalent as $\sin^2 \epsilon$ is the only term which contains ϵ^2 . This is more easily seen in the analysis which follows and for which the expansions are detailed.

B.2 THE GENERAL SYSTEM

This system is treated analytically and gives $\Delta L(\epsilon)$ for any number of dielectrics. Figure B-2 is the counterpart to Fig. B-1. I and J are the number of dielectrics in each arm (i.e., the maximum values of i and j respectively). The basic assumptions listed in B.1 are also assumed here. The first seven equations in that section may be compared directly to Eqs. (B.12) through (B.18) below.

Again, considering only optical distances,

$$\Delta L = B'EH - BDCH$$

$$\Delta L = (A'EH - A'B') - (ADCH - AB)$$

Symmetry still holds, giving

$$AD = DG \text{ and } AB = GF$$

which results in

$$\Delta L = (A'EH - A'B') - (GCH - GF) \quad (B.12)$$

Evaluating each term separately:

$$A'EH = 2 \sum_{i=0}^I \frac{n_{ai} l_{ai}}{\cos \epsilon_{ai}} \quad (B.13)$$

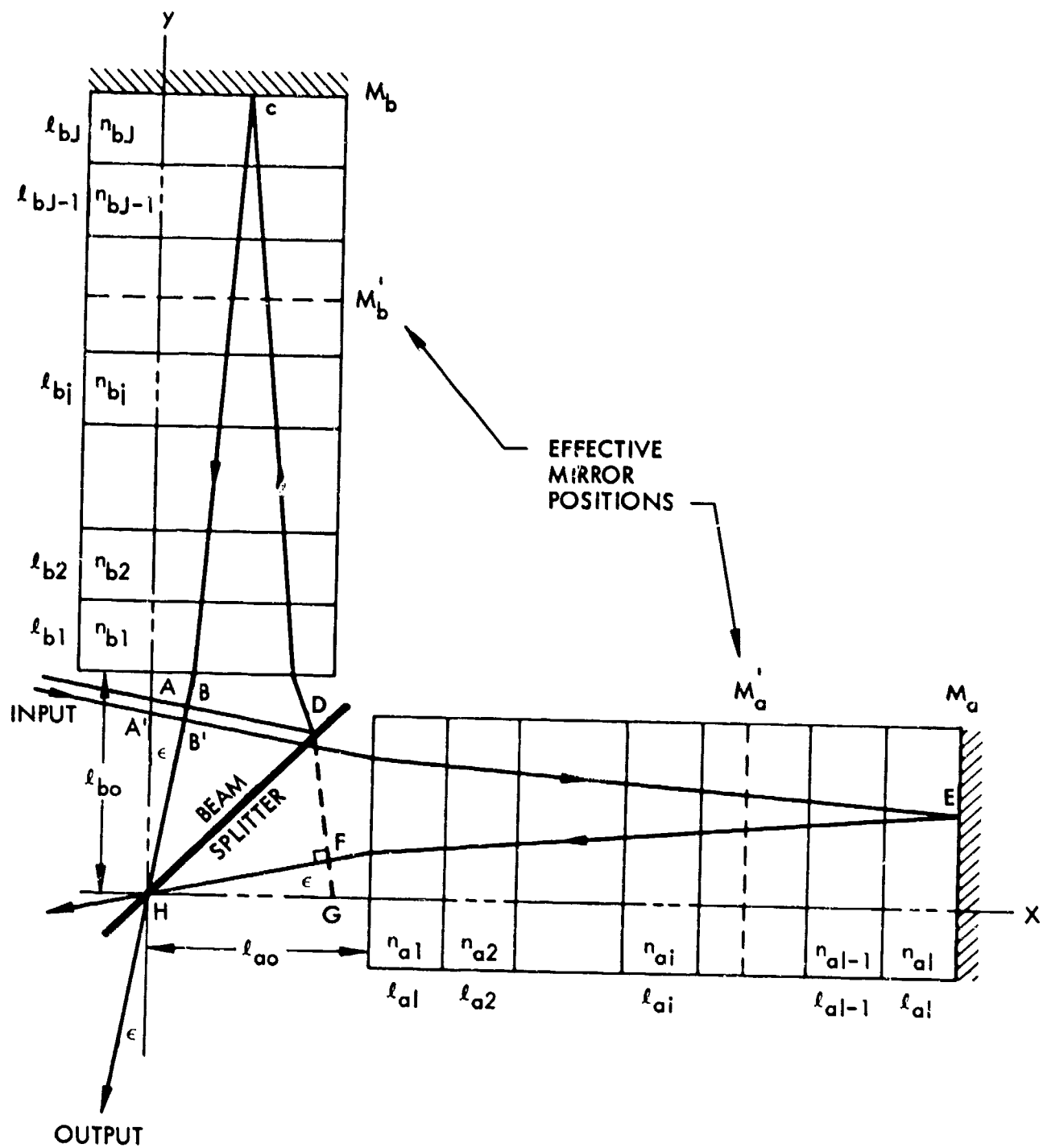


Fig. B-2 The General Differential Interferometer

B-7

LOCKHEED MISSILES & SPACE COMPANY

$$A'B' = n_o (HA') \sin \epsilon \quad \text{and} \quad HA' = 2 \sum_{i=0}^I \ell_{ai} \tan \epsilon_{ai} \quad (B.14)$$

$$A'B' = 2 \sum_{i=0}^I n_{ai} \ell_{ai} \frac{\sin^2 \epsilon_{ai}}{\cos \epsilon_{ai}}$$

$$GCH = 2 \sum_{j=0}^J \frac{n_{bj} \ell_{bj}}{\cos \epsilon_{bj}} \quad (B.15)$$

$$GF = n_o (GH) \sin \epsilon = 2n_o \sin \epsilon \sum_{j=0}^J \ell_{bj} \tan \epsilon_{bj}$$

$$GF = 2 \sum_{j=0}^J n_{bj} \ell_{bj} \frac{\sin^2 \epsilon_{bj}}{\cos \epsilon_{bj}} \quad (B.16)$$

Gathering terms gives

$$\begin{aligned} \frac{\Delta L(\epsilon)}{2} = & \sum_{i=0}^I \left(\frac{n_{ai} \ell_{ai}}{\cos \epsilon_{ai}} - \frac{n_{ai} \ell_{ai} \sin^2 \epsilon_{ai}}{\cos \epsilon_{ai}} \right) \\ & - \sum_{j=0}^J \left(\frac{n_{bj} \ell_{bj}}{\cos \epsilon_{bj}} - \frac{n_{bj} \ell_{bj} \sin^2 \epsilon_{bj}}{\cos \epsilon_{bj}} \right) \end{aligned}$$

$$\frac{\Delta L(\epsilon)}{2} = \sum_{i=0}^I \frac{n_{ai} \ell_{ai}}{\cos \epsilon_{ai}} (1 - \sin^2 \epsilon_{ai}) - \sum_{j=0}^J \frac{n_{bj} \ell_{bj}}{\cos \epsilon_{bj}} (1 - \sin^2 \epsilon_{bj})$$

$$\frac{\Delta L(\epsilon)}{2} = \sum_{i=0}^I n_{ai} f_{ai} \cos \epsilon_{ai} - \sum_{j=0}^J n_{bj} f_{bj} \cos \epsilon_{bj} \quad (B.17)$$

$$\frac{\Delta L(\epsilon)}{2} = \sum_{i=0, j=0}^{I, J} \left\{ n_{ai} f_{ai} \left(1 - \frac{n_o^2}{n_{ai}^2} \sin^2 \epsilon \right)^{1/2} - n_{bj} f_{bj} \left(1 - \frac{n_o^2 \sin^2 \epsilon}{n_{bj}^2} \right)^{1/2} \right\} \quad (B.18)$$

When $I = 1$ and $J = 0$, this expression is identical with Eq. (B.8). Using the binomial expansion

$$(1 + \zeta)^{1/2} = \sum_{p=1}^{\infty} \left\{ 1 + \frac{\prod_{r=1}^p [1/2 - (r-1)]}{p!} \zeta^p \right\}$$

on

$$\left[1 - \frac{n_o^2 \sin^2 \epsilon}{n} \right]^{1/2}$$

results in, after combining terms,

$$\begin{aligned} \frac{\Delta L(\epsilon)}{2} = & \sum_{i=0, j=0}^{I, J} \left\{ n_{ai} f_{ai} - n_{bj} f_{bj} + \sum_{p=1}^{\infty} \frac{\prod_{r=1}^p (3/2 - r)}{p!} \left(\frac{f_{ai}}{n_{ai}^{(2p-1)}} \right. \right. \\ & \left. \left. - \frac{f_{bj}}{n_{bj}^{(2p-1)}} \right) \left(-n_o^2 \sin^2 \epsilon \right)^p \right\} \quad (B.19) \end{aligned}$$

or,

$$\frac{\Delta L(\epsilon)}{2} = \sum_{i=0, j=0}^{I, J} \left\{ n_{ai} l_{ai} - n_{bj} l_{bj} - \sum_{p=1}^{\infty} A_p \epsilon \sin^{2p} \epsilon \right\} \quad (B. 20)$$

where

$$A_p = n_o^{2p} \left| \frac{\prod_{r=1}^p \left(\frac{3}{2} - r \right)}{p!} \right| \left(\frac{l_{ai}}{n_{ai}^{(2p-1)}} - \frac{l_{bj}}{n_{bj}^{(2p-1)}} \right) \quad (B. 21)$$

and $n_{ao} = n_{bo} = n_o$.

The requirement that $\Delta L(\epsilon)$ not contain $\sin^{2p} \epsilon$ is that

$$\sum_{i=0, j=0}^{I, J} A_p = 0 \quad (B. 22)$$

For $\epsilon = 0$

$$\frac{\Delta L(0)}{2} = \sum_{i=0, j=0}^{I, J} (n_{ai} l_{ai} - n_{bj} l_{bj}) \quad (B. 23)$$

Small variations from $\Delta L(0)$ are due to higher-order terms. The maximum number of higher-order terms that can be eliminated is equal to $I + J$. The total number of variables at hand is equal to the number of different indices of refraction that appear in both arms. Equal indices in the same arm add to give an effective combined length and in opposite arms subtract (as in the case of n_o around the beamsplitter). The total number of variables is then $I + J + 1$ (assuming different indices) where the 1 is due to n_o . Equation (B. 23) must always hold, which leaves $I + J$ equations of the form of Eq. (B. 21) which may be solved to eliminate $I + J$ higher-order terms. The variables are $(l_{ao} - l_{bo})$, l_{ai} , and l_{bj} .

In general, terms in a converging series will decrease as the term order increases. However, the above series was obtained by taking the difference of two converging series (which makes this series convergent) and may allow a dip or zero value to occur before the series finally goes to zero. The equations are transcendental in nature and require a graphical solution which at the present time is of academic interest only, as the $p = 1$ coefficient is larger than the $p = 2$ coefficient.

B.3 CALCULATION OF SYSTEM PARAMETERS

Calculation of system parameters is essentially a problem of solving $I + J + 1$ simultaneous equations.

B.3.1 Singlet Differential Interferometer $I = 1, J = 0$

Expanding Eq. (B.19) we find

$$\begin{aligned} \frac{\Delta L(\epsilon)}{2} = & n_o l_{ao} - n_o l_{bo} + n_{a1} l_{a1} \\ & - \frac{1}{2} \left(n_o l_{ao} - n_o l_{bo} + \frac{n_o^2}{n_{a1}} l_{a1} \right) \sin^2 \epsilon \\ & - \frac{1}{8} \left(n_o l_{ao} - n_o l_{bo} + \frac{n_o^4}{n_{a1}^3} l_{a1} \right) \sin^4 \epsilon - \dots \end{aligned} \quad (B.24)$$

Setting the coefficient of $\sin^2 \epsilon$ equal to zero and setting $\epsilon = 0$ gives the two conditions

$$0 = n_o l_{ao} - n_o l_{bo} + \frac{n_o^2}{n_{a1}} l_{a1} \quad (B.25)$$

$$\frac{\Delta L(0)}{2} = n_o l_{ao} - n_o l_{bo} + n_{a1} l_{a1} \quad (B.26)$$

Subtracting gives

$$\frac{\Delta L(o)}{2} = \ell_{a1} \left(n_{a1} - \frac{n_o^2}{n_{a1}} \right) \quad (B.27)$$

which results in

$$\ell_{a1} = \frac{\Delta L(o)}{2} \left(\frac{n_{a1}}{n_{a1}^2 - n_o^2} \right) \quad (B.28)$$

$$\ell_{ao} - \ell_{bo} = - \frac{\Delta L(o)}{2} \left(\frac{n_o}{n_{a1}^2 - n_o^2} \right) \quad (B.29)$$

Thus combining Eqs. (B.24), (B.28), and (B.29) we obtain

$$\frac{\Delta L(\epsilon)}{2} = \ell_{a1} \left(n_{a1} - \frac{n_o^2}{n_{a1}} \right) + \frac{1}{8} \frac{n_o^2}{n_{a1}} \ell_{a1} \left(1 - \frac{n_o^2}{n_{a1}^2} \right) \sin^4 \epsilon + \dots, \quad (B.30)$$

where

$$\ell_{bo} = \ell_{ao} + \frac{n_o \ell_{a1}}{n_{a1}} \quad (B.31)$$

Equation (B.31) is simply the condition for making the distance from the beam splitter to M_b and the apparent position of M_a equal. Using

$$n_{a1} = 1.46 \quad (\text{fused silica})$$

$$\Delta L(o) = 1.05 \quad (\text{from Appendix A})$$

$$n_o = 1.0$$

gives values of $(\ell_{ao} - \ell_{bo}) = -0.46$ cm and $\ell_{a1} = 0.68$ cm. Equation (B.30) now becomes

$$\Delta L(\epsilon) = 1.05 + 0.06 \sin^4 \epsilon$$

Using this result we can estimate the off-axis performance of the singlet interferometer. Solving for ϵ when

$$\Delta L(\epsilon) - \Delta L(o) = \frac{\lambda_o}{10} \quad \text{where} \quad \lambda_o = 6.328(10^{-5}) \text{ cm}$$

we find

$$\sin^4 \epsilon = \frac{\lambda_o}{0.6} = 1.05(10^{-4})$$

$$\epsilon \approx 5.8 \text{ deg}$$

At

$$\Delta L(\epsilon) - \Delta L(o) = \frac{\lambda_o}{100}, \quad \epsilon \approx 3.3 \text{ deg}$$

B.3.2 The Doublet System [I = J = 1, see Fig. B-3]

By expanding Eq. (B.19) we find

$$\begin{aligned} \frac{\Delta L(\epsilon)}{2} &= n_o \ell_{ao} - n_o \ell_{bo} + n_{a1} \ell_{a1} - n_{b1} \ell_{b1} \\ &\quad - \frac{1}{2} \left(n_o \ell_{ao} - n_o \ell_{bo} + \frac{n_o^2}{n_{a1}} \ell_{a1} - \frac{n_o^2}{n_{b1}} \ell_{b1} \right) \sin^2 \epsilon \end{aligned}$$

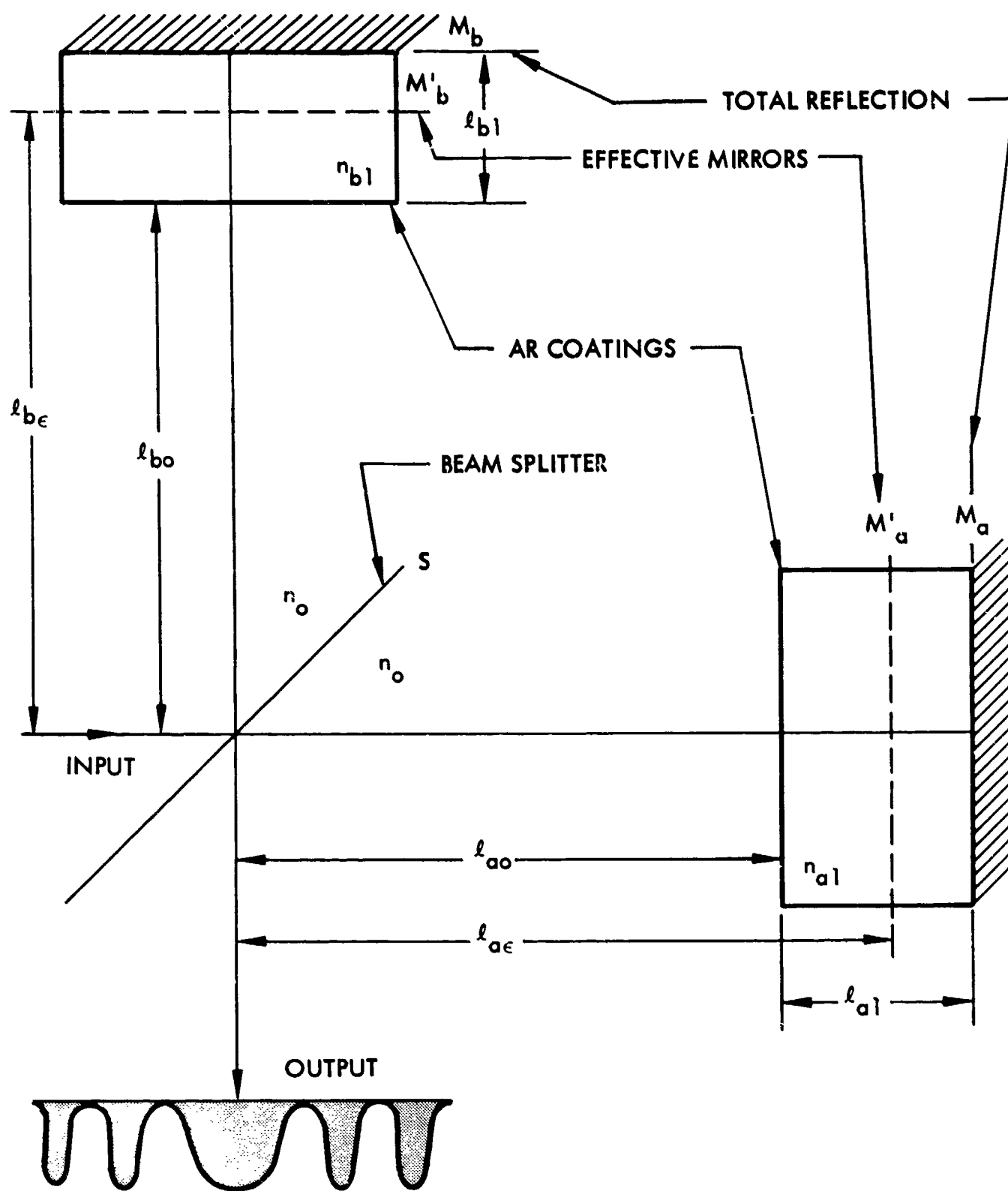


Fig. B-3 The Doublet Differential Interferometer

$$\begin{aligned}
& -\frac{1}{8} \left(n_o \ell_{ao} - n_o \ell_{bo} + \frac{n_o^4}{n_{a1}^3} \ell_{a1} - \frac{n_o^4}{n_{b1}^3} \ell_{b1} \right) \sin^4 \epsilon \\
& -\frac{1}{16} \left(n_o \ell_{ao} - n_o \ell_{bo} + \frac{n_o^6}{n_{a1}^5} \ell_{a1} - \frac{n_o^6}{n_{b1}^5} \ell_{b1} \right) \sin^6 \epsilon + \dots \quad (B.32)
\end{aligned}$$

Setting the coefficients of $\sin^2 \epsilon$ and $\sin^4 \epsilon$ equal to zero and setting $\epsilon = 0$ gives the three conditions

$$0 = n_o \ell_{ao} - n_o \ell_{bo} + \frac{n_o^2}{n_{a1}} \ell_{a1} - \frac{n_o^2}{n_{b1}} \ell_{b1} \quad (B.33)$$

$$0 = n_o \ell_{ao} - n_o \ell_{bo} + \frac{n_o^4}{n_{a1}^3} \ell_{a1} - \frac{n_o^4}{n_{b1}^3} \ell_{b1} \quad (B.34)$$

$$\frac{\Delta L(o)}{2} = n_o \ell_{ao} - n_o \ell_{bo} + n_{a1} \ell_{a1} - n_{b1} \ell_{b1} \quad (B.35)$$

Solving these we find setting

$$D = \frac{n_o^4}{n_{a1}^3 n_{b1}} - \frac{n_o^4}{n_{a1} n_{b1}^3} - \frac{n_o^2 n_{b1}}{n_{a1}^3} + \frac{n_o^2 n_{a1}}{n_{b1}^3} + \frac{n_{b1}}{n_{a1}} - \frac{n_{a1}}{n_{b1}} \quad (B.36)$$

$$\ell_{ao} - \ell_{bo} = \frac{n_o^3 \Delta L(o)}{2 n_{a1} n_{b1}} \left[\frac{1}{n_{a1}^2} - \frac{1}{n_{b1}^2} \right] / D \quad (B.37)$$

$$\ell_{a1} = - \frac{\Delta L(o)}{2 n_{b1}} \left[1 - \frac{n_o^2}{n_{b1}^2} \right] / D \quad (B.38)$$

$$\ell_{b1} = - \frac{\Delta L(o)}{2n_{a1}} \left[1 - \frac{n_o^2}{n_{a1}^2} \right] / D \quad (B.39)$$

Thus by combining Eqs. (B.32), (B.37), (B.38), and (B.39)

$$\begin{aligned} \frac{\Delta L(\epsilon)}{2} = & \ell_{a1} \left(n_{a1} - \frac{n_o^2}{n_{a1}} \right) - \ell_{b1} \left(n_{b1} - \frac{n_o^2}{n_{b1}} \right) \\ & - \frac{1}{16} \left[\frac{n_o^2}{n_{b1}} \ell_{b1} \left(1 - \frac{n_o^4}{n_{b1}^4} \right) - \frac{n_o^2 \ell_{a1}}{n_{a1}} \left(1 - \frac{n_o^4}{n_{a1}^4} \right) \right] \sin^6 \epsilon \end{aligned} \quad (B.40)$$

subject to

$$\ell_{ao} + \frac{n_o \ell_{a1}}{n_{a1}} = \ell_{bo} + \frac{n_a \ell_{b1}}{n_{b1}} \quad (B.41)$$

and

$$\frac{\ell_{a1}}{n_{a1}} \left(1 - \frac{n_o^2}{n_{a1}^2} \right) = \frac{\ell_{b1}}{n_{b1}} \left(1 - \frac{n_o^2}{n_{b1}^2} \right) \quad (B.42)$$

Condition (B.41) is the requirement that the distances from the beam splitter to apparent mirror positions M'_a and M'_b are equal at $\epsilon = 0$.

Using

$$n_{a1} = 1.52 \quad (\text{fused silica})$$

$$n_{b1} = 1.46 \quad (\text{Borosilicate glass})$$

$$\Delta L(o) = 1.05$$

$$n_o = 1.0$$

gives

$$l_{ao} - l_{bo} = 0.41 \text{ cm}$$

$$l_{a1} = 8.5 \text{ cm}$$

$$l_{b1} = 8.8 \text{ cm}$$

Using these parameters Eq. (B.40) becomes)

$$\Delta L(\epsilon) = 1.05 + 0.02 \sin^6 \epsilon$$

Checking off-axis performance, for $\Delta L(\epsilon) - \Delta L(o) = \lambda_o/10$ we find $\epsilon \approx 15 \text{ deg}$ and for $\Delta L(\epsilon) - \Delta L(o) = \lambda_o/100$, $\epsilon \approx 10 \text{ deg}$.

However, we can see that this system would be difficult to build due to the relatively large lengths of dielectric elements needed. Also variation of reactive index is difficult due to the limited number of dielectrics available.

BLANK PAGE

Appendix C
AN EXAMINATION OF THE COHERENCE AND TIME-AVERAGING
QUESTIONS FOR THE DIFFERENTIAL INTERFEROMETER

C.1 MUTUAL COHERENCE

The importance of coherence effects in the laser velocimeter in producing systematic errors is significant in that it is related to the ultimate accuracy of the system. An investigation of this problem using a time-domain analysis shows that with proper biasing these effects may be kept well within acceptable limits for the application at hand. Errors introduced when instantaneous values are compared with time-averaged intensities were also studied and found to be within acceptable limits.

We assume a differential interferometer whose travel time difference is τ (Fig. C-1).

At the detector d we have the electric vector at time $t + t_a + t_b + \tau$ given by

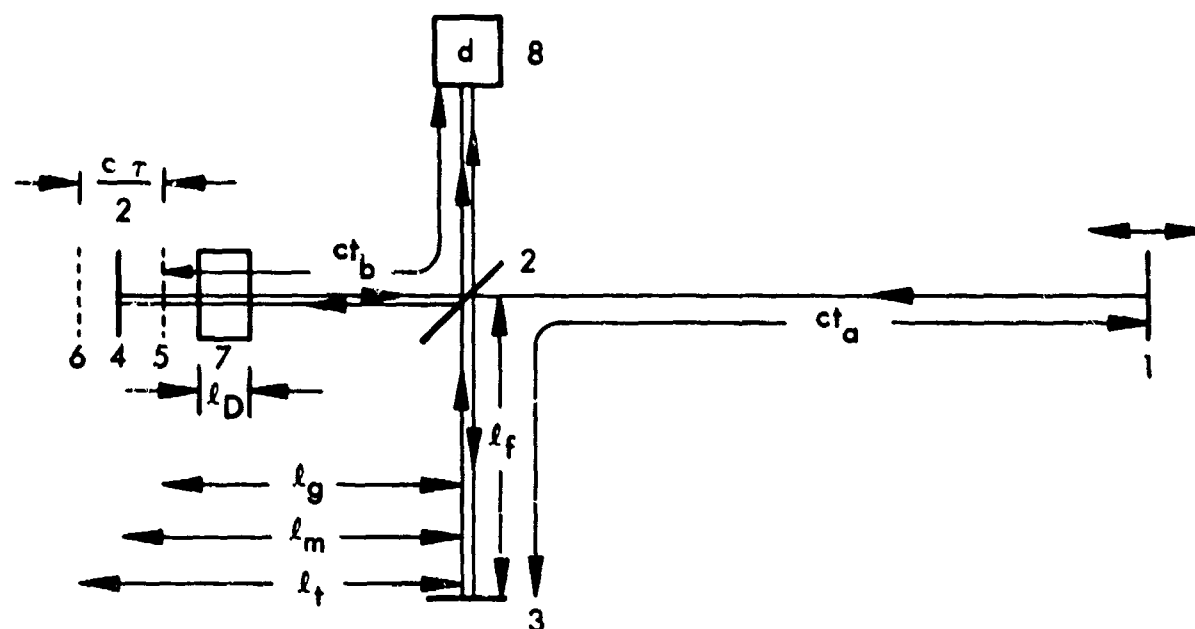
$$E_d(t + t_a + t_b + \tau) = E_1(t + t_a + t_b + \tau) + E_2(t + t_a + t_b + \tau) \quad (C.1)$$

where E_1 and E_2 are derived from the electric vector at the source by

$$E_1(t + t_a + t_b + \tau) = \kappa_1 E_o(t + \tau) \quad (C.2)$$

$$E_2(t + t_a + t_b + \tau) = \kappa_2 E_o(t)$$

The attenuation in each leg of the interferometer are approximately equal. Each ray passes through the beamsplitter once and is reflected once. Since $c\tau \ll c(t_a + t_b)$, the differential mirror spacing will have negligible effect on the relative amplitudes



- 1 moving source of light
- 2 beam splitter
- 3 fixed mirror
- 4 adjustable mirror
- 5 effective geometric position of mirror 4 $[l_g = l_f]$
- 6 effective travel time position of mirror 4 $[l_t = l_m + l_D (n-1)]$
- 7 dielectric etalon plate of thickness l_D
- 8 detector

Fig. C-1 Differential Interferometer Having Travel Time Difference τ

C-2

LOCKHEED MISSILES & SPACE COMPANY

due to geometric differences. The dielectric etalon plate is nonabsorbing and anti-reflection coated for 6328A, and thus introduces no significant attenuation in that leg of the interferometer. We can therefore set $|\kappa_1| = |\kappa_2| = \kappa$ and since $c\tau \gg \lambda_0$, we can absorb any phase difference between κ_1 and κ_2 in the bias without otherwise affecting the situation. Thus, we have

$$\begin{aligned} E_1^{(r)}(t + t_a + t_b + \tau) &= \kappa E_0^{(r)}(t + \tau) = E^{(r)}(t + \tau) \\ E_2^{(r)}(t + t_a + t_b + \tau) &= \kappa E_0^{(r)}(t) = E^{(r)}(t) \end{aligned} \quad (C.3)$$

The (r) denotes that these are real, physical electric field vectors and not the complex representation.

The instantaneous intensity at the detector is given by

$$I_d^{(r)}(t) = E_d^2(t) \quad (C.4)$$

The quantity which we are able to observe with a system of response time T is the time averaged intensity observed over the time interval:

$$\langle I_d^{(r)} \rangle = \frac{1}{T} \int_0^T E_d^2(t) dt = \frac{1}{T} \int_0^T [E^{(r)}(t + \tau) + E^{(r)}(t)]^2 dt \quad (C.5)$$

Now we assume* that these fields have Fourier transforms:

$$E^{(r)}(t) = \int_0^\infty a(\nu) \cos [\varphi(\nu) - 2\pi\nu t] d\nu \quad (C.6)$$

Consider the associated functions

$$E^{(i)}(t) = \int_0^\infty a(\nu) \sin [\varphi(\nu) - 2\pi\nu t] d\nu \quad (C.7)$$

* Born & Wolf, Principles of Optics, 3rd ed., Pergamon Press, New York, Ch. 10, p. 494 ff, 1965.

and

$$E(t) = \int_0^\infty a(\nu) e^{i[\varphi(\nu) - 2\pi\nu t]} d\nu \quad (C.8)$$

The complex electric vector $E(t)$ is related to the real vector $E^{(r)}(t)$ and its associated function $E^{(i)}(t)$ by

$$E(t) = E^{(r)}(t) + i E^{(i)}(t) \quad (C.9)$$

Since all non-zero frequency components of the laser beam are very high, e.g., for all $a(\nu) \neq 0$, $\nu \gg \frac{1}{T}$, we can assume that for each ν approximately

$$\int_0^T a^2(\nu) \cos^2 [\varphi(\nu) - 2\pi\nu t] dt = \int_0^T a^2(\nu) \sin^2 [\varphi(\nu) - 2\pi\nu t] dt \quad (C.10)$$

and

$$\int_0^T a^2(\nu) \sin [\varphi(\nu) - 2\pi\nu t] \cos [\varphi(\nu) - 2\pi\nu t] dt = 0 \quad (C.11)$$

The approximations (C.10) and (C.11) are good to 1 part in 10^6 , the ratio of T to $1/\nu$ for $T =$ several nanoseconds and $\nu = 5(10^{14})\text{Hz}$. The above relations imply

$$\int_0^T E^{(r)}(t)^2 dt = \int_0^T E^{(i)}(t)^2 dt = \frac{1}{2} \int_0^T E(t) E^*(t) dt \quad (C.12)$$

From Eqs. (C.5) and C.12) we get

$$\begin{aligned} \langle I_d^{(r)} \rangle &= \frac{1}{2T} \int_0^T [E(t + \tau) + E(t)] [E^*(t + \tau) + E^*(t)] dt \\ &= \frac{1}{2T} \int_0^T E(t + \tau) E^*(t + \tau) dt + \frac{1}{2T} \int_0^T E(t) E^*(t) dt \\ &\quad + \frac{1}{2T} \int_0^T [E(t + \tau) E^*(t) + E^*(t + \tau) E(t)] dt \end{aligned} \quad (C.13)$$

Letting

$$I = \frac{1}{2T} \int_0^T E(t) E^*(t) dt \approx \frac{1}{2T} \int_0^T E(t + \tau) E^*(t + \tau) dt \quad (C.14)$$

and

$$\gamma_{11}(\tau) = \frac{1}{2IT} \int_0^T E(t + \tau) E^*(t) dt \quad (C.15)$$

we finally obtain, dropping the (r) ,

$$\langle I_d \rangle = 2I [1 + \text{Re } \gamma_{11}(\tau)] \quad (C.16)$$

Up to this point out only assumptions have been:

- The electric vector belongs to a radiation field to which is associated the usual intensity function.
- This radiation field has a Fourier transform.
- The frequency components are all large compared with $1/T$ and $1/\tau$.

It now becomes necessary to add one more assumption:

- The frequency width of the laser line over the interval of measurement is small compared with the frequency spread which would be associated with the time interval T .

This assumption allows us to write, to a good approximation

$$E(t) = e^{i\omega t} \quad (\text{letting } I = 1/2 \text{ for convenience}) \quad (C.17)$$

The self-correlation coefficient γ_{11} gives a measure for the fringe contrast obtainable. The visibility of the fringes is given as

$$V \equiv \frac{I_{\max} - I_{\min}}{I_{\max} + I_{\min}} = |\gamma_{11}| \quad (C.18)$$

The device will be so biased in practice such that the measurement of the maximum expected Doppler shift will take place between two points symmetrically placed about the 50 percent point (Fig. C-2).



Fig. C-2 Biasing Position on Intensity Curve

If a fast velocity change occurs causing decrease in $|\gamma_{11}|$, the result will be an error in the reading of I_b (Fig. C-3).

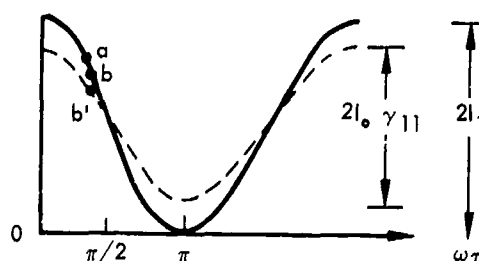


Fig. C-3 Effects of a Decrease in Visibility

The change in intensity at (b) can be seen to be

$$2I_1(1 + \cos \omega_b \tau) - 2I_1(1 + |\gamma_{11}| \cos \omega_b \tau) = 2I_1(1 - |\gamma_{11}|) \cos \omega_b \tau$$

where I_1 = Intensity of one beam.

The fractional change in intensity at $\omega_b \tau$ due to visibility is thus

$$\frac{(1 - |\gamma_{11}|) \cos \omega_b \tau}{1 + \cos \omega_b \tau}$$

However, we want to consider the error in time-averaged intensity values due to visibility changes. We will assume that we are within the linear region of the intensity curve and that we are biased about $\omega_a \tau$ with an excursion of $\omega_D \tau$. The

The fractional change (or error) in the intensity reading is then given to good approximation by

$$\begin{aligned} \text{error} &= \frac{2I_1(1 - |\gamma_{11}|) \cos \left[\omega_a \tau + \frac{\omega_D \tau}{2} \right]}{I_{\text{bias}} - I_d} \\ &= \frac{(1 - |\gamma_{11}|) \cos \left[\omega_a \tau + \frac{\omega_D \tau}{2} \right]}{\cos \omega_a \tau - \cos \left[\omega_a \tau + \frac{\omega_D \tau}{2} \right]} \end{aligned} \quad (\text{C.19})$$

If we bias about the 50-percent point, we can see that maximum errors occur when the frequency excursion does not bring us past one-half the maximum expected Doppler shift.

Using time domain analysis, the effect on $\gamma_{11}(\tau)$ of a Doppler shift in one sampling period T will be investigated. We assume a linear frequency change

$$\omega = \omega_a + \omega_D t/T, \quad 0 \leq t \leq T \quad (\text{C.20})$$

Then we can write

$$E(t) = \exp \left[i \left(\omega_a t + \frac{\omega_D t^2}{2T} \right) \right] \quad (\text{C.21})$$

Using eqs. (C.15), (C.17), and (C.21), we obtain

$$\begin{aligned} \gamma_{11} &= \frac{1}{T} \int_0^T \exp \left\{ i \left[\omega_a (t + \tau) + \frac{\omega_D (t + \tau)^2}{2T} \right] \right\} \exp \left\{ -i \left[\omega_a t + \frac{\omega_D t^2}{2T} \right] \right\} dt \\ &= \frac{1}{T} \int_0^T \exp \left\{ i \left[\omega_a \tau + \frac{\omega_D \tau^2}{2T} + \frac{\omega_D \tau}{T} t \right] \right\} dt \\ &= \frac{1}{T} \exp \left\{ i \left(\omega_a \tau + \frac{\omega_D \tau^2}{2T} \right) \right\} \frac{T}{i \omega_D \tau} \left[\exp i \omega_D \tau - 1 \right] \end{aligned}$$

$$\gamma_{11} = \frac{1}{i\omega_D \tau} \exp \left\{ i \left(\omega_a \tau + \frac{\omega_D \tau^2}{2T} + \frac{\omega_D \tau}{2} \right) \right\} \left[\exp \left(i \frac{\omega_D \tau}{2} \right) - \exp \left(-i \frac{\omega_D \tau}{2} \right) \right] \quad (C.22)$$

$$\gamma_{11} = \exp \left\{ i \left(\omega_a \tau + \frac{\omega_D \tau}{2} + \frac{\omega_D \tau^2}{2T} \right) \right\} \frac{\sin \frac{\omega_D \tau}{2}}{\frac{\omega_D \tau}{2}} \quad (C.23)$$

Thus

$$\text{Re } \gamma_{11} = \cos \left[\omega_a \tau + \frac{\omega_D \tau}{2} + \frac{\omega_D \tau^2}{2T} \right] \frac{\sin \frac{\omega_D \tau}{2}}{\frac{\omega_D \tau}{2}} \quad (C.24)$$

We will examine the operation of the system and coherence errors introduced under present conditions:

$$T = 10^{-8} \text{ sec}$$

$$\nu_0 = \text{laser freq} \cong 5 \times 10^{14} \text{ Hz}$$

For a velocity v_D the Doppler shift is

$$\omega_D = 2\pi \nu_0 \frac{v_D}{c} = 2\pi \cdot 5 (10^{14}) \frac{v_D}{3 (10^{10})},$$

$$\omega_D = \frac{\pi}{3} (10^5) v_D \text{ where } v_D \text{ is in cm/sec}$$

We will select τ , the total path differential, to produce a maximum expected excursion from approximately $I_m/3$ to $2I_m/3$. From Appendix A this corresponds to

$$\omega_D \tau = \frac{2\pi}{9}.$$

To allow maximum utilization of the nearly linear part of the intensity curve, we will bias the system such that the system is initially $\frac{\omega_D \tau}{2}$ above (or below) the symmetric $\omega \tau = \pi/2$ point. The maximum expected excursion during the change in velocity will thus be from $\omega \tau = \frac{7\pi}{18}$ to $\frac{11\pi}{18}$.

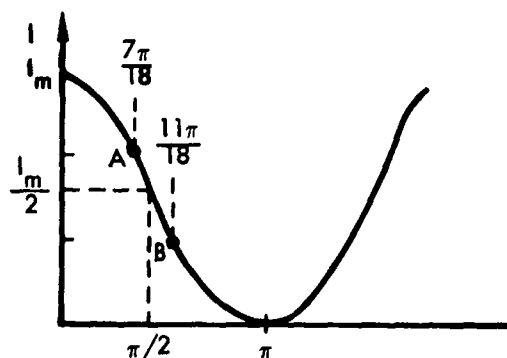


Fig. C-4 Example Operating Points on Intensity Curve

Biasing of the system is done by adjusting τ . Thus from Eq. (C.24) with $\omega_D = 0$ we find that we will initially bias with $\omega_a \tau = 7\pi/18$.

From Eqs. (C-16) and C-24) the intensity including correlation effects may be written as

$$\langle I_d \rangle = 2I_1 \left[1 + \cos \left(\omega_a \tau + \frac{\omega_D \tau}{2} + \frac{\omega_D \tau^2}{2T} \right) \frac{\sin \frac{\omega_D \tau}{2}}{\frac{\omega_D \tau}{2}} \right] \quad (C.25)$$

Correlation effects introduce errors in two ways as can be seen from comparing Eq. (C-25) with the expected value at one-half the Doppler shift, i. e.,

$$\langle I_d \rangle = 2 I_1 \left[1 + \cos (\omega_a \tau + \omega_D \tau/2) \right] \quad (C.25)$$

The first is due to a decrease in visibility. From Eqs. (C.18) and (C.23) we find

$$V = |\gamma_{11}| = \frac{\sin \omega_D \tau/2}{\omega_D \tau/2}$$

Following the discussion after Eq. (C.19) we will calculate the system error for a shift of $\omega\tau = \pi/9$. Then

$$|\gamma_{11}| = \frac{\sin \pi/18}{\pi/18} = 0.995$$

So the pattern height shifts by 0.5 percent. The error in the intensity reading is given by Eq. (C-19).

$$\begin{aligned} \text{error} &= \frac{(1 - 0.995) \cos \left(\frac{7\pi}{18} + \pi/18 \right)}{\cos 7\pi/18 - \cos \left(\frac{7\pi}{18} + \pi/18 \right)} \\ &= \frac{(0.005) (0.174)}{0.342 - 0.174} \\ &\cong 0.5 \text{ percent} \end{aligned}$$

The cosine term in Eq. (C.25) shifts our point along the I versus $\omega\tau$ curve by an amount $\frac{\omega_D \tau}{2} + \frac{\omega_D \tau^2}{2}$. The second source of error is due to the $\frac{\omega_D \tau^2}{2T}$ term, but this term is negligible, being smaller by a factor of $\tau/T \approx 10^{-2}$ than the other terms.

Thus we see correlation errors are primarily due to decrease in visibility and this error can be held to about 0.5 percent well within our system tolerances.

C.2 ERRORS DUE TO TIME-AVERAGING A NONLINEAR RESPONSE

As our system samples the intensity pattern during an interval T , the reading will be the time-averaged intensity. This value will depend upon the region of the intensity curve employed, the manner in which the frequency varies with time, and the magnitude of the Doppler shift. If we assume the same frequency-time curve as in Eq. (C.20), the time-averaged intensity will be given as:

$$I_{TA} = \frac{1}{T} \int_0^T I(t) dt = \frac{1}{T} \int_0^T 2I_1(1 + \cos \omega \tau) dt \quad (C.26)$$

$$I_{TA} = 2I_1 \left[1 + \frac{1}{T} \int_0^T \cos \omega \tau dt \right]$$

Since

$$\omega = \omega_a + \omega_D \frac{t}{T} \text{ for } 0 \leq t \leq T,$$

$$I_{TA} = 2I_1 \left[1 + \frac{1}{T} \int_0^T \cos \left(\omega_a \tau + \omega_D \tau \frac{1}{T} \right) dt \right]$$

$$I_{TA} = 2I_1 \left[1 + \frac{1}{\omega_D \tau} \int_{\omega_c \tau}^{(\omega_a + \omega_D) \tau} \cos x dx \right] \quad x = \omega_a \tau + \frac{\omega_D \tau}{T} t$$

$$I_{TA} = 2I_1 \left\{ 1 + \frac{1}{\omega_D \tau} \left[\sin(\omega_a + \omega_D) \tau - \sin \omega_a \tau \right] \right\} \quad (C.27)$$

The difference between the value of I_{TA} and $\langle I_d \rangle$ introduces another error into the system. This error depends on how we traverse the intensity curve from the initial bias point A in Fig. C-2.

If we bias our system about $\omega\tau = \pi/2$ as a midpoint for the expected shift $\omega_D\tau$, we can see from symmetry that if we get an ω_D as expected, then the excursion from initial point A to final point B will produce no time-average error. Thus the difference between I_{TA} and $\langle I_d \rangle$ is simply limited by the visibility factor mentioned before.

Errors are introduced if our Doppler shift is not the expected value since we are no longer in a symmetric situation. Maximum error for a linear frequency-time curve occurs if ω_D is one-half the expected value (i.e., $\omega'_D = \omega_D/2$). Using the parameters discussed, i.e., biasing with $\omega_a\tau = 7\pi/18$ a shift $\omega'_D\tau = \pi/9$ will give, using Eqs. (C.25) and (C.27),

$$\begin{aligned}\langle I_d \rangle &= 2I_1 \left[1 + \cos\left(\frac{7\pi}{18} + \frac{\pi}{18} + \frac{\pi}{18} \frac{\tau}{T}\right) \frac{\sin \frac{\pi}{18}}{\frac{\pi}{18}} \right] \\ &= 2I_1 \left[1 + \frac{\sin \frac{\pi}{18} \sin \frac{\pi}{18}}{\frac{\pi}{18}} \right] \\ &= 2I_1 [1 + 0.174]\end{aligned}$$

and

$$\begin{aligned}I_{TA} &= 2I_1 \left[1 + \frac{1}{\frac{\pi}{9}} \left(\sin \frac{\pi}{2} - \sin \frac{7\pi}{18} \right) \right] \\ &= 2I_1 [1 + 0.172]\end{aligned}$$

Since the system is biased such that $I_b = 2I_1 \left[1 + \cos \frac{7\pi}{18} \right] = 2I_1 [1 + 0.342]$,
the error due to time averaging is

$$\text{error} = \frac{\langle I_d \rangle - I_{TA}}{I_b - I_a} = \frac{0.173 - 0.172}{0.342 - 0.173}$$

$$\approx 1 \text{ percent}$$

These results suggest that the parameters of the system may be changed to include more of the intensity curve without significant error. If τ is increased to give $\omega_D \tau = \frac{\pi}{2}$ (i.e., $\tau = 10^{-10}$ s) then the system may be biased to go from $\omega \tau = \frac{\pi}{4}$ to $3\frac{\pi}{4}$, thus giving an intensity range of $0.15I_m$ to $0.85I_m$ for the maximum Doppler excursion anticipated.

The error may again be calculated. If we use $\omega_D' \tau = \frac{\pi}{4}$

$$\gamma_{11} = \frac{\sin \frac{\pi}{8}}{\frac{\pi}{8}} = 0.974$$

$$\text{error} = \frac{(1 - 0.974) \cos \frac{3\pi}{8}}{\cos \frac{\pi}{4} - \cos \frac{3\pi}{8}} = 3 \text{ percent}$$

Again the $\omega_D \tau^2 / 2T$ in the cosine term produces negligible error.

The maximum time-average error may be estimated at $\omega_D' \tau = \frac{\pi}{4}$ using Eqs. (C.25) and (C.27)

$$\begin{aligned} \langle I_d \rangle &= 2I_1 \left[1 + \cos \left(\frac{\pi}{4} + \frac{\pi}{8} + \frac{\pi}{8} \frac{\tau}{T} \right) \frac{\sin \frac{\pi}{8}}{\frac{\pi}{8}} \right] \\ &= 2I_1 [1 + 0.384] \end{aligned}$$

$$I_{TA} = 2I_1 \left[1 + \frac{1}{\pi} \left(\sin \frac{\pi}{2} - \sin \frac{\pi}{4} \right) \right]$$

$$= 2I_1 [1 + 0.374]$$

$$I_{bias} = 2I_1 \left[1 + \cos \frac{\pi}{4} \right]$$

$$= 2I_1 [1 + 0.707]$$

Thus,

$$\text{error} = \frac{0.384 - 0.374}{0.707 - 0.384}$$

$$\approx 3 \text{ percent}$$

From these calculations it seems feasible to increase the useful range of our instrument by a factor of 2 while still keeping within, say, a 4 to 5 percent error. It should also be remembered that these numbers represent worst case examples.

Appendix D

EFFECTS OF SURFACE IRREGULARITIES IN THE INTERFEROMETER

We assume that all optical surfaces have been worked to an rms deviation from flatness of σ . This analysis is performed on the originally intended design, to which we will return when we have better coatings on the antireflection surfaces.

Note that only path errors incurred while the beams are separate are influential in producing phase errors upon recombination.

Beam 1 in Fig. D-1 experiences the following:

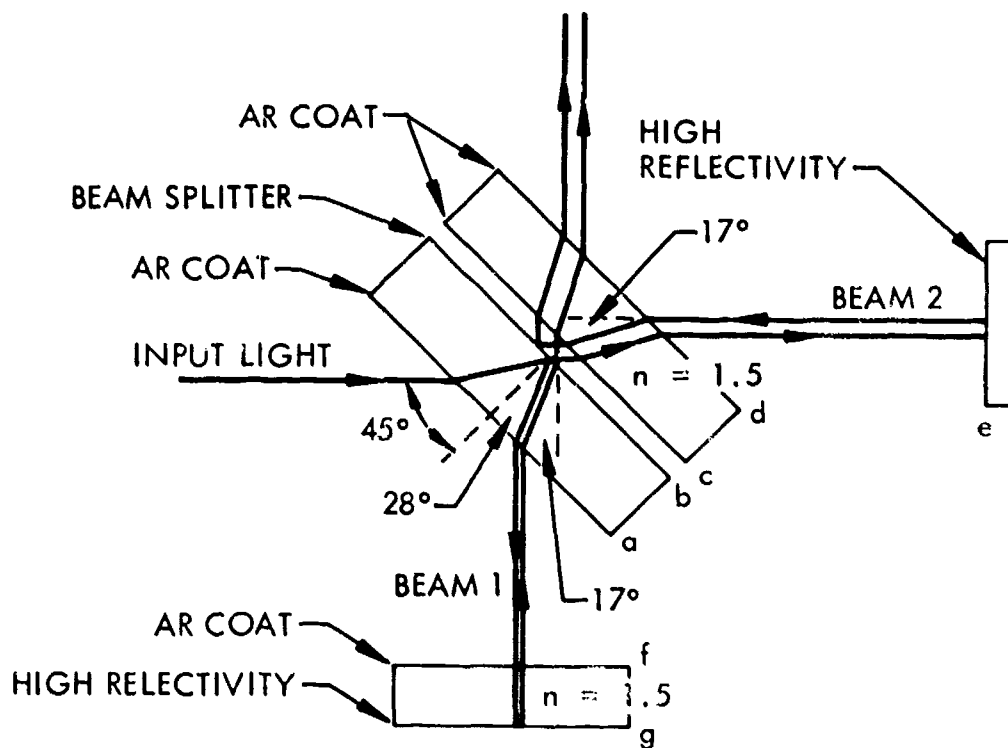


Fig. D-1 Beam Paths in Interferometer

D-1

- (1) Departure from b after reflection, in glass at 28 deg. The maximum effect of the error introduced by the deviation in flatness is computed by noting the change in total effective optical path (geometrical path times refractive index of medium in which ray travels).

We see in Fig. D-2 that the change in path length due to surface error is given by

$$\delta L = y - 1.5x^*$$

Since

$$y = 2\sigma \tan 28^\circ \cos 45^\circ$$

and

$$x = \sigma / \cos 28^\circ$$

we get

$$\delta L = -0.90\sigma$$

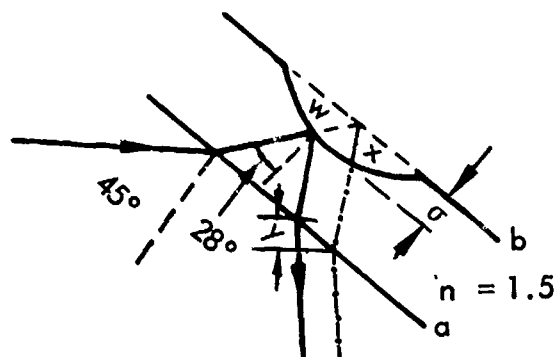


Fig. D-2 Errors Introduced by Reflection at Surface b

* w is not counted because both beams experience this difference.

D-2

LOCKHEED MISSILES & SPACE COMPANY

- (2) Transmission through a , 28 deg in glass to 45 deg in air.
Referring to Fig. D-3, we have

$$\delta L = y - 1.5x$$

since

$$x = \sigma / \cos 28^\circ$$

and

$$y = x \cos 17^\circ = \sigma \cos 17^\circ / \cos 28^\circ ,$$

we get

$$\delta L = (1.07 - 1.70)\sigma = -0.63\sigma$$

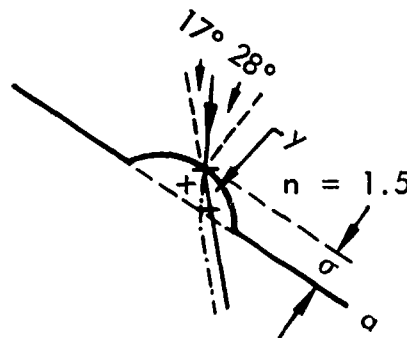


Fig. D-3 Errors Introduced by Transmission Through Surface a

- (3) Transmission air to glass at normal incidence through (f) .
In Fig. D-4 we see that the path difference is simply

$$\delta L = \sigma - 1.5\sigma = -0.5\sigma$$

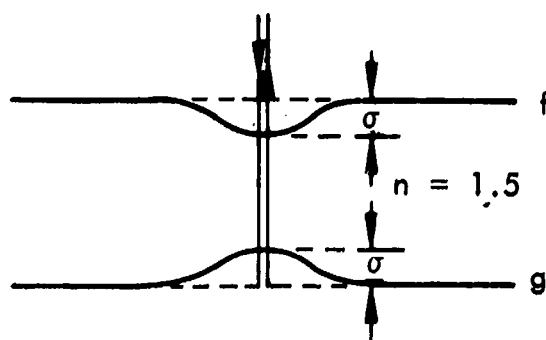


Fig. D-4 Errors Introduced by Surfaces f and g

- (4) Reflection at normal incidence from (g).

In Fig. D-4 we see that the path difference, due to the double pass, is

$$\delta L = -2(1.5\sigma) = -3.0\sigma$$

- (5) Transmission glass to air at normal incidence through (f).

By Fig. D-4,

$$\delta L = -0.5\sigma$$

- (6) Transmission, 45 deg in air to 28 deg in glass through (a).

As in (2),

$$\delta L = -0.63\sigma$$

- (7) Arrival at (b), 28 deg in glass. Same effect as (1), due to retrace of path:

$$\delta L = -0.90\sigma$$

- (8) Departure from (b), 45 deg in air.

See Fig. D-5.

D-4

LOCKHEED MISSILES & SPACE COMPANY

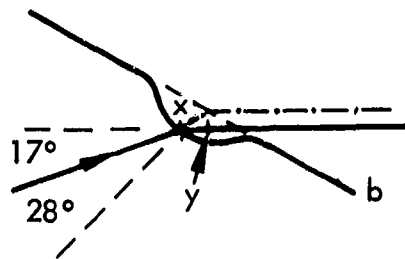


Fig. D-5 Errors Introduced by Transmission Through Surface b

$$x = \sigma / \cos 28^\circ$$

$$y = x \cos 17^\circ = \sigma \cos 17^\circ / \cos 28^\circ$$

$$\delta L = y - x = (1.07 - 1.70) \sigma = -0.63 \sigma$$

- (9) Transmission through (c), 45 deg in air to 28 deg in glass.
See Fig. D-6.

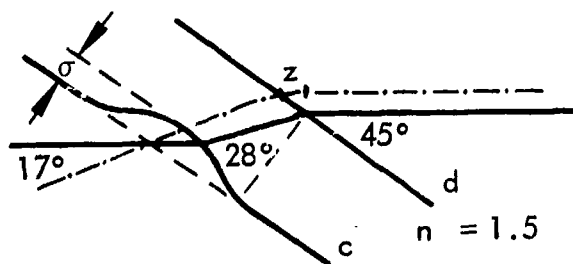


Fig. D-6 Errors Introduced at Surfaces c and d

$$\delta L = x - 1.5y - z$$

$$x = \sigma / \cos 45^\circ$$

D-5

LOCKHEED MISSILES & SPACE COMPANY

$$y = \sigma / \cos 28^\circ$$

$$z = y \tan 17^\circ = \sigma \tan 17^\circ / \cos 28^\circ$$

$$\delta L = (1.41 - 1.70 - .35)\sigma = -0.64\sigma$$

- (10) Transmission through d, glass at 28 deg to air at 45 deg.
Same as (2).

$$\delta L = -0.63\sigma$$

- (11) Reflection from (e) in air at normal incidence.

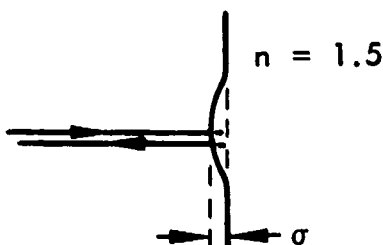


Fig. D-7 Error Introduced at Surface e

$$\delta L = -2\sigma$$

- (12) Same as (10), due to retrace of path.

$$\delta L = -0.63\sigma$$

- (13) Same as (9), due to retrace of path.

$$\delta L = -0.64\sigma$$

(14) Same as (8), due to retrace of path.

$$\delta L = -0.63\sigma$$

The differential path effects caused by each surface are then:

- (a) $-0.63 - 0.63\sigma = -1.26\sigma$ (2) and (6)
- (b) $-0.90\sigma - 0.90\sigma - (+0.63 + 0.63)\sigma$ (1) + (7) - (8) - (14)
 $= -3.06\sigma$
- (c) $(-0.64 - 0.64)\sigma = -1.28\sigma$ (9) and (13)
- (d) $(-0.63 - 0.63)\sigma = -1.26\sigma$ (10) and (12)
- (e) -2σ (11)
- (f) $(-0.50 - 0.50)\sigma = -1.0$ (3) and (5)
- (g) -3.0σ (4)

These constitute independent, random errors. We get the total probable error by computing the square root of the sum of the squares of the above, obtaining

$$\text{Probable system error} = 5.3\sigma$$

This places extremely stringent demands upon the optical surfaces for the interferometer. In fact, for the model used in our later tests, the observed standard deviation of 0.04 rad corresponds to 0.007λ . This could be dependably duplicated over a full angular aperture of several degrees only by setting tolerances presently beyond the state of the art — $\lambda/1,000$. We must therefore use the best available surfaces and expect a degradation of accuracy as we attempt to enlarge the angular range.

The above consideration relates only to the accuracy of measuring a pencil beam, which might wander in some unknown manner through the angular acceptance range. If we modify beam geometry so that we flood the entire useful range uniformly with light, allowing enough spillover so that a change in beam position or direction will not change conditions inside, then the above errors will cause only an effective loss of fringe visibility, which can be calibrated for given conditions. Then a Doppler

shift measurement can easily be more accurate by better than an order of magnitude, depending on the geometry of the errors and accuracy of beam uniformity.

Another way to improve accuracy is to sacrifice some angular range, as we did in the prototype, controlling beam position and direction within a small range known by observation to be usable. This technique enabled us to get useful data, despite the fact that surfaces were controlled to only $\lambda/20$.

Security Classification

DOCUMENT CONTROL DATA - R & D

(Security classification of title, body of abstract and indexing annotation must be entered when the overall report is classified)

1. ORIGINATING ACTIVITY (Corporate author)		2a. REPORT SECURITY CLASSIFICATION	
Lockheed Missiles & Space Company		2b. GROUP	
3. REPORT TITLE			
Laser Velocimeter Development Program Final Report			
4. DESCRIPTIVE NOTES (Type of report and inclusive dates)			
Final Report			
5. AUTHOR(S) (First name, middle initial, last name)			
C. W. Gillard		J. L. Rapier	
G. S. Ishikawa		J. C. Stover	
J. E. Peterson		N. L. Thomas	
6. REPORT DATE		7a. TOTAL NO. OF PAGES	7b. NO. OF REFS
3 Jan 1968			
8a. CONTRACT OR GRANT NO.		9a. ORIGINATOR'S REPORT NUMBER(S)	
DASA 01-67-C-0031		N-25-67-1	
b. PROJECT NO.			
c.		9b. OTHER REPORT NO(S) (Any other numbers that may be assigned this report)	
d.		DASA 2083	
10. DISTRIBUTION STATEMENT			
11. SUPPLEMENTARY NOTES		12. SPONSORING MILITARY ACTIVITY	
		Director, Defense Atomic Support Agency	
13. ABSTRACT			
<p>This report presents the results of investigations for developing a laser system capable of measuring the velocity history of the free surface of a solid, shock-loaded material. Experimental data as well as considerations and analyses basic to phenomena affecting the accuracy and functional deployment of the system are examined.</p>			

DD FORM 1473

REPLACES DD FORM 1473, 1 JAN 64, WHICH IS OBSOLETE FOR ARMY USE.

Security Classification

14.	KEY WORDS	LINK A		LINK B		LINK C	
		ROLE	WT	ROLE	WT	ROLE	WT

Security Classification



Defense Threat Reduction Agency

45045 Aviation Drive
Dulles, VA 20166-7517

CPWC/TRC

November 3, 1999

MEMORANDUM FOR DEFENSE TECHNICAL INFORMATION CENTER
ATTN: OCQ/MR WILLIAM BUSH

SUBJECT: DOCUMENT CHANGES

The Defense Threat Reduction Agency Security Office
has performed a classification/distribution statement
review for the following documents:

DASA-2519-1, AD-873313, STATEMENT A -
DASA-2536, AD-876697, STATEMENT A -
DASA-2519-2, AD-874891, STATEMENT A -
DASA-2156, AD-844800, STATEMENT A -
DASA-2083, AD-834874, STATEMENT A -
-DASA-1801, AD-487455, STATEMENT A -
POR-4067, AD-488079, STATEMENT C, -
ADMINISTRATIVE/OPERATIONAL USE
DASA-2228-1, AD-851256, STATEMENT C, *No Target*
ADMINISTRATIVE/OPERATIONAL USE *only chg'd from SA to adm/opn.*
RAND-RM-2076, AD-150693, STATEMENT D, -
ADMINISTRATIVE/OPERATIONAL USE
* AD-089546, STATEMENT A, ADMINISTRATIVE/OPERATIONAL USE * *ST-A*
DASA-1847, AD-379061, UNCLASSIFIED, STATEMENT C, *Jun '65*
ADMINISTRATIVE/OPERATIONAL USE *not in DTC*
RAND-RM-4812-PR, ELEMENTS OF A FUTURE BALLISTIC *370168*
MISSILE TEST PROGRAM, UNCLASSIFIED, STATEMENT C, *Conf*
ADMINISTRATIVE/OPERATIONAL USE *Authority to Declassify*

If you have any questions, please call me at 703-325-1034.

Arndith Jarrett

ARDITH JARRETT
Chief, Technical Resource Center

*Leave ST-A
On a Jarrett
23 Nov 99*